The University of Osaka
Institutional Knowledge Archive

Title	Direct synthesis of group IV-vacancy center-containing nanodiamonds via detonation process: formation mechanism and optical properties studied by time-resolved spectroscopy
Author(s)	牧野, 有都
Citation	大阪大学, 2023, 博士論文
Version Type	VoR
URL	https://doi.org/10.18910/92990
rights	© IOP Publishing. Reproduced with permission. All rights reserved.
Note	

The University of Osaka Institutional Knowledge Archive : OUKA

https://ir.library.osaka-u.ac.jp/

The University of Osaka

Direct synthesis of group IV−vacancy center-containing nanodiamonds via detonation process: formation mechanism and optical properties studied by time-resolved spectroscopy

YUTO MAKINO

SEPTEMBER 2023

Direct synthesis of group IV−vacancy center-containing nanodiamonds via detonation process: formation mechanism and optical properties studied by time-resolved spectroscopy

A dissertation submitted to
THE GRADUATE SCHOOL OF ENGINEERING SCIENCE
OSAKA UNIVERSITY
in partial fulfillment of the requirements for the degree of
DOCTOR OF PHILOSOPHY IN SCIENCE

BY

YUTO MAKINO

SEPTEMBER 2023

Abstract

Nanodiamonds (NDs) containing negatively charged group IV-vacancy (G4V$^-$) centers—silicon-vacancy (SiV$^-$), germanium-vacancy (GeV$^-$), and tin-vacancy (SnV$^-$) centers—have shown promising potential as fluorescent markers for bioimaging and biosensing, and single-photon sources for quantum information processing. The interest in these applications is mainly due to their small particle size and excellent optical properties. Although many studies have been conducted on the G4V$^-$ center-containing NDs (G4V-NDs), there are still two fundamental challenges left unanswered for their practical applications: (i) their production scale has been limited to the laboratory one; (ii) little is known about the effect of these small particle sizes on their optical properties. To address these challenges, this dissertation focused on a detonation process that produces NDs with an average particle size of 4–5 nm through the detonation of explosives. The simplicity of the process enables the production of detonation nanodiamonds (DNDs) in large quantities (tens or hundreds of tons per year) at low cost. The first purpose of this dissertation is to demonstrate the G4V-NDs synthesis by the detonation process (hereinafter referred to as "G4V-DNDs") through elucidating a formation mechanism of DND at the molecular level and then dopants selection. Since the produced G4V-DNDs are the smallest NDs, the G4V$^-$ centers in DNDs are sensitive to the particle size effects. The second purpose of this dissertation is to reveal the optical properties of the G4V$^-$ centers in DNDs and the particle size effects on them.

In Chapter 1, the background of this study was introduced: the optical properties of the G4V$^-$ center originating from its structural feature, previous production techniques of

the G4V-NDs, the detonation process, and the challenges for the practical applications of G4V-NDs. Through these introductions, I presented the strategy for addressing the challenges and the purposes of this dissertation. To implement the strategy, the detonation processes and time-resolved spectroscopy were essential and were mainly used in this dissertation. These experimental methods were described in Chapter 2.

In Chapter 3, an investigation of the DND formation mechanism during the detonation reaction was described. This study employed the time-resolved spectroscopic measurements of the detonation emission and a reactive molecular dynamics simulation of the explosive molecules. They revealed that atomic carbons (C_1) and six-membered ring carbons (C_6) species produced from the explosive molecules were observed as intermediate species of the DND formation. Hence, C_1- and C_6-mechanisms were proposed in which the C_1 and C_6 species function as building blocks for the DND formation, respectively. In addition, tetrakis(trimethylsilyl)silane (TTS) and triphenylsilanol (TPSOH) were selected as silicon dopants corresponding to the proposed C_1- and C_6-mechanism for a synthesis of the SiV^- center-containing DNDs (SiV-DNDs), respectively.

In Chapter 4, the detonation processes using explosives with individually added TTS and TPSOH selected in Chapter 3 were explained. The TTS or TPSOH-containing explosives produced DNDs with an average particle size of 7 nm (hereinafter referred to as “TTS- or TPSOH-DNDs”). To investigate the SiV^- center creation, photoluminescence (PL) measurements were carried out for the two types of DNDs. Only the PL spectrum of the TPSOH-DNDs exhibited luminescence corresponding to the SiV^- center at 1.68 eV. Hence, the SiV-DNDs were successfully synthesized via the detonation process using the aromatic compound TPSOH as the dopant. Moreover, the behaviors of TTS and TPSOH during the detonation reaction were investigated by time-resolved spectroscopic measurements of the detonation emission from the explosives with TTS or TPSOH. According to the time-resolved spectra, the achievement of the SiV-DNDs synthesis could be explained by the C_6-mechanism and aromatic structure of TPSOH.

In Chapter 5, the trials of the GeV^- or SnV^- centers-containing DNDs (GeV- or SnV-DNDs, respectively) synthesis by the detonation process using aromatic molecules as dopants, including group IV atoms centered on tetraphenyl compounds, were reported. In addition, the SiV-DNDs fabrication has been accomplished in Chapter 4 and was also resynthesized in this chapter to compare generated concentrations of the GeV- and SnV-DNDs produced under the same conditions. The successful syntheses of the SiV- and GeV-DNDs were evidenced by PL spectra with zero-phonon lines (ZPLs) attributed to these color centers. However, as a result of the same strategy, the SnV-DNDs were not obtained in detectable concentrations in the PL measurements. When the generated concentrations of the SiV- and GeV-DNDs synthesized under identical conditions were evaluated based on the number of data points that clear ZPLs were observed on the PL mappings, the SiV-DNDs were found to be produced more predominantly than the GeV-DNDs. The successes and limitations of the direct G4V-DND synthesis were explained by the difference in thermodynamics for each dopant during the detonation reactions.

In Chapter 6, the optical properties of the SiV^- and GeV^- centers in DNDs were described. The luminescence from the SiV^- and GeV^- centers in DNDs have broader linewidth and smaller Debye-Waller factor compared with those of typical SiV^- and GeV^- centers in bulk-sized diamonds. Furthermore, the SiV^- centers in DNDs exhibited a shorter lifetime than that of typical ones. The differences in their optical properties were discussed in the effect of extremely small particle size, ~10 nm, on the electronic state of these G4V$^-$ centers and the inhomogeneity of the G4V-DNDs derived from the detonation process. In contrast, the fundamental properties of these G4V$^-$ centers, such as photostability, do not change.

In Chapter 7, a general conclusion was given. The SiV- and GeV-DNDs syntheses were demonstrated by the detonation process using aromatic compounds including the group IV atoms as dopants. Subsequently, the optical properties of the SiV$^-$ and GeV$^-$ in DNDs were revealed by systematic spectroscopic investigations. These achievements contribute to the practical application of the G4V-DNDs as fluorescent markers and single-photon sources.

Table of contents

List of abbreviations

ND	Nanodiamond
DND	Detonation nanodiamond
F-ND	Fluorescent nanodiamond
NV^0	Neutral nitrogen-vacancy
NV^-	Negatively charged nitrogen-vacancy
$G4V^-$	Negatively charged group IV-vacancy
SiV^-	Negatively charged silicon-vacancy
GeV^-	Negatively charged germanium-vacancy
SnV^-	Negatively charged tin-vacancy
PbV^-	Negatively charged lead-vacancy
G4V-ND (or DND)	$G4V^-$ center-containing ND (or DND)
SiV-ND (or DND)	SiV^- center-containing ND (or DND)
GeV-ND (or DND)	GeV^- center-containing ND (or DND)
SnV-ND (or DND)	SnV^- center-containing ND (or DND)
HPHT	High-pressure–high-temperature
CVD	Chemical vapor deposition
CJ	Chapman-Jouguet
TNT	2,4,6-Trinitrotoluene
RDX	Hexahydro-1,3,5-trinitro-1,3,5-triazine
TATB	1,3,5-Triamino-2,4,6-trinitrobenzene
HMX	Octahydro-1,3,5,7-tetranitro-1,3,5,7-tetrazocine
TTS	Tetrakis(trimethylsilyl)silane

TPSOH	Triphenylsilanol
TPS	Tetraphenylsilane
TPG	Tetraphenylgermane
TPT	Tetraphenyltin
PL	Photoluminescence
PLE	PL excitation
XRD	X-ray diffraction
XRF	X-ray fluorescence
TEM	Transmission electron microscopy
DI	Deionized
MCP	Micro-channel plate electron multiplier
CCD	Charge-coupled device
CMOS	Complementary metal oxide semiconductor
OPA	Optical parametric amplifier
CW	Continuous-wave
QM	Quantum mechanics
MD	Molecular dynamics
FC	Frank-Condon
APES	Adiabatic potential energy surface
GS	Ground state
ES	Excited state
ZPL	Zero-phonon line
PSB	Phonon sideband
HRF	Huang-Rhys factor
DWF	Debye-Waller factor

LVM	Local vibration mode
FWHM	Full-width at half-maximum
QE	Quantum efficiency
QD	Quantum dot
QIP	Quantum information processing
QC	Quantum computing

Chapter 1. General introduction

1.1 Nanotechnology for advances in medical and quantum fields

Nanotechnology is considered to be one of the most important technologies of the 21st century. Approximately 18 billion USD had been invested globally in nanotechnology by national and local governments as of the end of 2005 [1]. Recent intensive research and investment in nanotechnology have provided countless nanomaterials [2, 3], nanodevices [4, 5], and nanosystems [6, 7] that have triggered technological innovations in various fields. The medical field has been one of the greatest beneficiaries of nanotechnology. Its prime example is likely to improve the use of fluorescent markers for diagnostic and screening purposes [8, 9]. The most widely used fluorescent markers today are organic dyes, which have non-ideal properties in this application as follows: (i) their luminescence is blinking and bleaching; (ii) their luminescence intensity is sensitive to surrounding environments such as pH, temperature, and solvents [10–12]. To improve such aspects of the organic dyes, nanotechnology has provided quantum dots (QDs) [12, 13]. They are semiconductor nanocrystals and show broad absorption characteristics with narrow luminescence spectra that are continuous and tunable because of quantum size effects [14]. In comparison with organic dyes, the QDs exhibit non-bleaching luminescence [15, 16]. These valuable properties make them promising alternatives to organic dyes [17, 18]. However, their implementation as fluorescent markers has been hampered by their blinking luminescence [12, 19]. In addition, the core of most QDs is composed of Cd known to be toxic, which also cannot be ignored for their practical use [20, 21]. Given the background above, the ideal fluorescent markers are still being searched for today. Figure 1.1 shows the number of publications per year from Google Scholar with the topic “fluorescent markers.” The ever-increasing number of articles since 2000 indicates the high interest in fluorescent makers. In the course of these studies, color center-containing nanodiamond (ND) particles—namely, fluorescent nanodiamond (F-ND) particles—have been newly proposed as candidates for ideal fluorescent markers [10, 22, 23]. The color centers in diamond structures act like isolated molecules in a solid host. There are more than 500 types of color centers [24], which emit bright luminescence in the visible to near-infrared region corresponding to their structures [25]. The interest in the F-NDs as fluorescent markers stems from their small particle size capable of entering living cells, biocompatibility originating from a diamond structure, and distinguished optical properties such as non-bleaching luminescence [26, 27]. The greatest advantage of the F-NDs in contrast to the QDs is their non-blinking luminescence [10, 26]. Hence, the F-NDs are nanomaterials with the potential to create next-generation medicine through higher-precision bio-imaging and -sensing. Another representative field that has benefited from nanotechnology is quantum application. In particular, developments in quantum information processing (QIP) and quantum computing (QC) have been spectacular [28, 29]. QIP and QC have each received billions of USD in investments over the past several years [30–32]. The realizations of these applications require not only innovations in both software and hardware but also the development of nanomaterials such as single-photon sources and quantum bits. As promising candidates as nanomaterials for these quantum applications, the F-NDs are also being actively studied [25, 33].

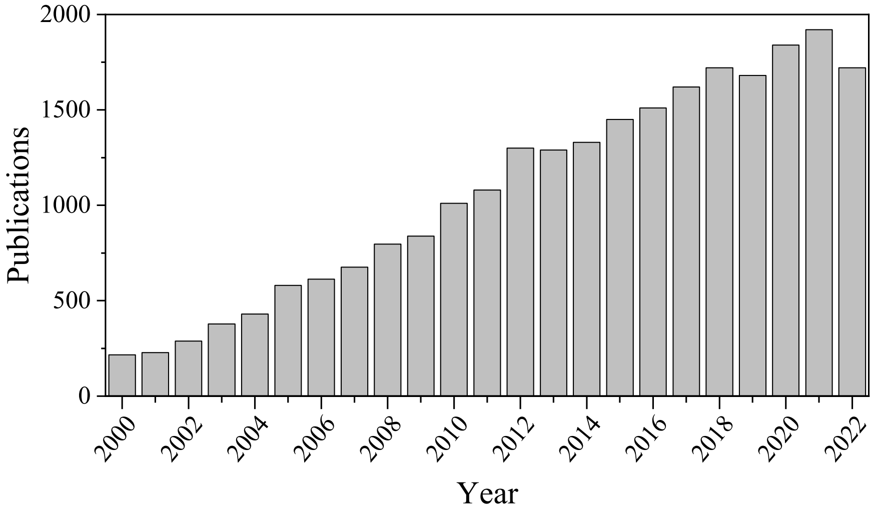

Figure 1.1 – Number of publications per year with topic "fluorescent markers." This source is Google Scholar using the keywords: "fluorescent marker" AND imaging OR sensing.

1.2 Color centers in diamonds

The F-NDs exhibit photoluminescence (PL) dependent on the color centers which are molecular-like defects in diamonds. Electronic transitions of the PL can be modeled by Frank-Condon (FC) principle which postulates Born-Oppenheimer approximation, as illustrated in Figure 1.2 [34, 35]. In this model, adiabatic potential energy surfaces (APESs) of electronic ground and excited states (GS and ES, respectively) are represented as harmonic oscillator potentials with equally spaced phonon energy levels (diamond lattice vibrational levels) indicated by black horizontal lines [36, 37]. Although the two APESs may have different shapes or effective phonon modes, they are assumed to be identical oscillators except for configuration coordinate ξ positions at their minimum energies. The ξ shift between the oscillators visualizes a change in electron cloud distributions of the color center in the diamond lattice accompanying their electronic transitions, namely, nuclear position changes of their equilibrium structures corresponding to the electronic states. However, the electronic transition is vertical in Figure 1.2 because the FC principle approximates that electron transitions are sufficiently fast compared with the nuclear motions [37–39]. In addition, the probability of the electronic transition between GS and ES involving the phonons is proportional to the square of overlap integral between the vibrational wavefunctions (orange curves in Figure 1.2) of initial and final states. In the PL process of optical absorption and emission, electrons excited from GS to ES undergo non-radiative transitions between the phonon energy levels, reaching the lowest phonon energy level of ES ($\nu' = 0$, in Figure 1.2) and then returning to one of the phonon energy levels of GS ($\nu = 0,\ 1,\ 2 \cdots$, in Figure 1.2) with radiative transitions. These radiative transitions are recorded in a PL spectrum, as emission lines. The radiative transition without phonon ($\nu' = 0 \rightarrow \nu = 0$, a green arrow in Figure 1.2) is observed as a prominent peak in the spectrum designated zero-phonon line (ZPL). Other radiative transitions with phonons ($\nu' = 0$ to $\nu = 1,\ 2 \cdots$, red arrows in Figure 1.2) also theoretically show peaks in the spectrum. However, they are sometimes not individually identifiable and form a continuous emission band, phonon sideband (PSB), on the low energy side of the ZPL because the acoustic phonons are continuous in a real crystal [39]. Since the adiabatic absorption process also involves electronic transitions between the same levels as the emission process, the absorption spectrum has a mirror image of the emission spectrum [36].

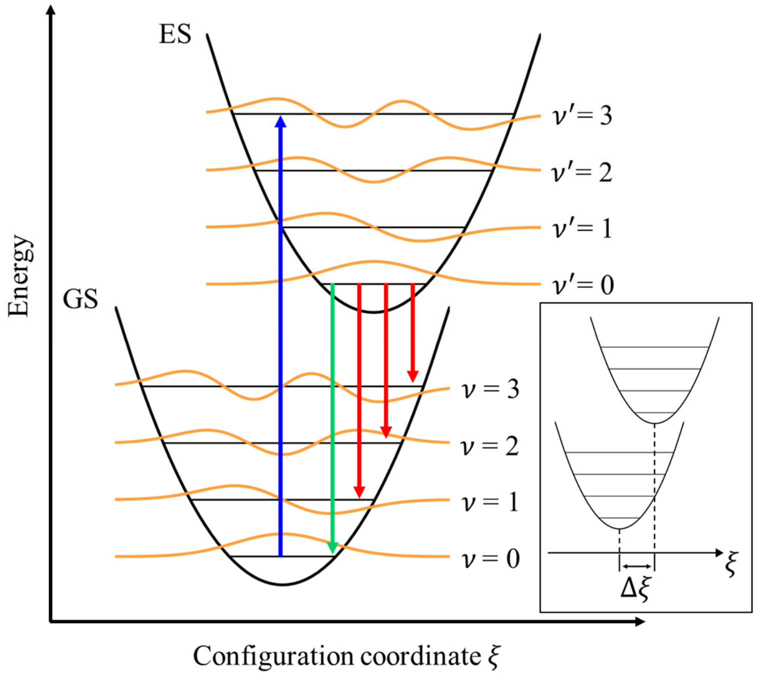

Figure 1.2 – FC principle for absorption and emission processes of a color center in diamond. APESs of GS and ES are denoted as black parabolas for harmonic oscillators. Horizontal black lines and orange curves represent phonon energy levels (diamond lattice vibrational levels) and their vibrational wavefunctions, respectively. Vertical absorption ($\nu = 0 \rightarrow \nu' = 0$) is shown in a blue arrow. Green and red arrows indicate transitions corresponding to ZPL ($\nu' = 0 \rightarrow \nu = 0$) and PSB ($\nu' = 0 \rightarrow \nu = 1$, 2, and 3), respectively. Inset in this figure shows a shift in equilibrium position of oscillators between GS and ES, as indicated by $\Delta\xi$.

One of the main properties of ZPL is the exponential dependence of its relative integrated intensity on temperature [35, 40, 41]. The ratio of the intensity of the ZPL (I_{ZPL}) to the total emission intensity (I_{Total}, sum of ZPL and PSB) is given by the expression

$$\frac{I_{\text{ZPL}}}{I_{\text{Total}}} = \exp[-S(T)]\,, \tag{1.1}$$

$$S(T) = \sum_{s} p_s(2\bar{n}_s + 1)\,, \tag{1.2}$$

where the S, p_s, and $\bar{n}_s$ denote Huang-Rhys factor (HRF), the dimensionless Stokes loss expressed in the number of phonons, and the thermal expectation value of the occupation number of the oscillator, respectively. The subscript s of the p_s and $\bar{n}_s$ distinguishes between multiple phonon modes that generally contribute to the emission process in a real crystal. The p_s and $\bar{n}_s$ is expressed by

$$p_s = \frac{m_s \omega_s^2 \Delta\xi_s^2}{2\hbar\omega_s}, \tag{1.3}$$

$$\bar{n}_s = \left[\exp\left(\frac{\hbar\omega_s}{k_\mathrm{B}T}\right) - 1\right]^{-1}, \tag{1.4}$$

where the m_s and ω_s are the effective mass and angular frequency of the s-th oscillator, $\hbar$ and k_B are Dirac and Boltzmann constants, T is absolute temperature, $\Delta\xi_s$ is a shift in the equilibrium position of the oscillators between GS and ES as shown by $\Delta\xi$ in the inset of Figure 1.2, respectively. Since $\bar{n}_s$ is a function of T, the HRF (S) depends on temperature. Moreover, S characterizes the electron–phonon coupling strength of the color center and diamond lattice; small S representing the weak electron–phonon coupling gives large $I_\mathrm{ZPL}/I_\mathrm{Total}$ which is evaluated as Debye-Waller factor (DWF) by the PL spectrum. Hence, it is essential to evaluate ZPL and DWF experimentally to understand the optical properties of F-NDs.

Among the color centers discovered thus far, the most investigated one is a nitrogen-vacancy (NV) center [42–44], which consists of a nitrogen atom substituting a carbon atom in a diamond lattice adjacent to a vacancy with $C_{3\mathrm{v}}$ symmetry [45, 46], as shown in Figure 1.3a. Neutral and negatively charged NV centers, NV^0 and NV^-, exhibit ZPLs at

2.16 and 1.95 eV [47], respectively. Since the ZPL of the NV⁻ center is spin-state dependent and its electron spins can operate under even ambient conditions, the ND containing the NV⁻ center is auspicious for application as quantum bits [48, 49]. In addition, the NV^0 and/or NV⁻ centers-containing NDs have also been studied for applications as fluorescent markers and single-photon sources, as their ZPLs are drawing attention [23, 42, 50]. However, both NV centers have been found not to be ideal materials for fluorescent markers and single-photon sources because their luminescence is spread over a large PSB with only ~4% present in the ZPLs at room temperature (~4% of DWF) due to their large electron–phonon coupling [51, 52], as shown in Figure 1.3b. Thus, researchers have investigated other color centers.

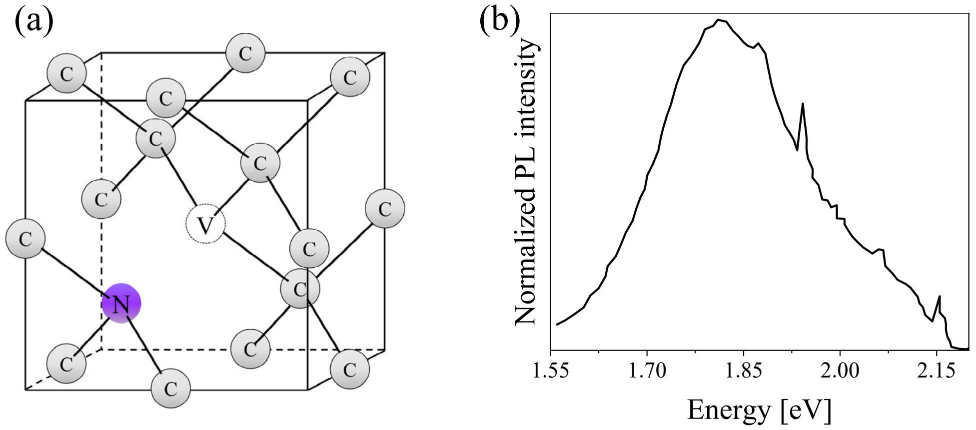

Figure 1.3 – (a) Structure of NV center in diamond lattice. Gray, white, and purple balls denote carbon atoms (C), a carbon vacancy (V), and a nitrogen atom (N), respectively. (b) PL spectrum of NV center in bulk-sized diamond. Small peaks at 2.16 and 1.95 eV are ZPLs of NV^0 and NV^- centers, respectively (Adapted from Ref [42]).

Nowadays, negatively charged group IV-vacancy ($G4V^-$) centers—silicon-vacancy (SiV^-), germanium-vacancy (GeV^-), tin-vacancy (SnV^-), and lead-vacancy (PbV^-) centers—have become widely known as a new class of color centers [52–54]. The $G4V^-$

center has a split-vacancy configuration, in which a group IV atom (Si, Ge, Sn, and Pb) is located between two carbon atom vacancies in a diamond lattice with D_{3d} symmetry, as shown in Figure 1.4a [51, 55–57]. This D_{3d} geometry forms an inversion symmetric potential for electronic orbitals [52, 58, 59]. As shown in Figure 1.4b, the electronic structure of the G4V⁻ center has GS (^2E_g) and ES (^2E_u) states that both have double orbital degeneracy. Without magnetic fields, the orbital degeneracy is lifted by spin-orbit interaction and dynamic Jahn-Teller interaction, producing a pair of split GS and ES. Each ES has dipole transitions to the two GS (A, B, C, D in Figure 1.4b). The emissions caused by the four dipole transitions cannot be separated unless they are measured at cryogenic temperatures. As a result, their emissions are usually observed as a single ZPL peak as an ensemble of them, as shown in Figure 1.4c. The ZPL positions of the G4V⁻ centers as the ensemble are summarized in Table 1.1. The luminescence concentration at the ZPLs due to their small electron–phonon coupling is in stark contrast with that of the NV centers. The reason for these excellent optical properties is that the G4V⁻ center is largely insulated from the diamond structure and the phonons by its split-vacancy structure with inversion-symmetric configuration and thus has a weak electron–phonon coupling [60]. In addition, the ZPLs peak positions of the G4V⁻ centers have shown good temperature sensitivity, as follows. The SiV⁻, GeV⁻, and SnV⁻ centers have shown temperature sensitivity down to 0.36, 0.30, and 0.50 K $Hz^{-1/2}$ around room temperature, respectively [61–63]. The optical properties of the G4V⁻ centers are suitable for the fluorescent markers for bio-imaging/-sensing and single-photon sources for QIP. Note that all the above values were observed from the G4V⁻ centers in bulk-sized diamonds. The optical properties of the G4V⁻ centers in NDs have not yet been adequately investigated.

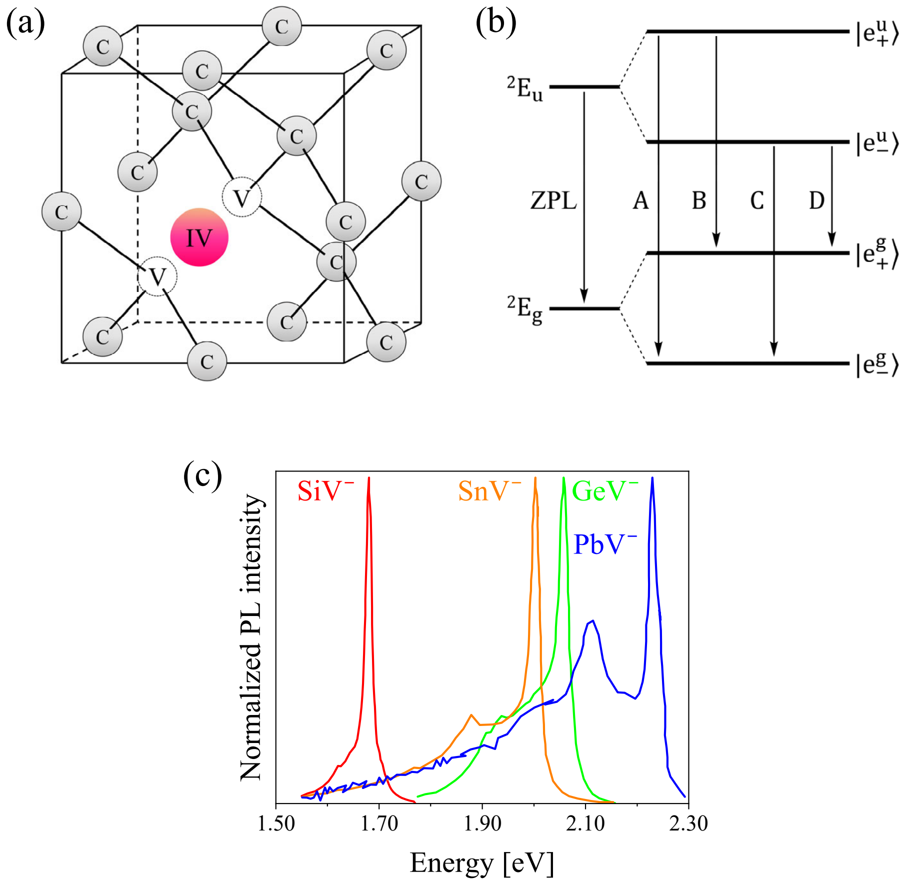

Figure 1.4 – (a) Split-vacancy structure of G4V center. Gray, white, and pink balls denote carbon atoms (C), carbon vacancies (V), and a group IV atom (IV), respectively. Group IV atom (IV) lies between two carbon vacancies. (b) Electronic structure and optical transitions (A, B, C, D) of G4V$^-$ center. (c) PL spectra of G4V$^-$ centers in bulk-sized diamonds (Adapted from Ref [52]).

Table 1.1 – Properties of ZPLs of G4V$^-$ centers in bulk-sized diamonds at room temperature [52, 64, 65].

G4V$^-$ center	ZPL [eV]	FWHM[a] [meV]	DWF
SiV$^-$	1.68	~11.4	~0.7
GeV$^-$	2.06	~17.1	~0.6
SnV$^-$	2.00	~19.4	~0.6
PbV$^-$	2.25[b] and 2.26[c]	12.6[b] and 14.1[c]	Not known

[a] Full-width at half-maximum; [b] corresponding to the transitions C in Figure 1.4b;
[c] corresponding to the transitions D in Figure 1.4b.

1.3 Synthesis techniques of group IV-vacancy center-containing nanodiamonds

Synthesis studies of the G4V$^-$ center-containing ND (G4V-ND) particles have been conducted in preparation for their applications as fluorescent markers and single-photon sources. These synthesis strategies employ techniques developed for producing bulk- and micro-sized diamonds containing the G4V$^-$ centers: high-pressure–high-temperature (HPHT), chemical vapor deposition (CVD), and ion implantation techniques.

The HPHT technique is a practical process for producing micron- and submicron-sized diamond particles widely used in the abrasives industry [66, 67]. HPHT diamonds are obtained from graphitic precursors under 5–6 GPa pressures and 1600–1900 K temperatures in a hydraulic press in the presence of metal solvents (also called catalyst: Fe, Ni, and/or Co), driven by the solubility difference between graphite and diamond phases in the solvent. In 1996, Sittas *et al.* reported the fabrication of 3 mm-sized diamonds containing the SiV$^-$ centers using an HPHT system with Si in the metal solvent [68]. This success raised hopes for an industrial-scale fabrication of the SiV$^-$ center-containing NDs (SiV-NDs) by the HPHT technique. However, there has been no active synthetic study on the SiV-NDs by this technique since their report. The reason is that it is difficult to keep the diamond size on the nanoscale by this technique owing to the high growth rate of the diamonds originating from high diffusion mobility of carbons in the metal solvent [69]. Therefore, the G4V-NDs fabrication by HPHT technique employed another strategy to obtain the diamonds directly converting solid organic compounds without the metal solvent. According to each publication in 2019, the SiV-NDs and GeV$^-$ center-containing NDs (GeV-NDs) were fabricated in laboratory scales. Bolshedvorskii *et al.* created 10 nm-sized SiV-NDs from a mixture of naphthalene ($C_{10}H_8$) and tetrakis(trimethylsilyl)silane

($C_{12}H_{36}Si_5$) under 8 GPa and 1300–1400 K [70]. Furthermore, Ekimov *et al.* fabricated 50 nm-sized GeV-NDs from adamantane ($C_{10}H_{16}$) with tetraphenylgermane ($C_{24}H_{20}Ge$) under conditions of 8–9 GPa and 1500–1900 K [69].

The CVD technique involves thermal or plasma dissociations of a mixture gas of carbon-containing compound and hydrogen followed by carbon deposition, resulting in the epitaxial growth of diamond crystals on a substrate under atmospheric pressure [71, 72]. Methane (CH_4) is mainly used as the carbon-containing compound, only needed to supply carbon atoms. The roles of hydrogen are to terminate dangling carbon bonds on the surface of the diamond layer or diamond nucleus and to prevent growth of graphite [73]. The CVD technique provides polycrystalline or single-crystalline diamonds. This is an unparalleled technology that can produce large-area diamond thin films or wafers for diamond electronic devices [74]. These CVD diamonds usually contain Si atoms as impurities owing to etching of the silicon substrates and CVD chamber walls [75]. Because Si atoms incorporated during the CVD growth process combine with vacancies *in situ*, SiV^- centers are generally observed in CVD diamonds. In 2011, Neu *et al.* prepared the SiV-NDs with sizes of 70–80 nm by crushing the CVD polycrystalline diamond film containing the SiV^- centers [76]. Controlled Si or Ge doping in the CVD process has also been known via adding monosilane (SiH_4) or monogermane (GeH_4) to CH_4/H_2 reaction gas [77, 78]. Romshin *et al.* reported the direct fabrication of 500 nm-sized SiV-NDs using the $CH_4/H_2/SiH_4$ system [79]. Furthermore, Westerhausen *et al.* demonstrated that GeV-NDs and SnV^- center-containing NDs (SnV-NDs) of several hundred nanometers were fabricated by a CVD process using germanium dioxide (GeO_2) and tin dioxide (SnO_2) as heteroatomic solid sources which are ionized by microwave plasma and then incorporated into the diamond growth process, respectively [80].

The ion implantation is a proven technique to introduce various types of color centers into bulk-sized diamonds [81–84]. In creation of the G4V$^-$ center by this technique, the diamond is irradiated with a beam of ionized group IV atoms and then post-annealing treatment to couple the group IV atom and carbon vacancies. By this technique, SiV-NDs preparations have been reported several times since the 2010s [85, 86]. It may be worth mentioning here that the PbV$^-$ center formation in a bulk-sized diamond by the ion implantation technique was reported by Wang *et al.* in 2021 [87]. This was the first successful creation of a diamond containing the PbV$^-$ center, which could be evaluated optical properties of the PbV$^-$ center. This success is expected to enable the fabrication of the currently undiscovered NDs containing the PbV$^-$ centers.

As summarized above, many fabrication techniques for the G4V-NDs have been reported, significantly contributing to the G4V-ND community. Based on these successes, the G4V-NDs synthetic research is taking the next steps toward their practical application, focusing on the following two points. The first point is productivity. The HPHT production of G4V-NDs by direct conversion of solid organic compounds has been reported only on the laboratory scale. The direct conversion method is not recognized as the industrial ND manufacturing process in contrast to the method using the metal solvent (including bulk-sized diamond production) [66]. In the CVD production, according to an estimate by Shenderova *et al.* in 2019 [67], only ~0.01 mg of 100 nm-ND particles can be obtained in one cycle of the CVD diamond production (typically ~1 h). Although there are ND production methods to crush bulk-sized diamonds, their multi-step process involving crushing and additional purification would limit productivity. To achieve mass production of the G4V-NDs, the inherently ND production scale of those technologies must be increased. This point is common in the ion implantation technique that uses the HPHT- or CVD-ND as raw materials. The second point is particle size. The G4V-NDs, as fluorescent markers and single-photon sources, can only reach their full potential at particle sizes as small as single-digit nanometers. When the G4V-NDs are administered to the body as fluorescent markers, the extremely small particle size can significantly reduce their accumulation in the kidneys [10]. Moreover, single-digit nanometer-sized G4V-NDs can move into living cells through their membranes since their small particle size is comparable to the size of typical biomolecules such as proteins [88, 89]. In the application of single-photon sources, the extremely small particle size increases the integration density of the G4V-ND in devices. While the fabrication method of SiV-ND by the CVD diamond crushing has been reported, its particle size seems to be limited to 70–80 nm [90]. At the present time, a synthetic method that combines industrial-scale productivity with single-digit nanometer particle size has not yet been found.

1.4 Detonation process for mass production of group IV-vacancy center-containing nanodiamonds

For the practical applications of the G4V-NDs, researchers have attracted attention to a detonation process. This technology is widely known to provide detonation NDs (DNDs) of 4–5 nm size on an industrial scale with tens or hundreds of tons per year at low cost (the scale estimated by Danilenko) [91–93]. This section describes the detonation process and then presents the SiV-NDs synthesis by this process.

Detonation is a supersonic combustion phenomenon with a detonation wave propagating in the condensed (solid or liquid) explosive (gaseous detonation is outside the scope of this dissertation) [94–96]. The detonation wave is characterized by coupling a shock wave with an exothermic chemical reaction front behind it [97]. The shock wave at the detonation wave surface causes adiabatic compression of the explosive and subsequent chemical decomposition, resulting in the release of enormous amounts of energy from it in a fraction of a microsecond [98]. The detonation process using solid explosives is the technique for *in-situ* synthesis of the DNDs in the detonation phenomenon, which was developed in the Union of Soviet Socialist Republics in the 1960s [99]. The raw material for the DNDs is an explosive such as a mixture of 60 wt% 2,4,6-trinitrotoluene (TNT) and 40 wt% 1,3,5-trinitro-1,3,5-triazacyclohexane (RDX) whose chemical structures are shown in Figure 1.5a [90, 91]. The mixed explosive serves as carbon and energy sources for the diamond formation. The negative oxygen balance of the mixed explosive allows an appearance of free carbons in the decomposition reaction according to the formula:

$$\mathrm{CHON} \longrightarrow \mathrm{N_2} + \mathrm{H_2O} + \mathrm{CO} + \mathrm{CO_2} + \mathrm{C}. \qquad (1.5)$$

The free carbons condense to form the diamond structures. The detailed DND formation mechanism was proposed by Danilenko as follows [90, 91]. Figure 1.5b indicates a pressure-temperature phase diagram for nanocarbon. At the nanoscale, the diamond–graphite–liquid triple point is shifted to lower temperatures because Gibbs free energy depends on the surface energy [100]. As soon as the detonation phenomenon begins, the pressure and temperature in the system increase rapidly and reach Chapman-Jouguet (CJ) point, corresponding to the conditions when the explosive decomposition and energy release are essentially complete, shown as point A in Figure 1.5b [91, 98]. At the CJ point, atomic-scale free carbons generated from the explosive molecules agglomerate to form less than 2 nm clusters, which are in the liquid phase. As the pressure and temperature decay along the isentrope indicated in a red line in Figure 1.5b, the carbon clusters grow as droplet carbons and then crystallize when their size exceeds 2 nm. Finally, when the pressure and temperature cross the diamond–graphite equilibrium line, the diamond growth ends, and graphite formation begins. During the DND formation, the high-pressure and high-temperature conditions favorable for the diamond formation last only a few microseconds, resulting in the DND average particle size of 4–5 nm. In some cases, a reaction in the detonation phenomenon represents the process of material conversion of the explosive molecules that proceeds between the beginning of the explosive decomposition and the reaching of the CJ point; in this dissertation, the process from the beginning of the explosive decomposition to the completion of the DND formation is presented as a detonation reaction.

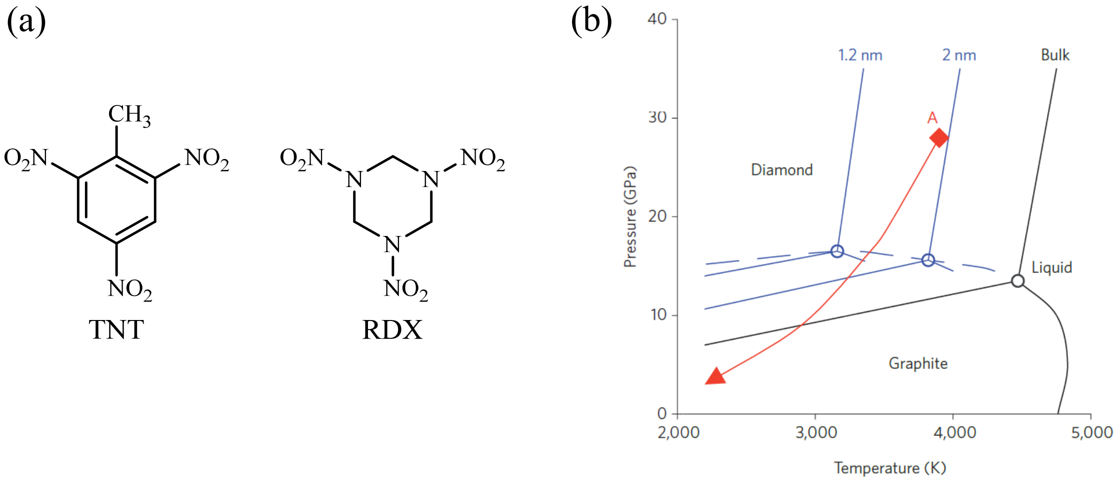

Figure 1.5 – (a) Chemical structures of TNT and RDX. (b) Nanoscale carbon phase diagram (Reprinted with permission from Ref [91]). Point A is CJ point. Black and blue lines are equilibrium lines of balk- and nano-sized carbons, respectively.

Practically, the explosive is detonated using an electronic detonator inside a steel chamber filled with various gas (such as N_2, CO_2, and Air) or H_2O (liquid or solid) [90, 91]. The detonation products are a mixture of the DNDs and the graphite. In addition, it also contains trace amounts of metals derived from the detonator and steel walls of the chamber. Because of removing these impurities, the detonation products are purified by an acid treatment.

The simplicity of the detonation process enables ND production in large quantities at low cost. The detonation process is an established technique for single-digit nanometer-sized NDs mass production. Hence, it also has attracted attention as a practical method for SiV-NDs production. However, there have been no reports of synthesized SiV^- center-containing DNDs (SiV-DNDs). According to a book regarding NDs edited by Arnaut in 2017 [90], a large number of samples of the DNDs were produced from explosives with various dopants, including Si. However, SiV^- luminescence was not observed in these samples. Thus, the detonation process has been considered unpromising for the SiV-DNDs synthesis.

1.5 Purposes of this dissertation

To implement the G4V-NDs as fluorescent markers and single-photon sources, it is necessary to establish a mass production technique of single-digit nanometer-sized ones. Although the HPHT and CVD techniques have achieved the G4V-NDs fabrications, the inherently low productivity of these techniques in NDs manufacturing has limited the G4V-NDs production to the laboratory scale. Furthermore, limiting the particle size of the G4V-NDs to single-digit nanometers further complicates its fabrication by the HPHT and CVD techniques. The most realistic way to fabricate the single-digit nanometer-sized G4V-NDs on a practical scale is to adopt the detonation process established as the mass production technology for the NDs with 4–5 nm sizes. Although some research has been carried out on the detonation synthesis of G4V$^-$ center-containing DNDs (G4V-DNDs) using explosives mixed with dopants as group IV atomic sources, there are no reports on their successful fabrication [90]. While experimental details, such as the dopant structures, are not published, it is clear that the mere presence of the group IV atoms in the explosive cannot achieve the G4V-DND fabrications. One of the strategies for the G4V-DNDs synthesis is to involve the dopants in the carbon cluster formation process by intermolecular interaction of the dopant with the explosive molecule. The dopant with a chemical structure enabling this strategy should be selected based on an understanding DND formation mechanism at the molecular level. However, there has been little research on the DND formation mechanism at the molecular level. Therefore, the first purpose of this dissertation is to demonstrate the G4V-NDs synthesis by the detonation process through the elucidation of the DND formation mechanism at the molecular level and subsequently dopants selection. In addition, this study allows for the representation of the detonation reaction as a chemical reaction based on the formation mechanism, thermodynamics, and kinetics. It provides an understanding of the detonation process from a perspective outside of explosives engineering.

The interest in the G4V-NDs for the biomedical and quantum fields is based on the optical properties of the G4V$^-$ centers, an ideal electronic state encapsulated in bulk-sized diamonds. Understanding the optical properties reflecting their electronic states is a prerequisite for any application. The G4V$^-$ centers stored in ND particles should exhibit altered optical properties compared with typical ones owing to their size effects. Nevertheless, little research has been done on the optical properties of the G4V⁻ centers inside NDs, as mentioned in Section 2. The difficulty in obtaining the G4V-ND samples is considered to hinder such research. Achieving the first purpose of this dissertation can eliminate this obstacle. Thus, the second purpose of this dissertation is to reveal the optical properties of the G4V⁻ centers in NDs produced by the detonation process, through systematic optical measurements. In addition, this study contributes to an understanding of the particle size effects on the electronic structure of the G4V⁻ centers in NDs. The particle size of DND is a few nanometers, which is extremely small among the NDs. Therefore, the electronic state of the G4V⁻ centers in DNDs must be significantly affected by the size effect relative to the other G4V⁻ centers in NDs. The effect appears clearly as the optical properties, facilitating discussion of their electronic structure. The discussion provides a foundational understanding lacking not only in the G4V-NDs but also in the F-ND community as a whole.

1.6 Dissertation overview

This dissertation is organized into the following seven chapters. The contents from Chapters 1–7 are based on the publication papers, as shown in List of publications.

Chapter 1 introduces the F-NDs and their fabrication techniques. Afterward, the reasons for focusing on the G4V-NDs and the detonation process in this dissertation are explained from their applicative point of view. In addition, the purposes and organization of this dissertation are described in this chapter.

Chapter 2 describes two main experimental methods used in this dissertation. As the first method, this chapter describes the detonation process consisting of the following procedures: (i) preparation of the explosive; (ii) purification of the detonation products; (iii) structural characterization of the DNDs. As the second method, this chapter describes the method of time-resolved spectroscopic measurement. There are instruments used for the measurement, operating principle, and system configuration.

Chapter 3 describes the investigation of the DND formation mechanism at the molecular level. The behavior of the explosive molecules during the detonation reaction is presented by the time-resolved spectroscopic measurements and a reactive molecular dynamics (MD) simulation. Based on these studies, two types of DND formation mechanisms are proposed. In addition, this chapter explains the selections of the dopants with chemical structures that each proposed mechanism involves for the SiV-DNDs synthesis.

Chapter 4 describes the SiV-DNDs synthesis by the detonation process. The SiV-DNDs synthesis is demonstrated by the explosive containing an aromatic silicon compound as one of the selected dopants in Chapter 3. This chapter also describes the time-resolved spectroscopic measurements of the emission from each explosive containing the selected dopants. Moreover, the effect of aromatic rings of the dopants for the SiV-DNDs synthesis is discussed by comparing the results in this chapter with the proposed mechanisms in Chapter 3.

Chapter 5 describes the synthesis of the GeV$^-$ or SnV$^-$ centers-containing DNDs (GeV- or SnV-DNDs, respectively). This study applies the detonation process using aromatic compounds as the dopant to these fabrications. Moreover, this chapter provides the reasons for the success and limitation of the direct G4V-DNDs synthesis via the detonation process from thermodynamic and kinetic points of view based on experimental results and quantum chemical calculations.

Chapter 6 describes the investigations of the optical properties of the SiV^- and GeV^- centers in DNDs. Their properties are determined by systematic optical measurements. The differences in the properties between the centers in DNDs and the typical ones in bulk-sized diamonds are explained by their characteristic electronic states depending on the extremely small particle size of the DNDs that encapsulate them.

Chapter 7 describes conclusion of this dissertation and future prospects of the F-NDs.

Chapter 2. Experimental methods

This chapter has presented the experimental methods for the DND synthesis and the time-resolved spectroscopic measurement, which were mainly used in this dissertation.

2.1 Synthesis and structural characterization of detonation nanodiamonds

2.1.1 Detonation nanodiamonds synthesis and purification

A mixed explosive consisting of 60 wt% TNT and 40 wt% RDX was prepared by compression to form a cylindrical charge (hereinafter referred to as "TR-explosive"), which was a raw material of undoped-DNDs. For the G4V-DNDs synthesis, a certain mass of each dopant as a group IV element source (Si, Ge, or Sn) was added in the course of the TR-explosive preparation. Chemical structures, chemical properties, and added quantities of these dopants were described in experimental details of corresponding chapters. All employed dopants are powdery solids at ambient pressure and temperature; therefore, they could be well mixed with TNT and RDX powders. The resultant mixtures were molded by pressing them into a cylindrical shape.

Each explosive was detonated in a detonation chamber owned by Daicel Corporation under a CO_2 atmosphere. The detonation products were purified with an acid mixture ($H_2SO_4 + HNO_3$) at 150 °C for 5 h. After cooling at 70 ºC, the reaction mixtures were added to deionized (DI) water and heated (at 150 °C) again for 5 h. The acid treatment was performed to remove sp^2 carbons and metal impurities. The precipitates were then rinsed with DI water and dried. After drying, the crude products were treated with aqueous 8 M NaOH at 70 ºC for 8 h to remove group IV dioxides (SiO_2, GeO_2, or SnO_2) as by-products derived from each dopant. Although the products obtained from the TR-explosive without dopants were uncontained to the group IV dioxides, the alkali treatment was also performed on them to compare properties of the undoped- and G4V-DNDs purified under the same conditions. Alkali-treated precipitates were added to DI water at room temperature, and the pH of the resultant mixtures was adjusted to 3–4 by addition of aqueous 1 M HCl. The crude suspension was centrifuged (CR22G, Hitachi Koki) at 8000 × *g* for 10 min, and the precipitates were separated and washed by adding DI water. The procedures of aqueous HCl addition and centrifugation were repeated. The collected precipitates were then rinsed with DI water and dried. Finally, purified samples were air-oxidized in O_2/N_2 (4/96 vol%) at 470 or 570 ºC for 2 h to remove trace amounts of sp^2 carbon. These procedures gave the undoped- and G4V-DNDs from the corresponding explosives.

2.1.2 Structural characterization of detonation nanodiamonds

All types of DNDs were characterized using powder X-ray diffraction (XRD; SmartLab, Rigaku) analysis and X-ray fluorescence (XRF; ZSX Primus IV, Rigaku) measurement with Cu-Kα_1 radiation ($\lambda = 1.54$ Å). The average crystallite sizes, approximately the average particle sizes of the DNDs, were then calculated using Scherrer's formula on the basis of the (111) diffraction peak which was the most intense diffraction peak in the XRD patterns. Transmission electron microscopy (TEM; JEM-1400 Plus, JEOL; acceleration voltage: 120 kV) was performed on a few droplets of a water suspension of these DNDs that were dried under ambient conditions on a grid.

Optical measurements were carried out to confirm constructions of the G4V$^-$ centers in DNDs. Drop-cast samples of each DND were prepared by dropping 100 µL of their 10 wt% aqueous suspensions onto glass substrates and drying under ambient conditions. The drop-cast samples were characterized using PL spectroscopy with a Raman spectrometer (Lab RAM Evolution, Horiba) equipped with a continuous-wave (CW) laser with an excitation energy of 2.33 eV. Inherent PL spectra, including the ZPLs of the SiV$^-$, GeV$^-$, and SnV$^-$ centers have been observed at this excitation energy and room temperature [58, 65, 101].

2.2 Time-resolved spectroscopic measurement

In this dissertation, intermediate species of the detonation reaction were identified by their emission in Chapters 3 and 4, and luminescence lifetimes of the G4V$^-$ centers in DNDs were determined in Chapter 6. The detonation reaction and radiative transition of excited electrons proceed on the pico- to microseconds time scale. Time-resolved spectroscopy using a streak camera was employed to measure such ultra-fast optical phenomena. This section provided an operation principle of the streak camera and an optical system configuration with the streak camera as its heart.

2.2.1 Operating principle

The streak camera is a device that resolves temporal information of the light to be measured and records it as spatial information, which is composed of a streak tube and a detector. The structure of the streak tube with a built-in micro-channel plate electron multiplier (MCP) is shown in Figure 2.1 [102–104]. The irradiated light forms a slit image on a photocathode by a lens system via an entrance slit. At the photocathode,

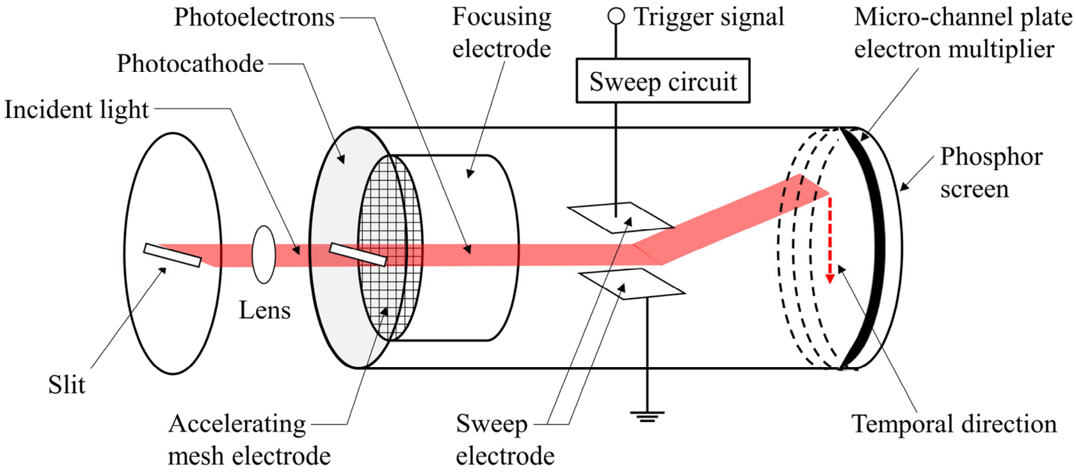

Figure 2.1 – Schematic of streak tube.

photoelectrons are emitted proportionally to the intensity of the light. The photoelectrons are rapidly accelerated by a mesh electrode and then traverse the streak tube after being suppressed in their spread by a focusing electrode. The photoelectrons pass between a pair of sweep electrodes to which a time-varying voltage is applied at a constant rate. The effect of the time-varying voltage is to generate a deflection electric field that sweeps early arriving photoelectrons upward and later ones downward. The ramp voltage application to the sweep electrodes is synchronized with the incident light via a trigger signal. The swept photoelectrons enter the MCP and are multiplied by several thousand times. Then these electrons sequentially collide with a phosphor screen and are converted back into light. The intensity of the light produced by the phosphor screen is linearly proportional to the optical intensity of the incident light. Therefore, temporal intensity variations of the measured light are converted into a vertical spatial luminance distribution on the phosphor screen as a streak image. The temporal resolution of the streak camera is typically in the range of pico- to milliseconds. In addition, the horizontal spatial distribution of the streak image corresponds to the horizontal position of the incident light. A streak camera equipped with a front-mounted spectrograph can generate the streak image with two-dimensional information of time and wavelength since the spectrometer converts the wavelength of the measurement light into horizontal spatial information. A time-resolved spectrum is obtained by measuring the intensity distribution of the streak image with a two-dimensional detector such as a charge-coupled device (CCD) camera or a complementary metal oxide semiconductor (CMOS) camera.

The streak cameras are classified into two types by time sweep methods of the photoelectrons: single-sweep and synchroscan types [102, 103]. In the single-sweep type, a ramp voltage is applied to the sweep electrodes in one direction, as shown in Figure 2.2a. The deflection distance of the photoelectrons is linearly proportional to the arrival time of the incoming photon (linear time axis). This type of streak camera due to the single-shot sweep is used to observe single-shot phenomena in which high-intensity emitted light. In practice, it also enables repetitive measurements up to a few MHz by trigger signals synchronized with the repetition frequency of phenomenon. This accomplishes the production of a high signal-to-noise ratio spectrum, even in dark phenomena. On the other hand, the synchroscan type is utilized for measurements requiring higher repetition rates. To achieve a higher repetition rate, the sweeping voltage can be applied in a sinusoidal high-frequency fashion in both directions, as shown in Figure 2.2b. The sinusoidal voltage synchronized with the repetition of the phenomenon enables a high repetition rate up to the GHz range and accumulates the streak images at precise locations on the phosphor screen. It must be taken into account that the deflection distance of the photoelectrons is no longer linear, resulting in a sinusoidal time axis. These types are used depending on measured phenomena and experimental environments. In this study, the streak camera observes the emission from the detonation reaction and the luminescence from the $G4V^-$ centers in DNDs. The detonation reaction is a one-time phenomenon of nano- to microseconds that emits high-intensity light. Although the luminescence from the $G4V^-$ centers has a pico- to nanoseconds lifetime and weak intensity, it is a repeated phenomenon excited by a pulsed laser of 1 kHz. Therefore, the single-sweep type streak camera is employed in all experiments of this study.

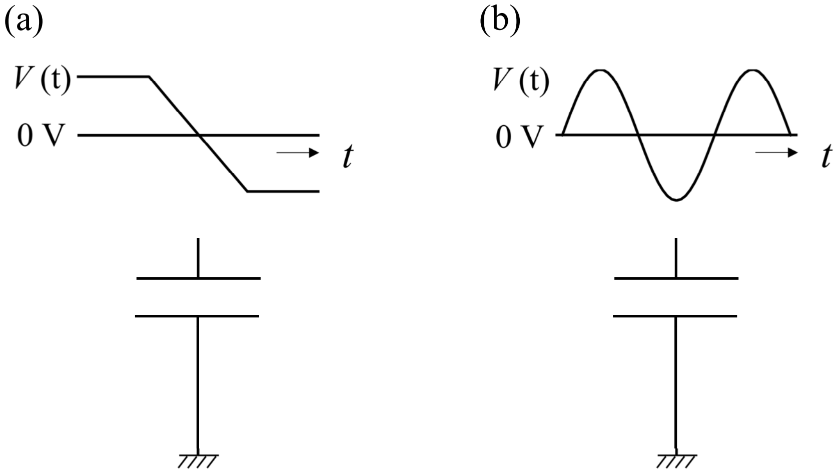

Figure 2.2 – Voltage waveforms on sweep electrodes: (a) single-sweep and (b) synchroscan types.

2.2.2 System configuration

Figure 2.3 is a schematic diagram of the optical system used in the time-resolved spectroscopic measurements [102]. This optical system consists of a measuring unit, an external trigger unit, and a readout unit. The measuring unit converts the temporal and wavelength information of the measurement light into spatial data by the streak camera equipped with the spectrometer. The external trigger unit activates the streak camera, and then a voltage is applied to the sweep electrodes. The generation methods of the trigger signal depend on the experimental environment and the time sweep methods. Because there are differences in the trigger generation methods between the observation of the detonation reaction (Chapter 3) and the luminescence lifetime measurement of the G4V⁻ centers in DNDs (Chapter 6), these methods are explained in experimental details of the corresponding chapters. The readout unit reads streak images produced on the phosphor screen in the streak camera. The CCD and the CMOS cameras were employed as the high-sensitivity cameras to detect the streak images in Chapters 3 and 4 experiments, respectively. Their connections to a computer were made using a flame-grabber board for the CCD camera and a USB interface for the CMOS camera. Finally, the streak image was read by the computer.

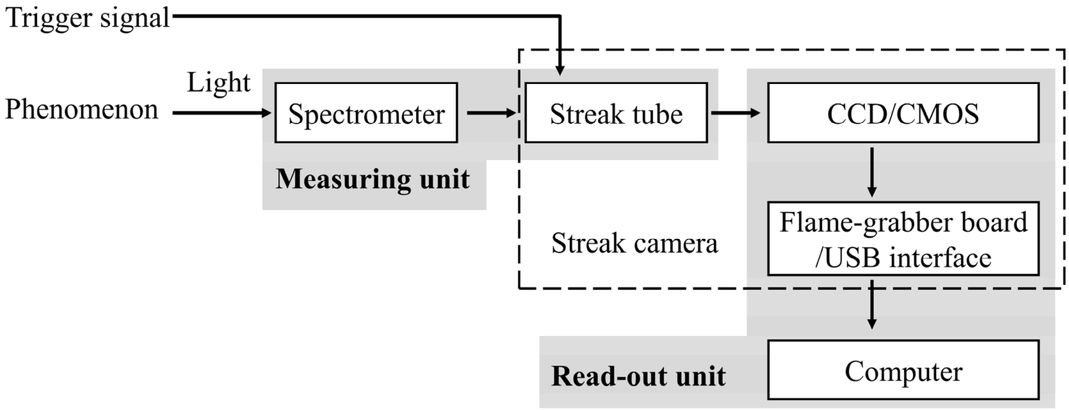

Figure 2.3 – Schematic layout of a streak camera system.

Chapter 3. Mechanism of nanodiamond formation during detonation reaction for silicon dopant selection

3.1 Introduction

In the previous chapter, time-resolved spectroscopy was described, which enables observation of ultra-fast optical phenomena. Using this technique as a key, the molecular level elucidation of the DND formation mechanism was attempted in this chapter. The DND formation mechanism during the detonation reaction has been actively studied since the discovery of the detonation process in the 1960s. According to Danilenko [90, 91], its basic mechanism is that carbon species generated from the decomposition of explosives condense and crystallize via droplets in the high-pressure and high-temperature environment of the detonation reaction, in agreement with the nanoscale carbon phase diagram (the details are described in Chapter 1.4). This mechanism is widely accepted. Moreover, the mechanism has been discussed from a molecular point of view. According to isotopic experiments [105, 106], the DNDs were almost composed of carbon atoms derived from TNT; thus, it is concluded that the roles of TNT and RDX have been to be the carbon source for the DND and to create sufficiently high-pressure and high-temperature conditions enabling the liquid-to-diamond phase transition, respectively. This conclusion is also supported by investigations of the relationship between the TNT/RDX ratio of the mixed explosive and the yield of DNDs. Therefore, the behavior of TNT molecules must be focused to reveal the DND formation mechanism. Dolmatov proposed a mechanism whereby radical-like carbon dimers (C_2) function as building blocks for the DND formation. The C_2 species are generated by the decomposition of explosive molecules such as TNT, which form the diamond structure via the construction of six-membered rings and/or adamantane skeletons (hereinafter referred to as “C_2-mechanism”) [106]. The rationale for this proposal is the energy balance between the energy generated by the explosive decomposition and the energy required to cleave the bonds of the explosive molecules. However, until now, there has been no experimental evidence to support the C_2-mechanism. One of the possible reasons for it is that the detonation reaction proceeds under extreme conditions: ultra-fast time scale of nano- to microseconds, high-pressure of several dozen GPa, and high-temperature of several thousand K. The extreme conditions make experimental observations of the intermediate species such as the C_2 building blocks during the detonation reaction considerably difficult. In this study, the intermediate species of the DND formation were observed using time-resolved emission spectroscopy (the details are described in Chapter 2) and a reactive MD simulation. The DND formation mechanisms at the molecular level were proposed on the basis of the observed intermediate species. In addition, for the SiV-DNDs synthesis by the detonation process, silicon compounds compatible with the proposed mechanism were selected as the Si-dopants to be added to the explosive as silicon sources.

3.2 Experimental detail in Chapter 3

3.2.1 Explosive preparation

In this chapter, the detonation reaction is recorded using a high-speed camera technique and time-resolved emission spectroscopy to investigate the DND formation mechanism. These optical experiments employed two types of explosives, as follows. First, a mixed explosive consisting of 60 wt% TNT and 40 wt% RDX was prepared by compression to form a cylindrical charge, which was referred to as the TR-explosive in Chapter 2.1.1. The TR-explosive used in this chapter had an amount and bulk density of 60 g and 1.52 g cm^{-3}, respectively. Second, a cylindrical charge of pure RDX was produced by pressing its powder (hereinafter referred to as “RDX-explosive”), which total amount and bulk density were 60 g (including 5.1 g paraffin wax as a binder) and 1.58 g cm^{-3}, respectively. The RDX-explosive was prepared as a reference for the TR-explosive. Each explosive was detonated in an explosion pit (98.5 m^3) owned by the Institute of Industrial Nanomaterials (IINa) of Kumamoto University. The emission from the detonation was detected by optical instruments installed outside the pit.

3.2.2 High-speed camera observation

A high-speed camera observation of the detonation phenomenon of the TR-explosive was carried out to investigate the time domain of the detonation reaction visually. This experiment was performed in the explosion pit. The TR-explosive detonated underwater to visually track a detonation wave propagating in the explosive. Underwater detonation prevents post-combustion caused by the reaction of detonation gases with ambient oxygen and allows observation of the inside of the explosive. The water does not affect the detonation wave propagation inside the explosive. Figure 3.1 shows an equipment arrangement in this experiment: the TR-explosive set in a water-filled container (external dimensions: 200 × 200 × 200 mm^3), a high-speed video camera (HPV-1, Shimadzu), and an arc flashlight (Power unit: SA-200F, Lamp house: LH-SA3, Nissin Electronic) were arranged in a straight line. The high-speed video camera enables a recording rate of 1 frame μs^{-1}. The activation of the high-speed camera with the detonation of the TR-explosive was synchronized by an ion-gap method which is a widely-used trigger-signal generation method for recording detonation phenomena [107].

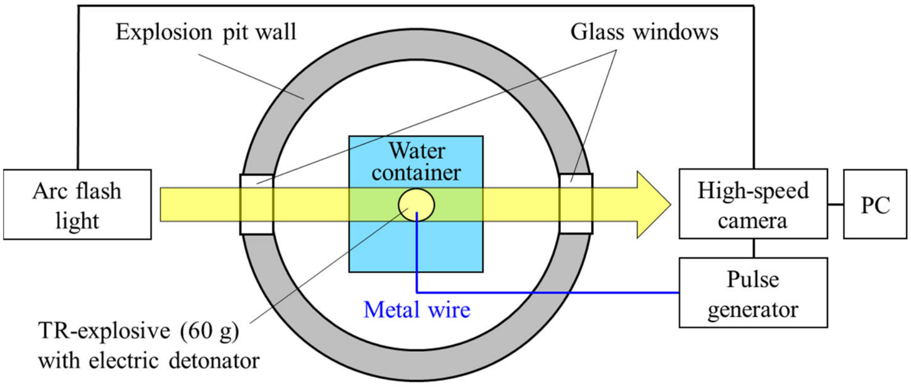

Figure 3.1 – Illustration of equipment arrangement for high-speed video camera observation.

3.2.3 Time-resolved emission measurement

The time-resolved emission measurements of the detonation reactions were performed to observe intermediate species of the DND formation. The TR- and RDX-explosives were individually detonated under an air atmosphere because the air in the large-scale explosion pit (98.5 m^3) could not be replaced by the CO_2 used in the DND syntheses described in Chapters 4 and 5. However, the external atmosphere does not affect the detonation reactions observed in these experiments since they proceed inside the solid explosives. Each detonation reaction from the TR- and RDX-explosives was observed using a handmade optical system, as schematically shown in Figure 3.2a. An optical fiber was positioned to capture the entire explosive. The light emitted from the reaction was collected through the optical fiber and then detected by a streak camera (C2830, Hamamatsu Photonics) interfaced with a spectrometer (C5094, Hamamatsu Photonics) equipped with a 50 grooves mm^{-1} grating. This optical system recorded time-resolved emission spectra with the time and energy resolution of 130 ns and 0.006 eV, respectively. The energy and intensity of the spectra were calibrated using a mercury-argon lamp (HG-1, Ocean optics) and a standard tungsten lamp (Calibrated lamp: 63358, Lamp mount: 63366, Oriel), respectively. This optical system also enables high energy resolution measurements of 0.0003 eV by employing 600 grooves mm^{-1} grating. In this case, the energy calibration was carried out using several standard lamps as follows: hydrogen, neon, argon, krypton, and/or xenon lamps (Calibrated lamp: Spectrum tube 4605, 4608, 4600, 4614, 4615, respectively; Power supply: SP-200, Electro-technic products). The overall experimental setup is shown in Figure 3.2b. The activation of the streak camera with the detonation of the TR- or RDX-explosives was synchronized by the ion-gap method. The streak camera was triggered by igniting an electric detonator with a metal wire via a pulse generator. The same electric detonator ignited the explosive through a detonating cord. The difference in transmission time between the metal wire and the detonating cord was eliminated by adjusting the length of the detonating cord.

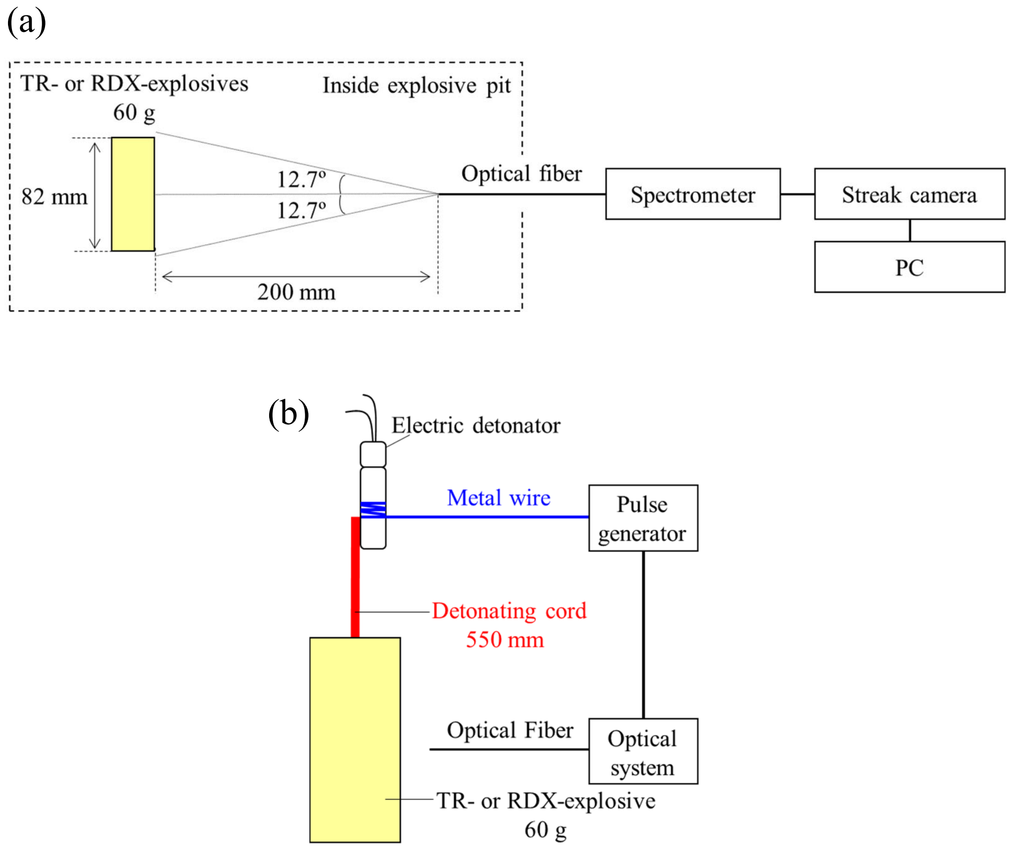

Figure 3.2 – (a) Schematic of optical system. Distance between TR- or RDX-explosives and optical fiber end was set to 200 mm, as calculated by height of these explosives (82 mm) and aperture angle of optical fiber (12.7°). (b) Visualization of overall experimental setup.

3.2.4 Molecular dynamics simulation

The thermal decomposition of solid explosives has been studied by MD simulations. This reaction proceeds under a condensed phase at high-pressure and high-temperature. Computational studies of such complex reactions require reproducing bond cleavages and formations of thousands of atoms over pico- to nanoseconds. Quantum mechanics (QM) methods are used to simulate organic chemical reactions because they can accurately predict the geometries, energies, and vibrational energies of small molecules [108].

However, their computational cost limitations make them inapplicable to the thermal decomposition system. Therefore, in 2011, Duin and Goddard III *et al.* developed a ReaxFF first-principles-based reactive force field for MD simulation [109]. The ReaxFF is based on the covalent formation and the bond order principle, which relates the bond energy to bond lengths, valence angles, and torsion angles. This realizes nearly accurate QM and as low computational cost as those for a simple force field. Energy contributions to the ReaxFF potential are summarized by the following [108, 110, 111]:

$$\begin{aligned} E_{\text{ReaxFF}} = E_{\text{bond}} + E_{\text{lp}} + E_{\text{over}} + E_{\text{under}} + E_{\text{val}} + E_{\text{pen}} + E_{\text{tors}} + E_{\text{conj}} \\ + E_{\text{Hbond}} + E_{\text{vdW}} + E_{\text{Coulomb}} + E_{\text{lg}} + E_{\text{Specific}} \, . \end{aligned} \tag{3.1}$$

E_{bond} is a continuous function of interatomic distance and describes the energy associated with forming bonds between atoms. E_{lp} and E_{Hbond} are lone-pair and hydrogen binding energies, respectively. E_{over} represents an over-coordinated energy, which is based on atomic valence rules. E_{under} is an undercoordinated atom, the energy contribution for the resonance of π-electron between attached under-coordinated atomic centers. E_{val} denotes an energy contribution from valence angle terms. E_{pen} is an additional energy penalty to stabilize the systems with two double bonds sharing an atom in a valency angle. E_{conj} denotes a conjugate effect of the molecular energy, especially for aromatic molecules where successive bond has bond order values of 1.5. E_{tors} represents torsion energies associated with torsion angle strain. Finally, E_{vdW} and E_{Coulomb} are respective electrostatic and dispersive contributions calculated between all atoms regardless of connectivity and bond-order. E_{lg} is a correction factor to improve the long-range dispersion interaction, added to E_{ReaxFF} in 2011 [112]. The ReaxFF potential containing E_{lg} is called a ReaxFF-lg.

There have been many papers on the molecular mechanism of explosive decomposition under high-pressure and high-temperature using the MD simulations with ReaxFF. In 2009, Zhang *et al.* investigated the decomposition and subsequent carbon clusters growth process of well-known explosives: 1,3,5-Triamino-2,4,6-trinitrobenzene (TATB) and octahydro-1,3,5,7-tetranitro-1,3,5,7-tetrazocine (HMX) [113]. In 2014, Furman *et al.* discussed initial processes in the thermal decomposition of condensed phase TNT, which begins with the C–N bond cleavages, focusing on its activation energy [114]. In 2013, Rom *et al.* studied thermal decomposition process of 0–30 vol% compressed liquid phase TNT under 1800–3500 K [115]. This study showed that the C–N bond cleavages and subsequent dimerization of TNT molecules proceed in the early stages of the reaction, followed by carbon clustering. This simulation was not pressure-controlled because of canonical ensemble (NVT) adoption. These papers are crucial for the study of this dissertation on the formation mechanism of the DND. In this study, I carried out the MD simulation with ReaxFF that reproduced the detonation reaction with reference to their papers for analyzing what intermediate species contribute to the formation of DND. The conditions for the reaction to be reproduced are as follows. Firstly, TNT should be adopted as the explosive, which is only a carbon source. Secondly, the initial phase of TNTs is in solid phase. Finally, simulation pressure and temperature must be 25 GPa and 3675 K, respectively, which are the conditions at the CJ point (the details described in Chapter 1.4) of the 1.6 g cm^{-1} mixed explosive consisting of 60 wt% TNT and 40 wt% RDX (TR-explosive) used for the DND productions in Chapters 4–5 and the optical experiments in this chapter [116].

The MD simulation of this study used the ReaxFF-lg potential implemented in the large-scale atomic/molecular massively parallel simulator (LAMMPS) code. This basic procedure was designed by Furman *et al.* and Rom *et al.* [114, 115]. The initial crystal structure of TNTs was obtained from Cambridge Structural Database available at the CCDC (http://www.ccdc.cam.ac.uk), CSD_CIF_ZZZMU01, as shown in Figures 3.3a and b. The unit cell was expanded in all three directions by (3 × 6 × 2) to create a supercell of 288 TNT molecules (6048 atoms). This supercell is shown in Figure 3.3c. Atomic positions and cell parameters are optimized by the conjugate gradient method until reaching minimum potential energy. The optimized supercell subsequently thermalized at 300 K for 5 ps constrained by Berendsen thermostat with 25 fs damping constant to reproduce its status under room temperature. Moreover, an isobaric–isothermal ensemble (NPT) simulation was carried out to relax excess pressure, where temperature and pressure were controlled by Nose-Hoover method at 1 atm and 300 K with 50 fs and 250 fs damping constants, respectively. The relaxed supercell made by these procedures presented a crystal density of 1.50 g cm^{-1}. Although the calculated density value does not match the experimental value of 1.65 g cm^{-1} owing to insufficient training of the E_{lg}, it has been reported that the effect on the reaction simulation is negligible [114]. Then, the supercell was volumetrically compressed at 35% to control the generated pressure of approximately 25 GPa in the NPT calculations described below. Optimization and microcanonical ensemble (NVE) simulation for an additional 5 ps were performed to relax stress inside the supercell caused by these compressions. The relaxed supercells were used for decomposition simulation at 3675 K and 25 GPa. The target temperature of 3675 K was reached from 300 K by rescaling atomic velocities for 100 fs. This rescaling is performed every 5 fs by ramped values between the start (300 K) and end (3675 K) temperatures. The pressure of the system reached 3675 K was approximately 25 GPa. The NPT calculation controlled by Nose-Hoover barostat and thermostat was used during the remainder of the simulation to maintain constant pressure and temperature at 25 GPa and 3675 K, respectively. The damping constant of the barostat and thermostat control was 10 fs. The rapid heating and constant thermalization timesteps were 0.1 and 0.2 fs, respectively. Moreover, bond formations and cleavages were monitored at arbitrary time steps using bond-order cutoff values shown in Table 3.1 (typical values in ReaxFF C/H/O/N high-energy simulations [114, 115]) to identify chemical species.

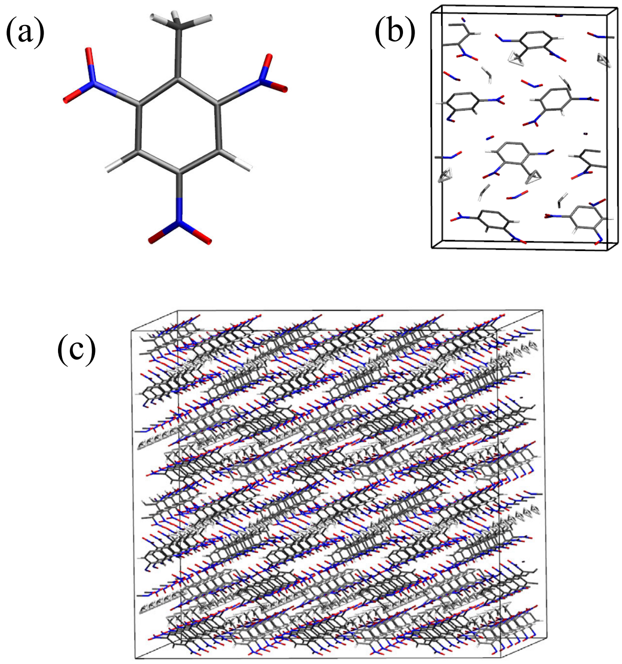

Figure 3.3 – (a) Molecular structure of TNT molecule. (b) Orthorhombic unit cell and (c) orthorhombic non-compressed supercell containing 8 and 288 TNT molecules, respectively. Gray, white, red, and blue sticks represent carbon, hydrogen, oxygen, and nitrogen atoms, respectively.

Table 3.1 – Atom pairs (atom#1 and atom#2) bond order cutoff values employed in chemical species analysis.

Atom #1	Atom #2	Bond order cut off
C	C	0.55
C	H	0.40
C	O	0.65
C	N	0.30
H	H	0.55
H	O	0.40
H	N	0.55
O	O	0.65
O	N	0.40
N	N	0.55

3.3 Results and discussion

3.3.1 High-speed camera observation

The high-speed camera observation was performed to investigate the time domain as an appearance of the detonation wave. Figures 3.4a–f show high-speed camera images of the detonation phenomenon in water, as recorded at a rate of 1 frame μs^{-1}. The time when the electric detonator was ignited was set as 0 μs (Figure 3.4a). The TR-explosive was detonated at 6 μs (Figure 3.4b). The detonation wave then propagated through the explosive (Figures 3.4c and d), and after 19 μs, the entire explosive had finished reacting (Figure 3.1e). Finally, explosive gas expanded (Figure 3.4f). Therefore, the time domain of the detonation wave in the TR-explosive is 13 μs.

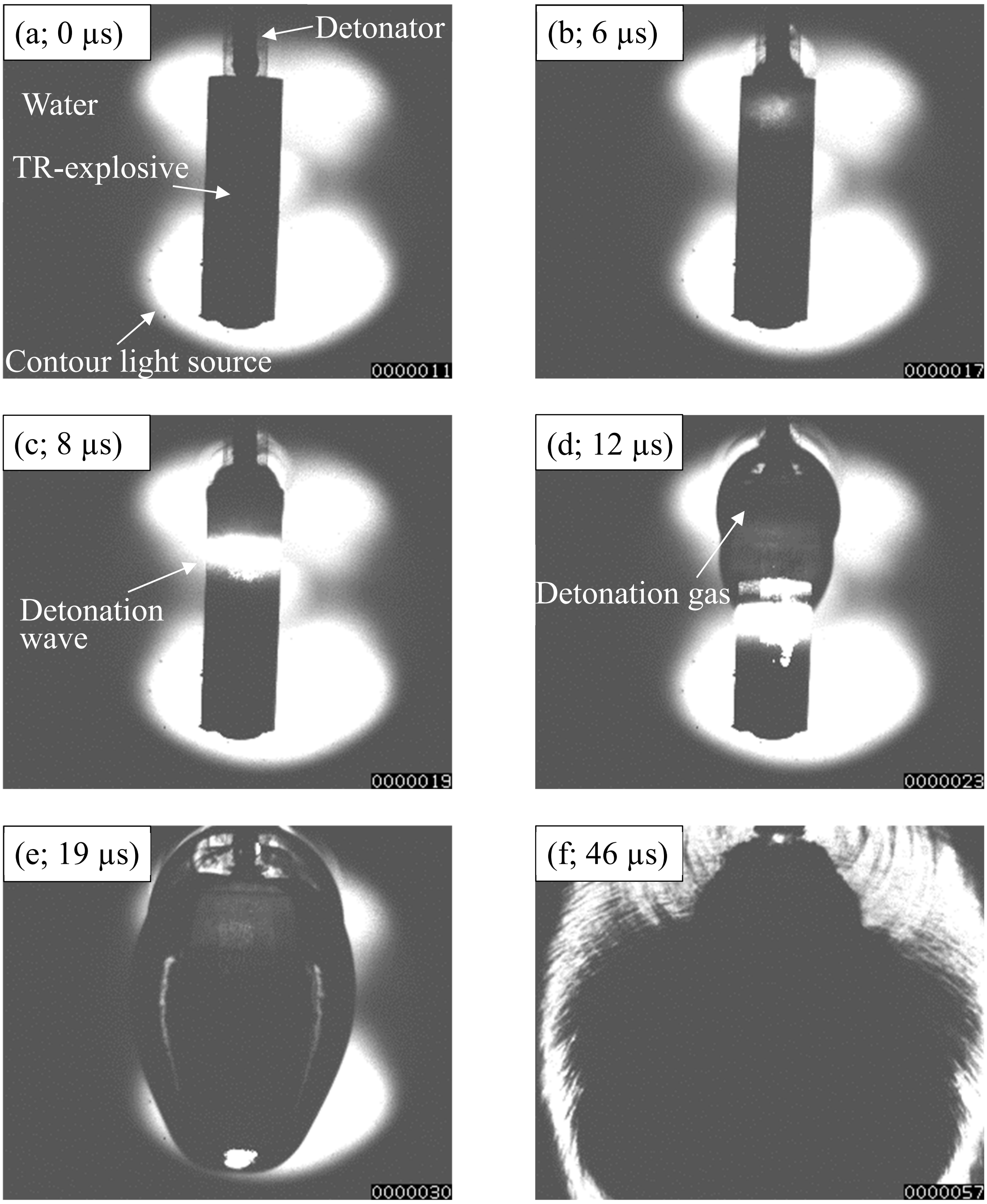

Figure 3.4 – High-speed camera images of detonation phenomenon. (a) Initiation time of detonator. (b) Start of detonation reaction. (c, d) Detonation propagation. (e) End of detonation reaction. (f) Expansion of the explosive gas.

3.3.2 Time-resolved emission measurement

The temporal evolution of the detonation phenomenon for the TR-explosives was measured using time-resolved spectroscopy to observe the intermediate species of the DND formation. The RDX-explosive as a component of the TR-explosive was also investigated to determine the origin of the emission from the detonation of the TR-explosive. Unfortunately, the TNT could not be examined because it does not detonate as a stand-alone explosive. The time-resolved emission spectra of the TR- and RDX-explosives are shown in Figures 3.5a and b, respectively, whose measurements employed the grating of the 50 grooves mm^{-1}. Figures 3.5a' and b' show the spectra extracted by the integration for 13 μs after the start of the significant emission in Figures 3.5a and b, respectively. The time domain of 13 μs is the same as that of the detonation wave observed with the high-speed camera (see Section 3.1). These spectra could not be fitted with Planck distribution and showed several sharp peaks. The peaks at 2.10 and 2.93 eV are shown in both spectra. The peaks at 1.74, 1.90, 2.02, 2.24, 2.52, and 2.72 eV are only observed in the emission from the RDX-explosive. Although these peaks detected for only the RDX-explosive must also be included in the emissions from the TR-explosive, these observations are probably hampered by a broad background peak emitted from the low-energy side observed only in the TR-explosive that should originate from TNT. Moreover, these time-resolved emission spectra did not show Swan-band of C_2 which is characteristic of the radical of diatomic carbon [117–119].

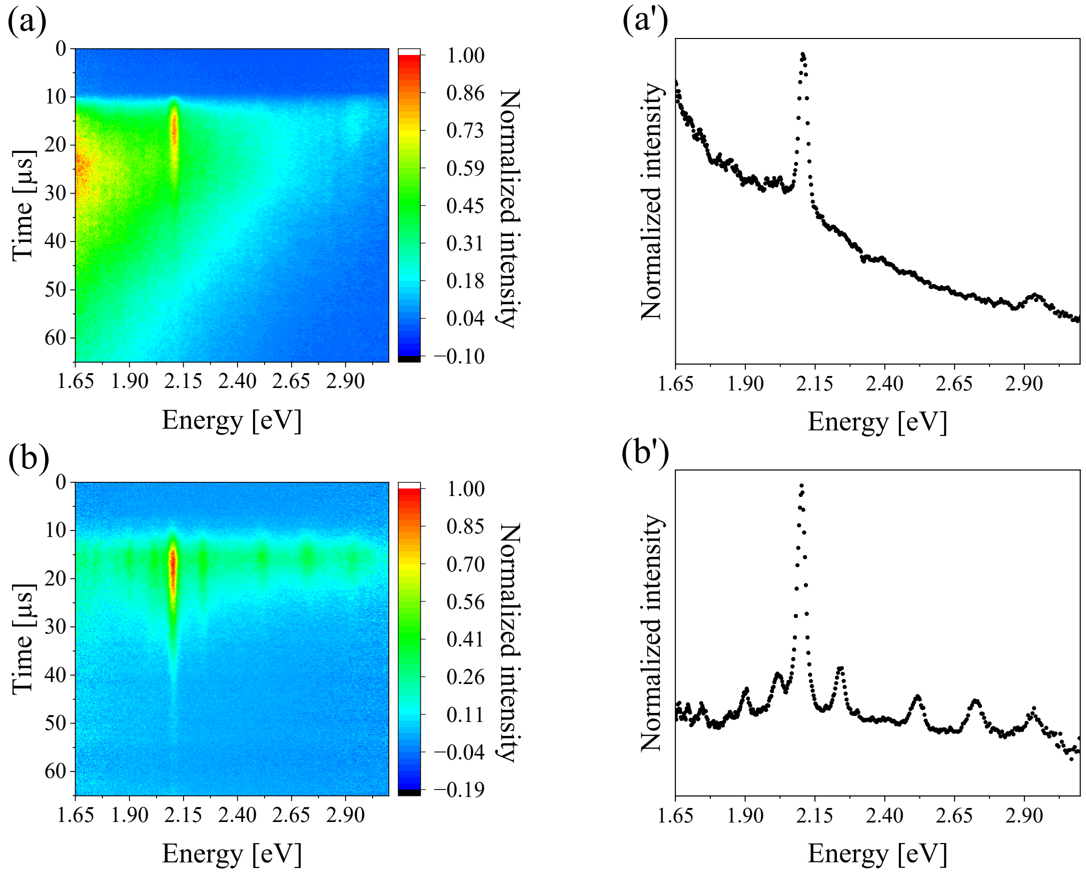

Figure 3.5 – Time-resolved spectra of emission from (a) TR- and (b) RDX-explosives. Spectral intensities in (a) and (b) represented small negative values because dark images were subtracted from raw streak images to remove background signals. Detonation reactions occurred for 13 µs (11–24 µs), and secondary combustion was observed after detonation reaction. (a') and (b') are time-integrated spectra over detonation reaction time domains in (a) and (b), respectively.

The significant peaks at 2.10 and 2.93 eV observed in the emission spectra from TR- and RDX-explosives are atomic emissions owing to their narrow linewidths. Since the emitting atoms are presumed to be involved in the DND formation during the detonation reaction, additional studies for these atomic emission assignments were performed by following procedures: (i) high-resolution time-resolved spectroscopic measurements of emission from the detonation of the TR-explosive using the finder grating of the 600 groove mm^{-1}; (ii) calculations of peak energies via peak fitting with functions; (iii) assignments concerning to the National Institute of Standards and Technology (NIST) atomic spectra database [120]. Firstly, the peak at 2.10 eV was assigned. Figure 3.6a is a high-energy resolution time-resolved emission spectrum around 2.10 eV. Figure 3.6b is a spectrum extracted by the integration between 11 and 24 µs as black dots, which was corrected by a linear baseline subtraction parallel to the x-axis. These spectra showed a target peak. Because the detonation reaction proceeds under 25 GPa and 3675 K, the emission peak was presumed to have an instrumental width ΔE_{i} plus Doppler width ΔE_{D} and a collision width ΔE_{c} (under an ideal gas assumption) expressed by Equations 3.2 and 3.3, respectively [121–124],

$$\Delta E_{\mathrm{D}} = \frac{2E_0}{c}\sqrt{\frac{2\ln 2 k_{\mathrm{B}} T}{M}}, \tag{3.2}$$

$$\Delta E_{\mathrm{c}} = 2\gamma P\,, \tag{3.3}$$

where E_0 is the atomic emission energy, c is light speed, k_{B} is Boltzmann constant, M is atomic mass, γ is a collision broadening coefficient that depends on temperature, P and T are pressure and temperature, respectively. ΔE_{i} and ΔE_{D} are expressed by a Gauss function, while ΔE_{c} is described by a Lorentz function [125]. Therefore, the emission peaks are presented by a Voigt function, which is the convolution of the Gauss and the Lorentz functions and is expressed by

$$F_{\mathrm{V}}(E) = F_0 + A\frac{2\ln 2}{\pi^{3/2}}\frac{w_{\mathrm{L}}}{w_{\mathrm{G}}^2}\int_{-\infty}^{\infty}\frac{\exp(-t^2)}{\left(\sqrt{\ln 2}\frac{w_{\mathrm{L}}}{w_{\mathrm{G}}}\right)^2 + \left(\sqrt{4\ln 2}\frac{E - E_0}{w_{\mathrm{G}}} - t\right)^2}dt\,, \tag{3.4}$$

$$w_{\mathrm{G}} = \sqrt{\Delta E_{\mathrm{i}}^2 + \Delta E_{\mathrm{D}}^2}\,, \tag{3.5}$$

$$w_{\mathrm{L}} = \Delta E_{\mathrm{c}}\,, \tag{3.6}$$

where $F_{\mathrm{V}}(E)$ is the emission intensity at energy E, F_0 is the baseline, A is the peak area, w_{G} and w_{L} are the full-width at half maximum (FWHM) of the Gaussian and Lorentzian components, respectively. A red line in Figure 3.6b shows that the emission peak is well-fitted with the Voigt function. According to the fitting parameters shown in Table 3.2, the Gaussian components, ΔE_{i} and ΔE_{D}, do not contribute to the atomic emission profile owing to w_{G} of ~0; therefore, the pressure effect expressed as the Lorentz component, ΔE_{c}, unexpectedly dominated the emissions from the reaction despite its high-temperature of 3675 K. Hence, the Lorentz function is used for the subsequent fitting of the emissions from the detonation reaction, represented as

$$F_{\mathrm{L}}(E) = F_0 + \frac{2A}{\pi}\frac{w_{\mathrm{L}}}{4(E - E_0)^2 + w_{\mathrm{L}}^2}\,, \tag{3.7}$$

as shown by a red line in Figure 3.6c. These fitting parameters are indicated in Table 3.2. The peak at 2.103 eV calculated by the Lorentz function fitting was assigned to

C(I) [$2s^2 2p3p$–$2s^2 2p7s$] atomic emission by referencing the NIST atomic spectra database [120]. Secondly, the peak at 2.93 eV in Figures 3.5a' and b' was assigned. Figure 3.7a is a high-energy resolution time-resolved emission spectrum around 2.93 eV. Figure 3.7b shows a spectrum extracted by the integration between times 9 and 22 μs as black dots, which was corrected by a linear baseline subtraction parallel to the x-axis. The single peak of the integration spectrum could be fitted by the Lorentz function, as indicated by a red line in Figure 3.7b. According to its fitting parameters shown in Table 3.3 and NIST atomic spectra database, the peak energy is 2.934 eV, which was assigned to O(II) [$2s^2 2p^2(^3\mathrm{P})3d$–$2s^2 2p^2(^3\mathrm{P})4f$] atomic emission [120].

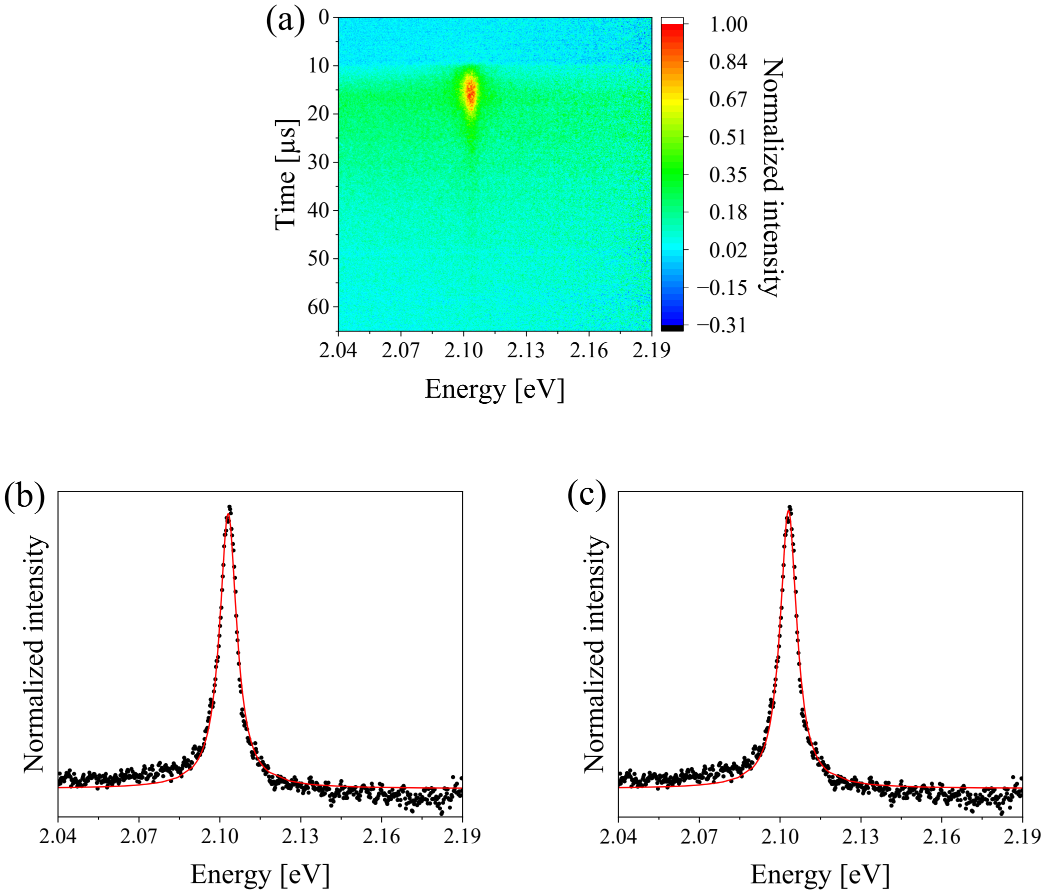

Figure 3.6 – (a) High spectral resolution time-resolved spectrum of emission from TR-explosive around 2.10 eV. Spectral intensity represented small negative value because dark image was subtracted from raw streak image to remove background signal. The detonation reaction occurred for about 13 μs (11–24 μs), and secondary combustion was observed after detonation reaction. (b, c) Time-integrated spectra over the detonation time domain in (a) were indicated as black dots, where baselines were subtracted by linear lines parallel to x-axis. Red lines in (b) and (c) are the Voigt and Lorentz curves, respectively.

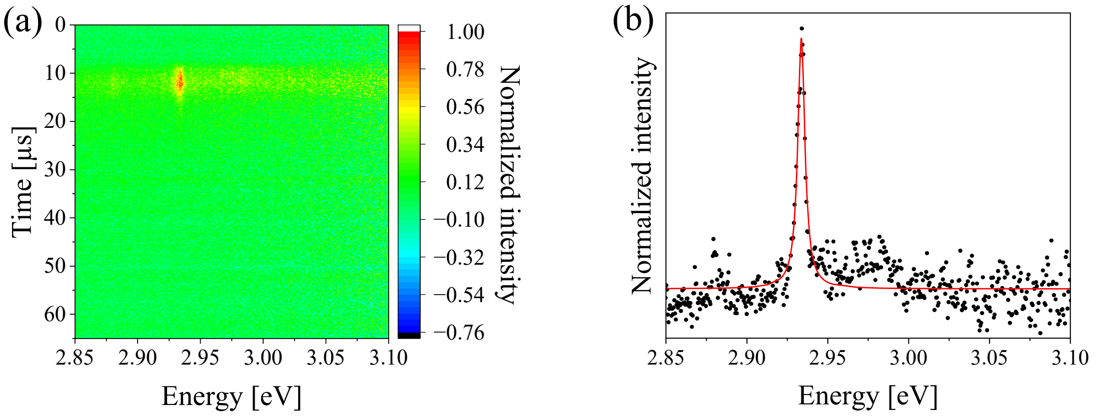

Figure 3.7 – (a) High spectral resolution time-resolved spectrum of emission from TR-explosive around 2.93 eV. Spectral intensity represented small negative value because dark image was subtracted from raw streak image to remove background signal. Detonation reaction occurred for about 13 μs (9–22 μs), and secondary combustion was observed after detonation reaction. (b) Time-integrated spectra over detonation time domain in (a), where baseline was subtracted by a linear line parallel to x-axis. Black dots and a red line indicate original data and fitted Lorentz curve, respectively.

Table 3.2 – Fitting parameters of Voigt and Lorentzian functions for a peak around 2.10 eV of emission from TR-explosive.

Function	F_0 [arb. units]	E_0 [eV]	A [arb. units]	w_G [eV]	w_L [eV]
Voigt	$(9.119 \pm 0.158) \times 10^{-2}$	2.103 ± 0.000	$(1.075 \pm 0.017) \times 10^{-2}$	0.0000 ± 0.1505	$(7.730 \pm 0.280) \times 10^{-3}$
Lorentz	$(9.169 \pm 0.145) \times 10^{-2}$	2.103 ± 0.000	$(1.068 \pm 0.012) \times 10^{-2}$	N.A.[a)]	$(7.590 \pm 0.136) \times 10^{-3}$

[a)] N.A.: Not Applicable.

Table 3.3 – Fitting parameters of Lorentzian function for a peak around 2.93 eV of emission from TR-explosive.

F_0 [arb. units]	E_0 [eV]	A [arb. units]	w_L [eV]
$(1.593 \pm 0.029) \times 10^{-1}$	2.934 ± 0.000	$(6.820 \pm 0.268) \times 10^{-3}$	$(5.370 \pm 0.288) \times 10^{-3}$

3.3.3 Molecular dynamics simulation using ReaxFF

The MD simulation system was well-reproduced with the target conditions of 25 GPa and 3627 K according to the time series of pressure and temperature during equilibration shown in Figure 3.8a. Figures 3.8b and c show the temporal evolution of the main final gaseous products from the TNT molecules and its magnified view of the gas products evolution in the time region from 0 to 3 ps, respectively. The nitro groups were initially eliminated as NO_2 from the TNTs, resulting in N_2 via NO molecules. The O atoms, including nitro groups, reacted with the H atoms at 3,5-positions and the methyl groups of the TNTs and formed OH and H_2O molecules. Productions of CO and CO_2 molecules are negligible. Thus, while the functional groups of the TNT molecules were released into the system as stable low molecular weight compounds, the C_7 carbon skeletons of TNT molecules were not decomposed. The remaining number of C_7 species and the maximum size of carbon clusters at each time were pursued to investigate the behaviors of the carbon atoms, as shown in Figures 3.8d and e. The carbon cluster growth almost stopped at 2 ps with the disappearance of the C_7 species. Subsequently, the behavior of the carbon atoms during this 2 ps period was studied in detail. Figure 3.9a shows the existing number of each carbon species at 0.0, 0.3, 0.7, and 1.1 ps, weighted by the carbon number of itself. The C_7, C_{14}, C_{21}, and C_{28} species were prominently presented. This indicates that the C_7 TNT skeleton structures were polymerized without degradation. The existing number of the carbon species at 1.1 to 2.1 ps is shown in Figures 3.9b and c. Since the relationship between the carbon number of species and their existing number seems linear, each species that includes more than 50 carbon atoms exists only one molecule at any time.

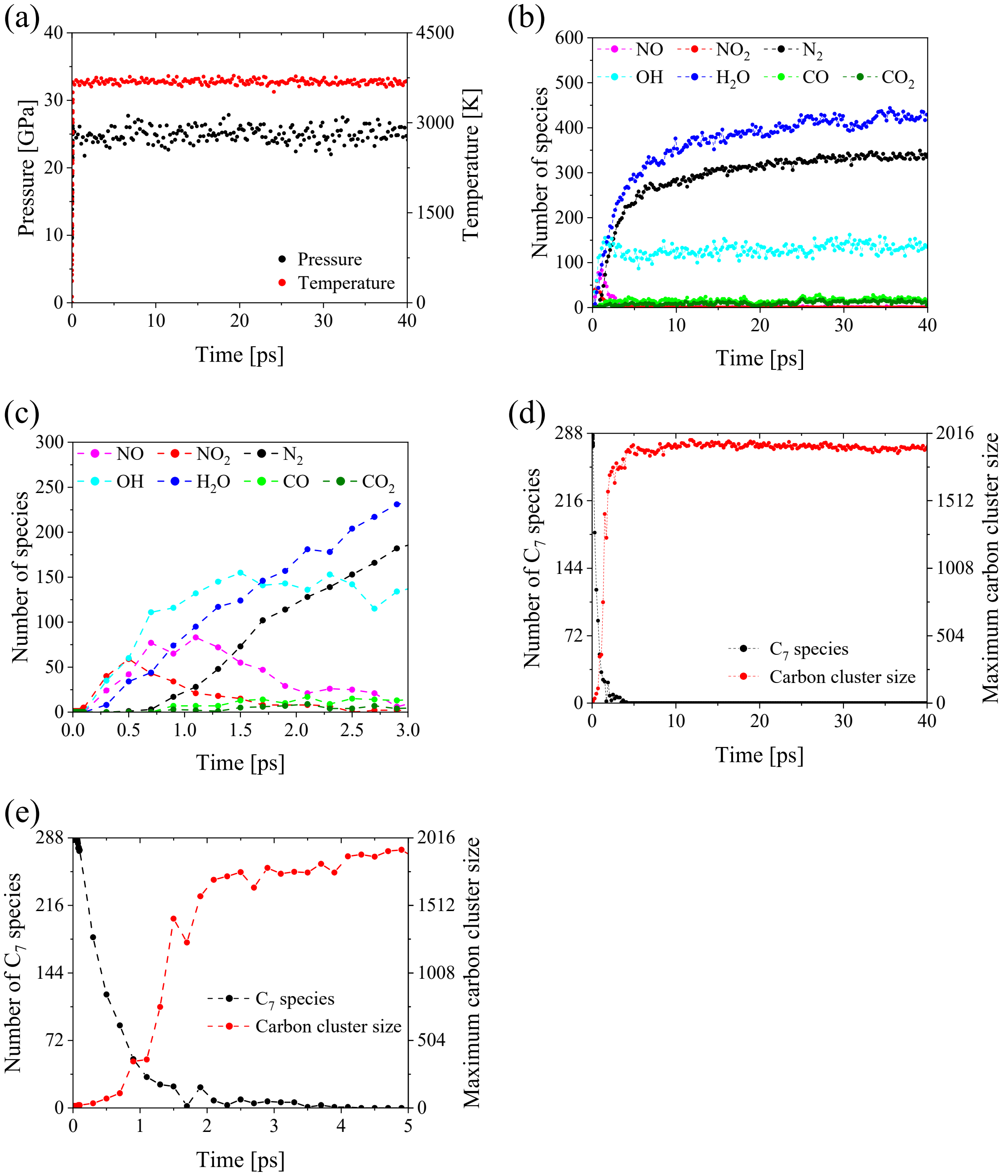

Figure 3.8 – (a) Pressure and temperature histories of simulation system. (b) Temporal evolution of stable gaseous molecules number. (c) Magnified view of (b) in time region from 0–3 ps. (d) Evolution of C_7 species number and maximum cluster size. (e) Magnified view of (d) in time region from 0–5 ps.

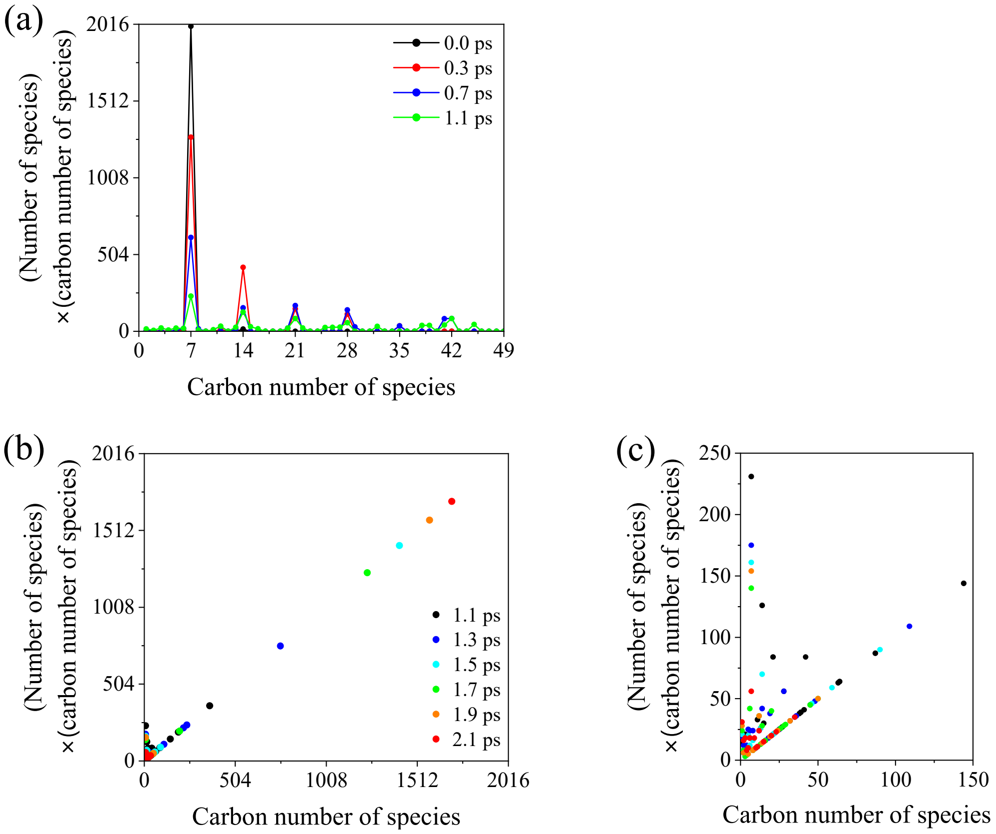

Figure 3.9 – Existence number of carbon species in simulation system during (a) 0.0–1.1 ps and (b) 1.1–2.1 ps. (c) Magnified view of the (b) in carbon number of species region from 0–150. In figures (a, b, c), carbon numbers of species weighted existence numbers.

3.3.4 Formation mechanism of nanodiamond during detonation reaction

The DND formation mechanism is estimated based on the analysis of the time-resolved emission spectra shown in Figure 3.5. Unlike the previous studies (the details are described in Section 1 as the C_2-mechanism), the absence of Swan-band of C_2 in the time-resolved emission spectra indicates that C_2 species were not a significant component in the DND formation process. The alternative mechanisms proposed in this study were C_1- and C_6-mechanisms. The atomic emission of C(I) was observed from the TR-explosive. This atomic emission was not only present in the emission from the TR-explosive but also measured in that from the RDX-explosive. Thus, there is a possibility that the origin of the atomic carbons is the RDX which plays a role in the energy source of the DND formation. However, the observation of the C(I) atomic emission should not be ignored because of its potential to originate from the TNT as a carbon source for the DND. Hence, the C_1-mechanism is proposed in which the atomic carbons (C_1) generated by the decomposition of the TNT molecules function as building blocks for the DND formation. Furthermore, the estimation of the DND formation mechanism is discussed by the results of the MD simulation with ReaxFF. This simulation confirmed that the dimerization and trimerization of the TNTs proceeded while maintaining the carbon skeleton C_7 with the aromatic ring C_6 as TNT core. Such C_6-mechanism is consequently suggested. Although the C_6 or C_7 intermediate species were undetected in the time-resolved emission spectra, asymmetric molecules larger than C_3 cannot be observed in those spectroscopic experiments. Therefore, the C_6-mechanism is not ruled out by the spectroscopic investigations. In summary, the C_1- and C_6-mechanisms are proposed by the time-resolved spectra and the MD simulation with ReaxFF, respectively, where the C_1 or C_6 building blocks couple and aggregate with themselves and then undergo a phase transition from the liquid phase to the diamond phase during the detonation reaction.

3.3.5 Selection of silicon dopant for synthesis of silicon-vacancy center-containing nanodiamonds via detonation process

The silicon compounds shown in Figure 3.10 are selected corresponding to two types of putative DND formation mechanisms, as Si-dopants. For the C_1-mechanism, a tetrakis(trimethylsilyl)silane (TTS) is employed. TTS is not only composed of an abundance of Si atoms, but its central Si atom has four Si–Si bonds with lower bond energy than C–C and C–Si bond energies. These structural features are predicted to release atomic Si readily. The released Si atoms are expected to be in high-frequency contact with the C_1 species derived from TNT molecules and then incorporated into the C_1 condensation process. In the C_6-mechanism, an aromatic silicon compound triphenylsilanol (TPSOH) is adopted. The C_6 building blocks and TPSOH have aromatic ring structures. Since these aromatic rings interact during the detonation reaction, the Si atoms of TPSOH molecules are expected to incorporate into the DNDs. In addition, these Si-dopants can be mixed with TNT and RDX powders well and then molded by pressing to form the cylindrical shape because they are powdery solids at ambient pressures and temperatures (the melting points of TTS and TPSOH are 263–264 and 152–154 °C, respectively [126, 127]). The detonation experiments of the SiV-DND synthesis in which these Si-dopants were used are described in Chapter 4. The C_1- and C_6-mechanisms also are evaluated from results of the SiV-DND syntheses.

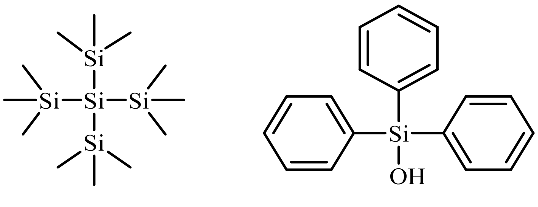

TTS TPSOH

Figure 3.10 – Chemical structures of TTS and TPSOH.

3.4 Summary

The study on the DND formation mechanism at the molecular level was performed using the time-resolved emission measurements and the MD simulation with ReaxFF. The time-resolved spectrum of the emission from the TR-explosive recorded the atomic carbon C_1 emission. On the other hand, the MD simulation showed dimer- and trimerization of TNT molecules while maintaining their carbon skeleton C_7 with the aromatic ring C_6. Hence, the C_1- and C_6-mechanisms were proposed, in which the C_1 and C_6 species function as the building blocks for the diamond structure construction, respectively. In addition, the TTS and TPSOH were selected as the Si-dopants corresponding with the C_1- and C_6-mechanisms for the SiV-DNDs synthesis by the detonation process, respectively.

.

Chapter 4. Synthesis of silicon-vacancy center-containing nanodiamonds via detonation process

4.1 Introduction

In the previous chapter, the two types of Si-dopants were selected corresponding to the proposed mechanisms. The SiV-NDs syntheses by the detonation process using explosives with these Si-dopants individually are tried in this chapter. The SiV-ND has attracted considerable attention as an ideal fluorescent marker for bioimaging because of biocompatibility of the ND and excellent optical properties of the SiV^- center [10]. The SiV^- center exhibits narrow and strong ZPL at 1.68 eV [52, 58]. The ZPL is known to have a spectra width of ~11.4 meV and to possess a small PSB as ~70% of its total luminescence is concentrated in the ZPL [51, 65]. This prominent luminescence lying in a near-infrared biological window (1.38–1.77 eV) is available for observations in living cells [128, 129], which can be excited by near-infrared light [65]. In addition, the SiV^- centers in bulk-sized diamonds and 200 nm-sized NDs have shown temperature sensitivity down to 0.36 and 0.52 K $Hz^{-1/2}$ around room temperature, respectively [61]. Thus, the SiV-ND is also expected to be applied to nanoscale temperature sensing in living cells. In 2022, intracellular imaging and thermometry using the SiV-NDs were realized by Liu *et al.* [130]. Given this background, numerous fabrication studies for the SiV-NDs have been carried out thus far: HPHT, CVD, and ion implantation techniques are well known [70, 76, 79, 85, 86]. Nevertheless, no technique has been discovered to produce the SiV-NDs on a practical scale. The establishment of the SiV-NDs mass production technique is required for their practical application as fluorescent markers. Therefore, researchers have been focused on the detonation process that produces NDs through the detonation of explosives such as the mixture of TNT and RDX. Because of its straightforward procedures, DNDs can be synthesized on a practical scale [91–93]. In addition, the DNDs exhibit two unique features for biomedical applications, as follows. First, the DNDs can move into living cells through the membrane because their small particle size of 4–5 nm is comparable to the size of typical biomolecules such as proteins [88, 89]. Second, the DND surface is naturally covered with functional groups enabling modification with various chemical compounds [131]; therefore, the surface modifications allow their dispersion in a wide range of media [132–134]. The production of SiV-NDs via the detonation process has been actively studied using explosives containing various Si-dopants [90]. However, there has been no successful fabrication of the SiV-DNDs directly to date. In this study, the SiV-NDs synthesis is performed by the detonation process (SiV-DNDs) using the explosives containing each Si-dopant. Furthermore, the chemistry behind the successful synthesis of the SiV-DNDs is discussed in terms of the DND formation mechanism at the molecular level.

4.2 Experimental detail in Chapter 4

The standard explosive generally used to produce undoped-DNDs is a mixed explosive consisting of 60 wt% TNT and 40 wt% RDX prepared by compression to form a cylindrical charge of 60 g as the total mass. This explosive was referred to as the TR-explosive in Chapters 2 and 3, which was also employed in the time-resolved emission measurements described in Chapter 3.3.2. In the study of this chapter, the SiV-DNDs synthesis was performed using the TR-explosive with the Si-dopants selected in Chapter 3.3.5: TTS (Tokyo Chemical Industry Co., Ltd.) or TPSOH (Tokyo Chemical

Industry Co., Ltd.). 0.6 g of each Si-dopant was added in 60 g of the TR-explosive preparation (hereinafter referred to as “Si-explosive”). Both Si-dopants are powdery solids at room pressure and temperature because TTS and TPSOH melting points are 263–264 and 152–154 °C, respectively [126, 127]. Therefore, they could be well mixed with TNT and RDX powders. The resultant mixtures could be molded by pressing into a cylindrical shape. Each Si-explosive was detonated under a CO_2 atmosphere. The detonation products were purified by acid treatment, alkali treatment, and air-oxidization at 470 ºC for 2 h. These purified samples were confirmed to be DNDs by powder XRD analyses and TEM observations. Subsequently, the creation of the SiV^- centers in DNDs was investigated by PL measurements for their drop-cast samples. These original methods were described in Chapter 2.1.

The isolation of single-digit nanometer-sized DNDs from the *as-purified* DNDs was performed with reference to the method of Stehlik *et al.* [135], as follows. A colloidal solution was prepared from 12 mg of the DNDs with 8 mL of DI water, followed by sonication using an ultrasound horn (UP-400S, Hielscher Ultrasonics) at 120 W for 1 h to ensure proper dispersion. The dispersion was centrifuged (CR22G, Hitachi Koki) at 13200 × *g* for 1 h. The supernatant (up to 4 mm deep from the liquid level) was collected carefully using a micropipette, which was characterized by the PL measurement after drying on a glass substrate as a drop-cast sample.

The detonation reactions of the Si-explosives containing TTS or TPSOH were observed by time-resolved emission spectroscopy. These observations were carried out by the identical method as in the time-resolved emission measurements of the detonation from the TR-explosive described in Chapter 3.2.3. In these measurements, amounts of the Si-dopants were used ten times (6 g) as much as the SiV-DNDs synthesis for more apparent observation of dopant-attributed emission.

4.3 Results

4.3.1 Structural characterization

XRD patterns of the purified detonation products obtained from the two types of Si-explosives are shown in Figure 4.1. The products were confirmed to have a diamond crystal structure as three major diffraction peaks, originating from (111), (220), and (311) planes, were explicitly observed. Graphite peaks were not observed. The average crystalline sizes of the diamonds obtained from the Si-explosives including TTS or TPSOH were calculated on the basis of each (111) diffraction peaks using Scherrer's formula were 7.1 or 7.4 nm, respectively. In addition, TEM images of the aggregated diamonds produced by the Si-explosives are shown in Figures 4.2a and b. The particle sizes in the TEM images were calculated assuming a spherical shape. The particles with unclear boundaries of adjacent particles were not included in the calculation, such as those shown by the yellow squares in the TEM images. The calculation results as particle size distributions of their diamonds are shown in Figure 4.2c. The most frequently observed particle sizes of the diamonds obtained from the Si-explosives containing TTS and TPSOH roughly matched the respective average crystallite sizes based on the powder XRD analyses. According to these characterizations, DNDs were produced from the Si-explosives as in a well-known detonation process, irrespective of the dopants. The DNDs obtained by the Si-explosives containing TTS and TPSOH are hereinafter individually-referred to as “TTS-DNDs” and “TPSOH-DNDs.”

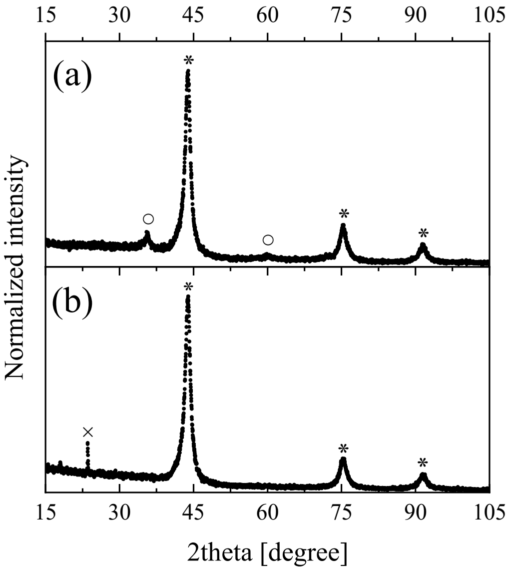

Figure 4.1 – XRD patterns of detonation products obtained from Si-explosives including (a) TTS and (b) TPSOH. Asterisks, circles, and a cross denote cubic diamond structure, cubic silicon carbide structure, and a spike noise, respectively.

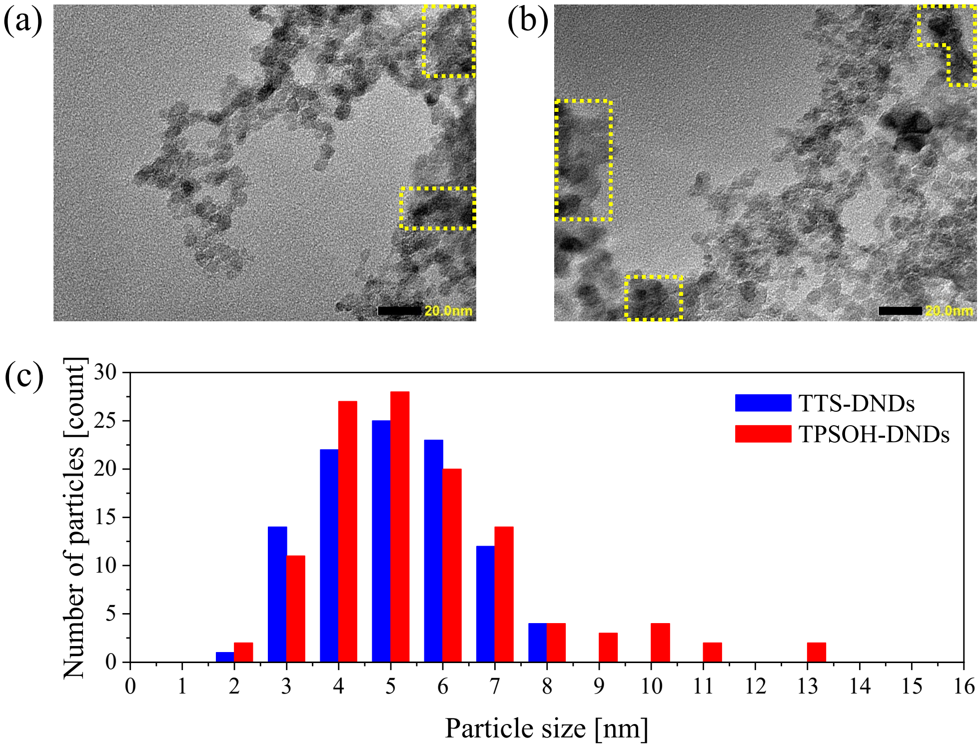

Figure 4.2 – TEM images of aggregated diamonds produced by Si-explosives containing (a) TTS or (b) TPSOH. (c) Particle size distributions made by TEM images (a, b). Yellow squares in (a) and (b) are areas of particle sizes that were excluded from calculations owing to unclear boundaries between adjacent particles.

4.3.2 Photoluminescence measurement

PL measurements were performed at room temperature for the drop-cast samples of the TTS- and TPSOH-DNDs which were densely packed on the glass substrate. Figures 4.3a and b show normalized PL intensity maps at 1.68 eV which is the ZPL of the SiV^- center [52, 65], for the TTS- and TPSOH-DNDs, respectively. Each map comprises 10201 spots, each corresponding to a 1 × 1 μm region. Figures 4.3a' and b' show representative PL spectra for the TTS- and TPSOH-DNDs, corresponding to spots 1 and 2 indicated in Figures 4.3a and b, respectively. One can see that only the TPSOH-DNDs have a distinct peak centered at 1.68 eV in their PL spectrum, suggesting that the SiV-DNDs were successfully synthesized via the detonation process using the Si-explosive containing TPSOH as the silicon source. In this study, the experimental procedures do not include an annealing process to couple the Si atoms and the carbon vacancies required in the general process to prepare the split-vacancy structure which is a Si atom lying between two carbon vacancies (the structure described in Chapter 1.2) [136]. Although the air-oxidation was performed at 470 ºC as a post-treatment to remove trace amounts of sp^2 carbon, it is generally insufficient to form the SiV structure under such temperature. According to one of the reports, an even at a temperature of 800 ºC could not combine the Si atom and the vacancies in DND [137]. Hence, the SiV^- centers were directly formed during the DND formation process.

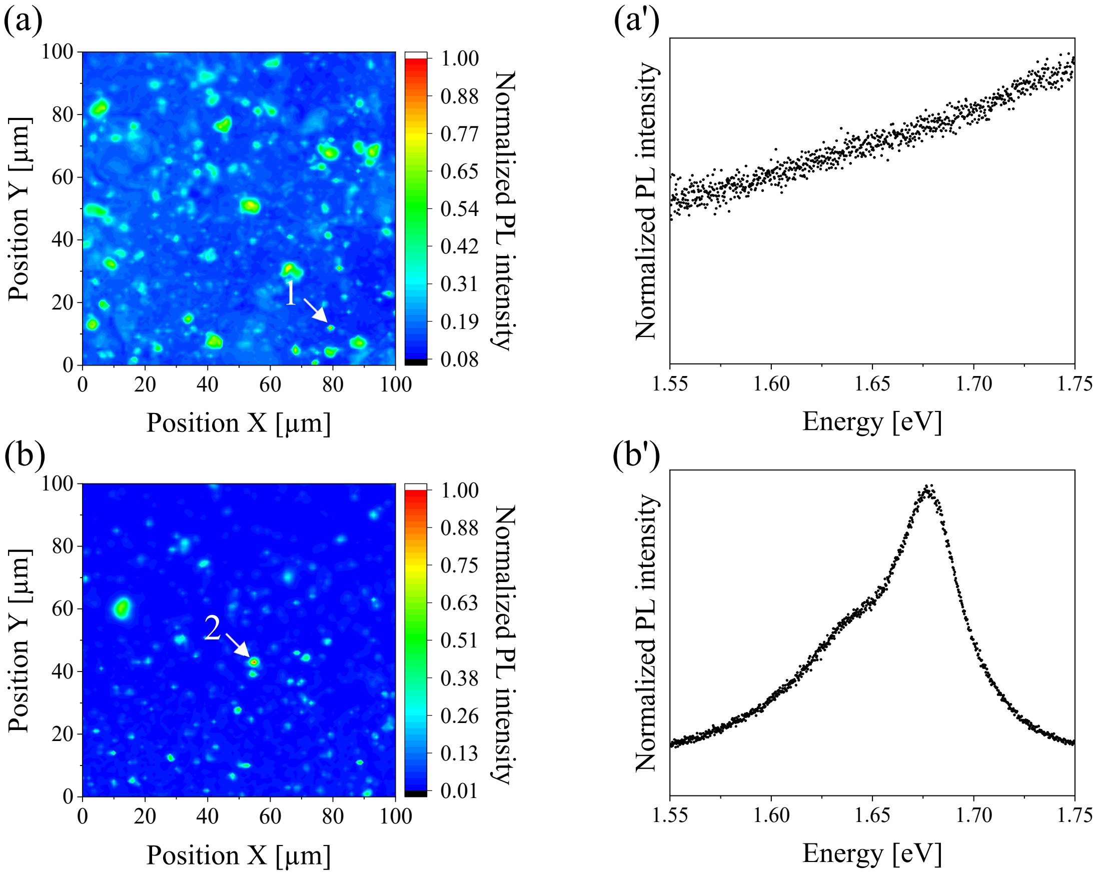

Figure 4.3 – Results of PL measurements on DNDs produced from Si-explosives. Intensity mapping of PL at 1.68 eV for (a) TTS- and (b) TPSOH-DNDs. Representative PL spectra corresponding to spots 1 and 2 indicated in (a, b) are shown in (a') and (b'), respectively.

The TPSOH-DNDs contain aggregates and minor larger (>10 nm size) diamond particles according to their TEM image shown in Figures 4.2b and c. Here, single-digit nanometer-sized TPSOH-DNDs were isolated from such large particles following the method stated in Section 2 and subsequently evaluated the construction of SiV^- centers by PL spectroscopy. The TPSOH-DNDs were ultrasonicated and then centrifuged ($13200 \times g$, 1 h). The supernatant after centrifugation was collected at a depth in the range of 4 mm from the liquid level. The sedimentation velocity V_{sed} of the particle in a solvent is expressed by [138]

$$V_{\mathrm{sed}} = \frac{2gr^2(\rho_{\mathrm{p}} - \rho_{\mathrm{s}})}{9\mu}, \tag{4.1}$$

where g is gravitational acceleration, r is the radius of the particle, ρ_{p} and ρ_{s} are the density of the diamond particles and solvent, and μ is the solvent's viscosity, respectively. According to Equation 4.1, V_{sed} of the >10 nm-sized DNDs centrifuged at 13200 × g was calculated to be >6.4 mm h^{-1}. Therefore, the collected supernatant (up to 4 mm deep from the level) should contain only single-digit nanometer-sized DNDs. The isolated single-digit nanometer-sized TPSOH-DNDs exhibited the ZPL of SiV^{-} center at 1.68 eV in their PL spectrum, as shown in Figure 4.4. Thus, the single-digit nanometer-sized SiV-DNDs were synthesized via the detonation process.

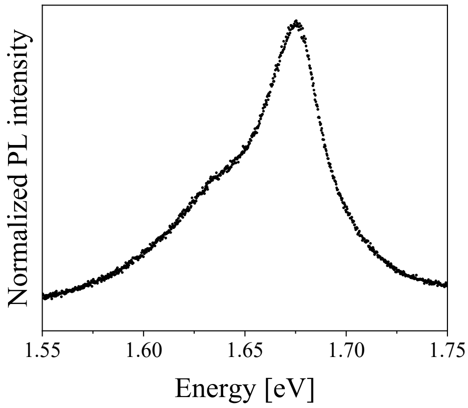

Figure 4.4 – PL spectrum of separated single-digit nanometer-sized SiV-DNDs.

4.3.3 Time-resolved emission measurement

Temporal evolutions of the detonation reactions from the Si-explosives were observed using time-resolved emission spectroscopy. Figures 4.5a and b show time-resolved spectra of the detonation emission from the Si-explosives containing TTS and

TPSOH, respectively. Their time and energy resolutions are 130 ns and 0.006 eV, respectively. According to the high-speed camera observations studied in Chapter 3.3.1, the time domain of the detonation reaction is 13 μs from the first recording of prominent emission in the time-resolved spectra (12–25 and 11–24 μs in Figures 4.5a and b, respectively). Figures 4.5a' and b' show time-integrated spectra during the detonation reaction times in Figures 4.5a and b, respectively. As with the emission from the TR-explosive explained in Chapter 3.3.2, these spectra could not be fitted with Planck distribution and showed sharp peaks at 2.10 and 2.93 eV assigned with C(I) [$2s^2 2p3p$–$2s^2 2p7s$] and O(II) [$2s^2 2p^2(^3\mathrm{P})3d$–$2s^2 2p^2(^3\mathrm{P})4f$], respectively. Other small peaks at 1.90, 2.24, 2.52, and 2.72 eV are consistent with the detonation emission from RDX (described as the RDX-explosive in Chapter 3.3.2). It is noteworthy that a unique peak at 1.84 eV was observed only in the detonation reaction of the Si-explosive containing TTS (Figure 4.5a and a'). Therefore, a high-resolution experiment was additionally performed to assign this unique peak according to the procedure described in Chapter 3.2.2. Figure 4.6a shows a high-resolution time-resolved emission spectrum around the peak position, measured using a finer grating with a spectral resolution of 0.0003 eV. Figure 4.6b offers an extracted spectrum; this was made by integrating over the time ranges of 14–27 μs, corresponding to the detonation reaction time in Figure 4.6a. The peak in the extracted spectrum was well-fitted with a Lorentz curve as a red line in Figure 4.6b. The peak energy is 1.848 eV according to the fitting parameters summarized in Table 4.1 and subsequently is assigned to a Si(IV) [$2p^6 5p$–$2p^6 5d$] atomic emission with reference to the NIST atomic spectra database [120].

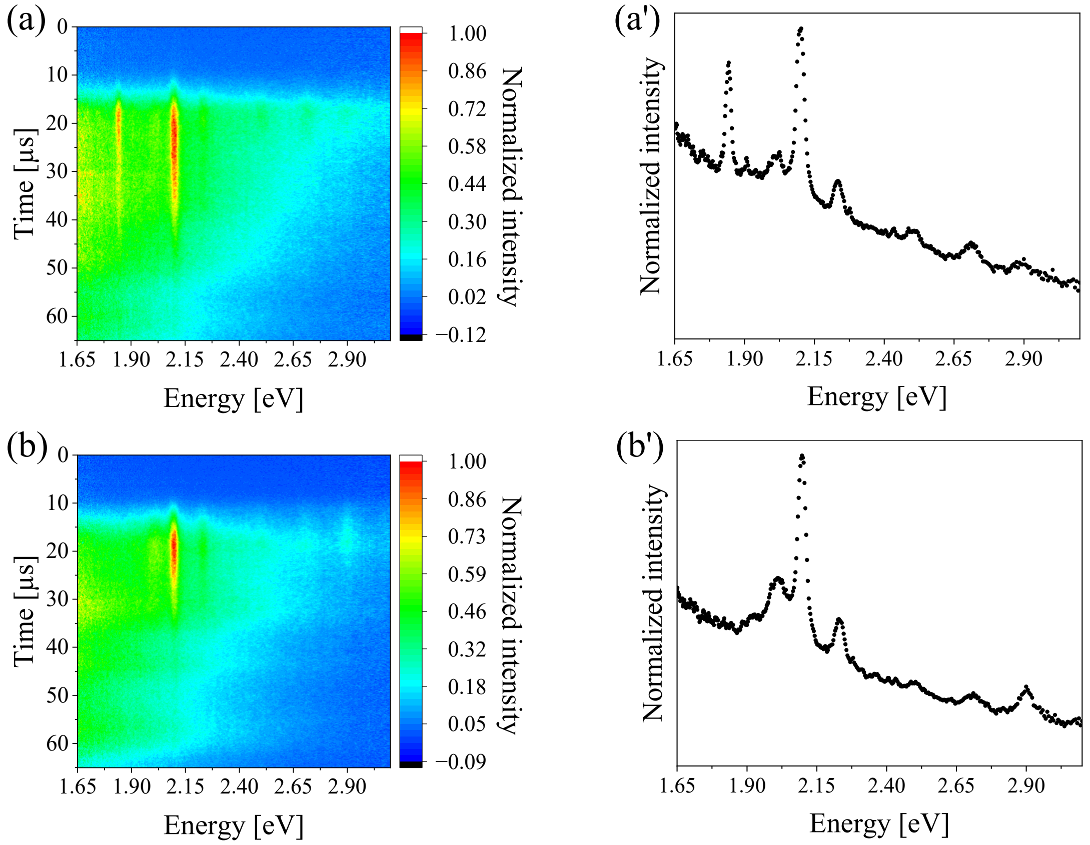

Figure 4.5 – Time-resolved spectra of emission from Si-explosives containing (a) TTS and (b) TPSOH. Spectral intensities in (a) and (b) represented small negative values because dark images were subtracted from raw streak images to remove background signals. Detonation reactions occurred for 13 µs (TTS: 12–25 µs, TPSOH: 11–24 µs), and secondary combustions were observed after the detonation reactions. (a') and (b') are time-integrated spectra over the detonation reaction time domains in (a) and (b), respectively.

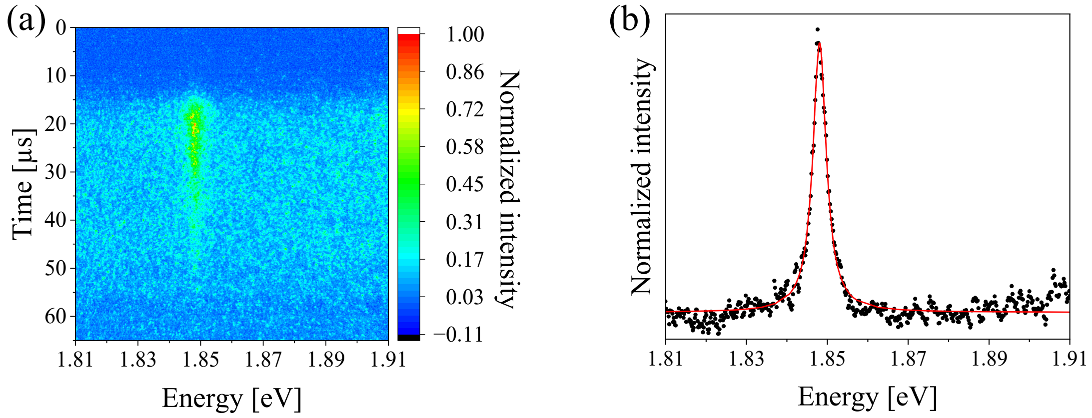

Figure 4.6 – (a) High spectral resolution time-resolved spectrum of emission from Si-explosive containing TTS around 1.84 eV. Spectral intensity represented small negative value because dark image was subtracted from raw streak image to remove background signal. Detonation reaction occurred for about 13 µs (14–27 µs), and secondary combustion was observed after detonation reaction. (b) Time-integrated spectra over detonation time domain in (a), where baseline was subtracted by a linear line parallel to x-axis. Black dots and a red line indicate original data and fitted Lorentz curve, respectively.

Table 4.1 – Fitting parameters of Lorentzian function for a peak around 1.84 eV of emission from TR-explosive.

F_0	x_c	A	w_L
$(8.654 \pm 0.162) \times 10^{-2}$	1.848 ± 0.000	$(5.530 \pm 0.082) \times 10^{-3}$	$(4.050 \pm 0.080) \times 10^{-3}$

4.4 Discussion

TTS and TPSOH as Si-dopants were selected based on the C_1- and C_6-mechanisms for the DND formation proposed in Chapter 3.3.5, respectively. In the C_1- and C_6-mechanisms, atomic carbons (C_1) and aromatic rings (C_6) derived from TNTs function as building blocks for the diamond structure construction, respectively. The successful synthesis of the SiV-DNDs is explained by focusing on the chemical structures of the Si-dopants (the chemical structure is shown in Figure 3.10) and the proposed mechanisms. In the C_1-mechanism, atomic Si should be incorporated into the carbon condensation process because they are the same atomic species as the C_1 building blocks. TTS was selected as a compound with high Si atom content, whose covalent bonds are readily cleaved. The time-resolved emission spectra (Figures 4.5 and 4.6) demonstrated the release of the atomic Si from TTS. Nevertheless, the SiV-DNDs were not produced by the Si-explosive containing TTS. It suggests the non-intervention of atomic Si in the C_1 species condensing process and the invalidity of the C_1-mechanism. One interpretation of the C_1 atomic emission observed in the time-resolved spectra is that C_1 originates only from RDX which does not supply carbons to the DNDs and creates high-pressure and high-temperature conditions. On the other hand, TPSOH selected by the C_6-mechanism led to the SiV-DNDs synthesis. The TPSOH selection was because the three aromatic rings bonded to a Si atom in its chemical structure should allow for the aromatic interaction with the C_6 building blocks during the detonation reaction. The absence of Si atomic emission in the time-resolved spectra indicated in Figures 4.5b and b' suggest that the chemical structure of TPSOH could be maintained in whole or in part during the detonation reaction. Thus, the combination of the aromatic rings-containing TPSOH chemical structure and the C_6-mechanism can explain the achievement of the SiV-DNDs synthesis. The discussion above not only explains the reason for the successful synthesis of the SiV-DNDs but also proposes the C_6-mechanism as a promising DND formation mechanism at the molecular level.

4.5 Summary

The SiV-DNDs synthesis was performed using explosives containing TTS or TPSOH. Only the DNDs obtained from the explosives with TPSOH showed the PL spectrum including the peak at 1.68 eV corresponding to the ZPL of SiV^- center. Hence, the SiV-DNDs synthesis was realized by employing TPSOH as Si-dopant. According to the time-resolved emission spectra of the detonation reactions from each explosive, TTS was decomposed to atomic Si, whereas TPSOH partially or wholly maintained its chemical structure, during the detonation reactions. Combining these optical experimental results with the C_6-mechanism proposed in Chapter 3, the achievement of the SiV-DNDs synthesis can be explained by the aromatic–aromatic interactions between TPSOH and the C_6 diamond building blocks derived from TNT molecules as the DND carbon source. The control of the detonation reactions based on the C_6-mechanism leads to further discussion of the *in situ* doping of hetero atoms into DNDs by the detonation process from the molecular reaction mechanism perspective.

Chapter 5. Synthesis of three types of group IV-vacancy center-containing nanodiamonds by detonation process using aromatic compounds as group IV element sources, and its mechanism

5.1 Introduction

In the previous chapter, the practical scale synthesis of SiV-NDs is demonstrated by the detonation process, which produces NDs with 7 nm on average through the detonation of the mixed explosives consisting of TNT, RDX, and an aromatic Si compound. The detonation process with the aromatic compound was expanded to synthesize the other G4V-NDs in this chapter. The GeV$^-$ and SnV$^-$ centers are other types of G4V$^-$ centers composed of elements with larger atomic numbers than the SiV$^-$ center. The GeV$^-$ and SnV$^-$ centers exhibit strong and sharp ZPLs at 2.06 and 2.00 eV as well as the SiV$^-$ center, respectively [52, 64]. Therefore, the GeV- or SnV-NDs have also emerged as promising candidates for fluorescent markers and single-photon sources [10, 64]. In particular, there is a strong demand to synthesize single-digit nanometer-sized GeV- and SnV-ND particles for applications of fluorescent markers owing to their low accumulation in the body. The fabrications of their high crystalline particles have been achieved via HPHT and CVD techniques [69, 80]. However, the method to synthesize large quantities of single-digit nanometer-sized GeV- and SnV-NDs, which is necessary for their practical applications, has not been found. In this study, the GeV- and SnV-NDs syntheses were carried out by the detonation process (GeV- and SnV-DNDs, respectively) with the aromatic compound as dopants. In addition, the SiV-DNDs were resynthesized to compare the amounts of the GeV- and SnV- DNDs produced under the same conditions. The thermodynamics and kinetics of the detonation reactions for the G4V-DNDs production are discussed, and the reasons for the success and limitation of their direct synthesis are explained.

5.2 Experimental detail in Chapter 5

5.2.1 Synthesis and structural characterization

The typical detonation process for the DNDs production was performed using a mixed explosive consisting of 60 wt% and 40 wt% RDX by compression to form a cylindrical charge with a total mass of 60 g. This mixed explosive was referred to as the TR-explosive in Chapters 2–4 and was also referred to in this chapter. For the G4V-DNDs synthesis, 0.6 g of each dopant was added in the course of the TR-explosive preparation. Tetraphenylsilane (TPS; Tokyo Chemical Industry Co., Ltd.), tetraphenylgermane (TPG; Tokyo Chemical Industry Co., Ltd.), and tetraphenyltin (TPT; Tokyo Chemical Industry Co., Ltd.), whose chemical structures are shown in Figure 5.1, were selected as the group IV dopants (hereinafter referred to as "Si-, Ge-, and Sn-explosives," respectively). Melting points of TPS, TPG, and TPT are 235–238, 231–233, and 226–228 °C, respectively [139–141]. All dopants are powdery solids at ambient pressure and temperature; therefore, they could be well mixed with TNT and RDX powders. The resultant mixtures could be molded by pressing into a cylindrical shape. The bulk densities of the TR-, Si-, Ge-, and Sn-explosives were 1.52, 1.54, 1.55, and 1.55 g cm^{-3}, respectively. All of the explosives were individually detonated under a CO_2 atmosphere. The detonation products were purified by the acid-, alkali treatments and air-oxidization at 470 °C for 2 h. These purified sample structures were characterized by powder XRD analyses, XRF measurements, and TEM observations. The formation of $G4V^-$ centers in DNDs generated from the four kinds of explosives was investigated by PL measurements. These original methods were described in Chapter 2.1.

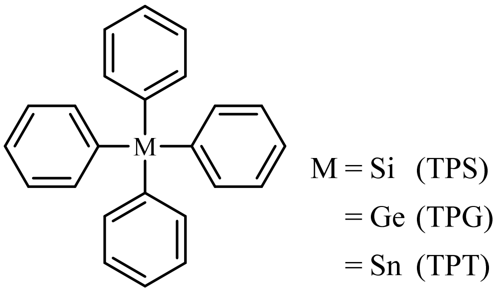

Figure 5.1 – Chemical structures of dopants: TPS, TPG, and TPT.

5.2.2 Quantum chemical calculation

Free energies of the group IV dopants ($C_{24}H_{20}M$, M: Si, Ge, and Sn), group IV dioxides (MO_2), and the G4V-DNDs were calculated by following procedures: (i) investigation of their optimized geometries; (ii) calculations of their total electronic energies and corrections of their thermal free energies. These corrections were considered under 3675 K as the temperature of the detonation reaction. This temperature is the conditions at the CJ point (the details described in Chapter 1.4) of the 1.6 g cm^{-1} mixed explosive consisting of 60 wt% TNT and 40 wt% RDX used for the DNDs productions [116].

5.2.2.1 Geometry optimization

The conformers of the group IV dopants—TPS ($C_{24}H_{20}Si$), TPG ($C_{24}H_{20}Ge$), and TPT ($C_{24}H_{20}Sn$)—were generated by rotating the four phenyl groups at 120-degree intervals, and the molecular mechanical energies were evaluated using the CONFLEX program in SCIGRESS [142, 143]. The two most stable conformers were then identified among all the generated conformers, which have C_1 and C_{2v} symmetries. The most stable conformer of each group IV dopant was determined by evaluating the total electronic energies of the two conformers at the DFT/B3LYP/def2-SVP level of theory using the Gaussian 16 package and by comparing them with each other [144]. The optimized geometries of the group IV dopants are shown in Figure 5.2, all of which have C_1 symmetry. The four bond lengths between the group IV atom and phenyl carbon atom are the same as each other, and the bond lengths in TPS, TPG, and TPT are 0.190, 0.197, and 0.217 nm, respectively.

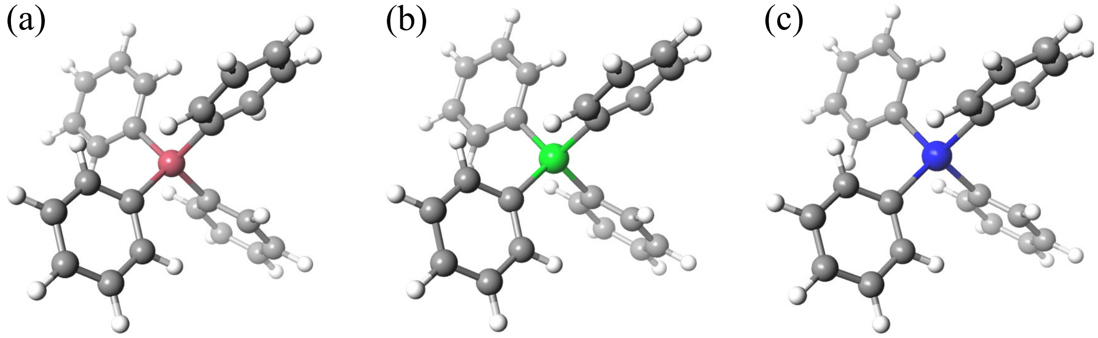

Figure 5.2 – Structural models after optimization of group IV dopants ($C_{24}H_{20}M$, M denotes a group IV atom): (a) TPS ($C_{24}H_{20}Si$), (b) TPG ($C_{24}H_{20}Ge$), and (c) TPT ($C_{24}H_{20}Sn$). Gray and white balls represent carbon and hydrogen atoms, respectively. Pink, green, and blue balls denote silicon, germanium, and tin atoms, respectively.

The group IV dioxides—silicon dioxide (SiO_2), germanium dioxide (GeO_2), and tin dioxide (SnO_2)—are considered to be in the gas phase because they exist under detonation processes with 3675 K. Therefore, these dioxides were dealt with as molecules in the gas phase and optimized their geometries at the DFT/B3LYP/def2-SVP level of theory using the Gaussian 16 package [144], as shown in Figure 5.3. The bond lengths between group IV and oxygen atoms in SiO_2, GeO_2, and SnO_2 are 0.152, 0.163, and 0.184 nm, respectively.

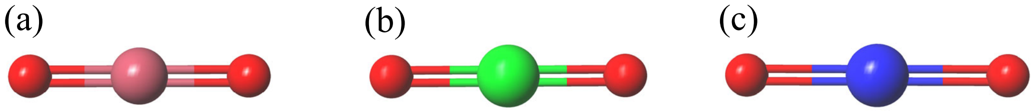

Figure 5.3 – Structural models after optimization of group IV dioxides (MO_2): (a) silicon dioxide (SiO_2), (b) germanium dioxide (GeO_2), and (c) tin dioxide (SnO_2). Red, pink, green, and blue balls represent oxygen, silicon, germanium, and tin atoms, respectively.

Model compounds of the G4V-DNDs (SiV-, GeV-, and SnV-DND) used in these calculations were adopted and then optimized. In each $G4V^-$ center, a corresponding group IV atom (M: Si, Ge, and Sn) lies between two nearest-neighbors carbon vacancies (V) in a diamond, and the molecular structure has D_{3d} symmetry [55–57]. Therefore, each G4V-DND model compound should be constituted as its geometry maintains D_{3d} symmetry. Moreover, although even a spherical DND particle of 4.2 nm size comprises almost 7000 carbon atoms [145], the number of constituent atoms in the adopted model compounds is subjected to restriction by at most a few hundred carbon atoms owing to the limitation of the computational cost for quantum chemical calculation. Under these conditions, H-terminated carbon clusters $C_{104}[V\text{-}M\text{-}V]^-H_{86}$ with each $G4V^-$ center represented by "$[V\text{-}M\text{-}V]^-$" laid in its central position, which has a doublet spin state [65, 83, 146–148], were adopted as the model compounds. Geometric optimizations of the cluster models $C_{104}[V\text{-}M\text{-}V]^{-}H_{86}$ were conducted at the DFT/B3LYP/def2-SVP level of theory using the Gaussian 16 package under the restriction of preserving the D_{3d} symmetry to reproduce the diamond structure containing a $G4V^{-}$ center [144]. The optimized geometries are shown in Figure 5.4. The six interatomic distances between the group IV atom and the first adjacent carbon atoms are identical. The distances in $C_{104}[V\text{-}Si\text{-}V]^{-}H_{86}$, $C_{104}[V\text{-}Ge\text{-}V]^{-}H_{86}$, and $C_{104}[V\text{-}Sn\text{-}V]^{-}H_{86}$ are 0.201, 0.205, and 0.214 nm, respectively. The clusters can be considered adequate model compounds of the G4V-DNDs for the following reasons. Firstly, the terminal H atoms do not significantly influence the electronic state of the $G4V^{-}$ center because the H atoms are remote from the group IV atom beyond more than three chemical bonds. Secondly, the structural deviations between the second and third adjacent carbon atoms of the group IV atom in $C_{104}[V\text{-}M\text{-}V]^{-}H_{86}$ and those in $C_{104}[C\text{-}C]H_{86}$ are very small by 0.005-0.006 nm $atom^{-1}$; $C_{104}[C\text{-}C]H_{86}$ is a reference compound of the undoped-DND and is optimized by the same quantum chemical method because its geometry maintains the D_{3d} symmetry [83, 147, 149]. Therefore, if the fourth adjacent carbon atoms are added to the clusters, and these clusters are subsequently optimized, the fourth adjacent carbon atoms hold the corresponding positions of the carbon atoms in an ideal diamond crystal. It is thus unnecessary to add such fourth adjacent carbon atoms from a geometrical point of view.

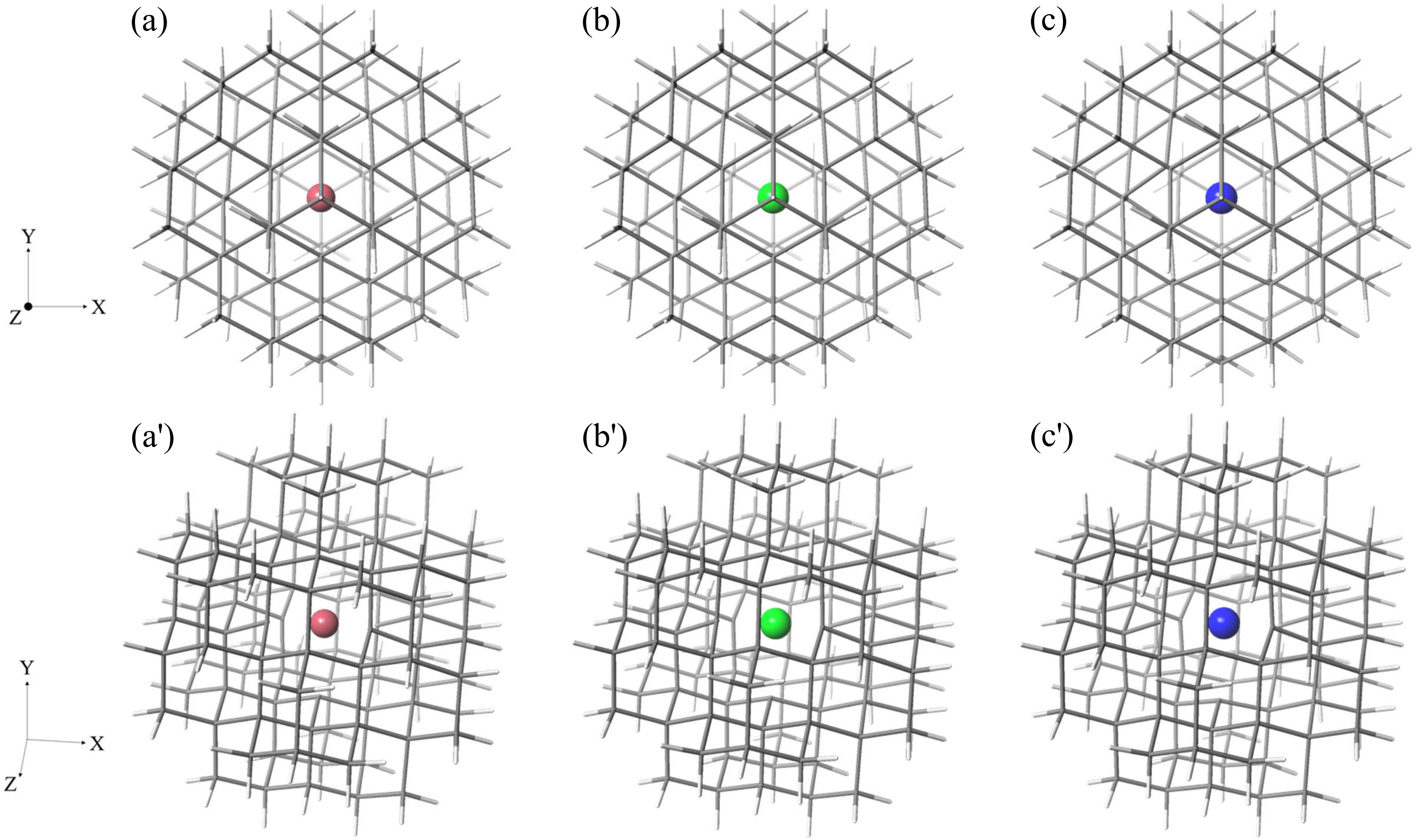

Figure 5.4 – Structural models after optimization of H-terminated carbon cluster model compounds of G4V-DNDs (C_{104}[V-M-V]$^{-}H_{86}$). Model compounds of the SiV-, GeV- and Sn-DND are (a) C_{104}[V-Si-V]$^{-}H_{86}$, (b) C_{104}[V-Ge-V]$^{-}H_{86}$, and (c) C_{104}[V-Sn-V]$^{-}H_{86}$, respectively. Figures in (a-c) are drawn from the (111) plane, and the side views of the (a-c) figures are shown in (a'-c'), respectively. Gray and white sticks denote carbon and hydrogen atoms, respectively. Pink, green, and blue balls represent silicon, germanium, and tin atoms, respectively.

5.2.2.2 Calculation of total electronic energy and correction of thermal free energy

The total electronic energies of the group IV dopants ($C_{24}H_{20}M$), group IV dioxides (MO_2), and G4V-DND model compounds ($C_{104}[V\text{-}M\text{-}V]^{-}H_{86}$) were calculated at their optimized geometries. Their thermal free energy corrections were evaluated by vibrational analysis under 3675 K. As a prerequisite, the method supposes the vibrational partition functions that can be derived based on harmonic oscillator approximations [150]. At the detonation reaction temperature, the compounds in this system vibrate with large amplitudes. Subsequently, the corresponding harmonic oscillator partition functions may not start to correct the thermal free energy properly. An analogous carbon system has been studied by similar methods for correction of the thermal free energies, where stabilities of metallofullerenes and C_{13} carbon clusters were investigated in 0–4500 K [151, 152]. According to these previous studies, the method can be applied to the high-temperature condition at the detonation reaction.

5.3 Results

5.3.1 Structural characterization

XRD patterns of the purified detonation products obtained from the TR-, Si-, Ge-, and Sn-explosives are shown in Figure 5.5. All the patterns show three major diffraction peaks that originate from the (111), (220), and (311) planes of the diamond. Therefore, all products were confirmed to have diamond crystal structures. The average crystallite sizes of the diamonds were calculated on the basis of (111) diffraction peaks in each pattern using Scherrer's formula, which are approximately particle sizes of the DNDs. In the diamonds produced from the TR-, Si-, Ge-, and Sn-explosives, the average crystallite sizes were 6.3, 7.7, 7.2, and 5.9 nm, respectively. The particle sizes were verified by the TEM observations. Figures 5.6a–d show TEM images of the diamonds produced by the TR-, Si-, Ge-, and Sn-explosives, respectively. The particle sizes in the TEM images were calculated assuming a spherical shape. The calculation did not include parts with unclear boundaries of adjacent particles, such as those shown by the yellow squares in the TEM images. Figure 5.6e shows the particle size distributions calculated from the TEM images. The particle sizes were distributed from a few nanometers to larger than 10 nm. The most frequent particle sizes of the diamonds obtained from the TR-, Si-, Ge-, and Sn-explosives in Figure 5.6e were approximately consistent with their average crystallite sizes calculated by the Scherrer formula. DNDs were thus synthesized from all explosives as in a typical detonation process, irrespective of the dopants. The DNDs originated from the TR-, Si-, Ge-, and Sn-explosives are hereinafter referred to as "undoped-, Si-, Ge-, and Sn-DNDs," respectively.

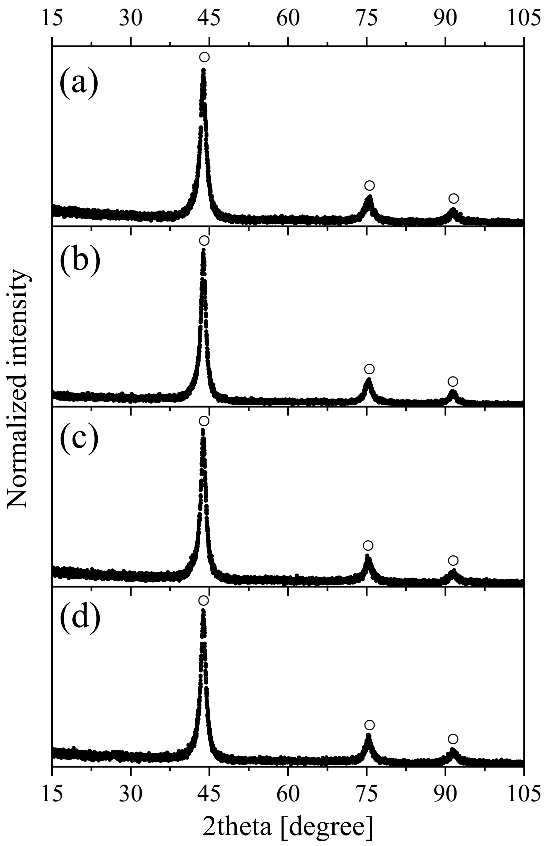

Figure 5.5 – XRD patterns of detonation products obtained from (a) TR-, (b) Si-, (c) Ge-, and (d) Sn-explosives. Circles denote cubic diamond structure.

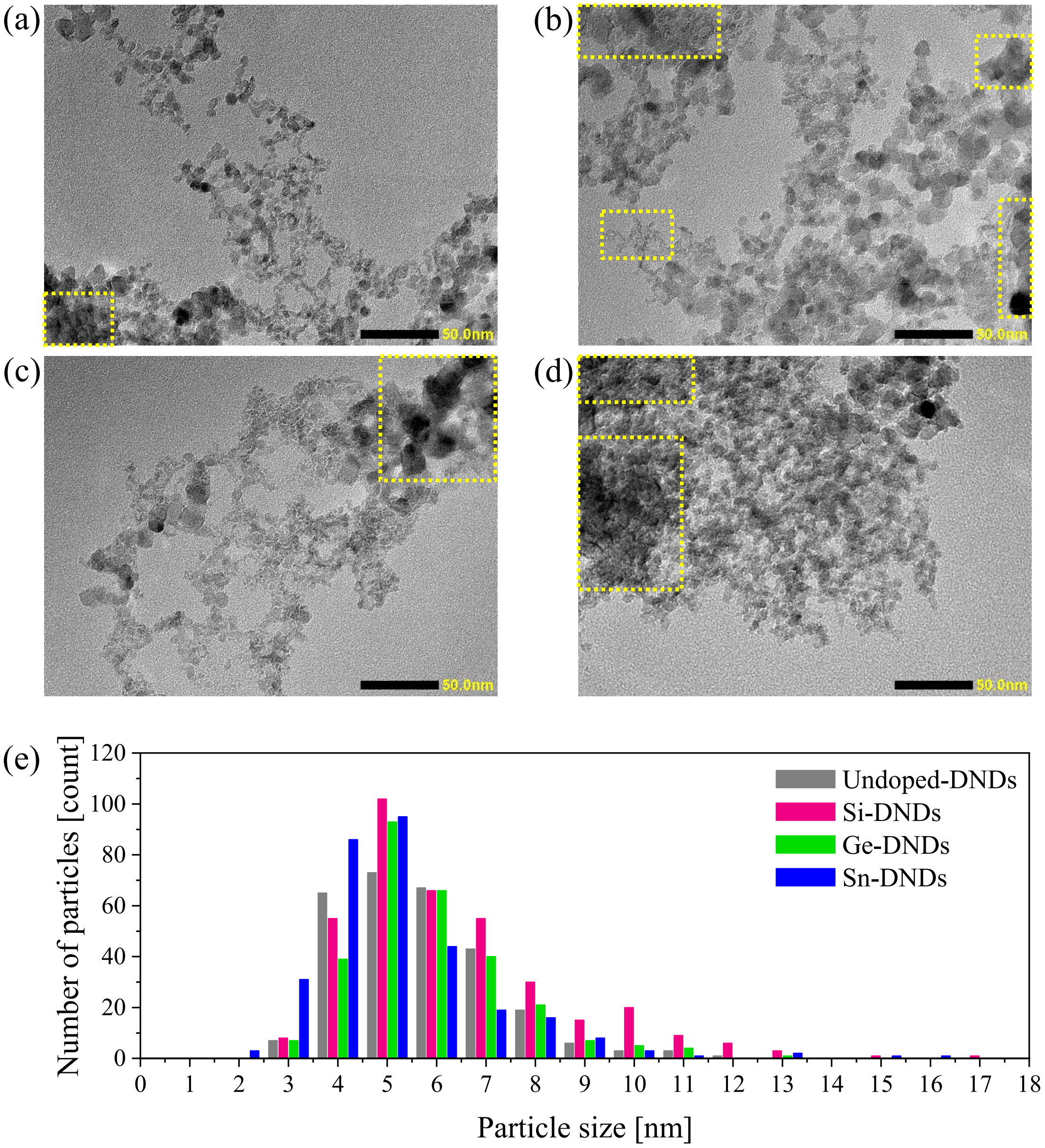

Figure 5.6 – TEM images of aggregated (a) undoped-, (b) Si-, (c) Ge-, and (d) Sn-DNDs. Yellow squares in (a)-(d) are areas of particle sizes that were excluded from calculations owing to unclear boundaries between adjacent particles. (e) Particle size distributions were obtained from TEM images.

Table 5.1 shows the elemental composition of the undoped-, Si-, Ge-, and Sn-DNDs provided by the XRF measurements. This elemental analysis is unsuitable for quantitatively characterizing elements with a low atomic number (e.g., carbon, nitrogen, and oxygen) [153]. In particular, nitrogen remains undetected despite being a major component of the DNDs as well as carbon and oxygen [89, 154, 155]. Nitrogen is mainly supplied by the explosives themselves. In addition, all samples were the detection of water oxygen adsorbed on the surface of the DNDs and a minimal amount of silicon, probably derived from the water used to recover the detonation products. Therefore, quantitative evaluation of the elements that compose the DNDs by the XRF measurements alone is difficult. On the other hand, the elemental concentrations of the four types of DNDs can be compared qualitatively because they were measured under the same conditions. The elemental concentrations of Si, Ge, and Sn in the Si-, Ge-, and Sn-DNDs are higher than those of the other DNDs analyzed, respectively. Thus, the corresponding dopants supplied the atoms of each group IV element to Si-, Ge-, and Sn-DNDs.

Table 5.1 – Elemental composition of each sample (mass%).

Element	Undoped-DNDs	Si-DNDs	Ge-DNDs	Sn-DNDs
C	92	92	92	91
O	7.5	7.9	8.1	8.4
Al	N.D.[a)]	0.0073	N.D.[a)]	0.021
Si	0.0077	0.086	0.049	0.047
P	N.D.[a)]	N.D.[a)]	0.0043	N.D.[a)]
S	0.022	0.021	0.017	0.016
Cl	0.073	0.039	0.024	0.034
K	N.D.[a)]	N.D.[a)]	0.0031	0.0047
Ca	N.D.[a)]	0.022	N.D.[a)]	0.013
Ti	N.D.[a)]	0.032	0.018	0.023
Fe	0.0069	0.016	0.011	0.011
Ni	N.D.[a)]	0.0017	0.0028	0.0024
Cu	0.0027	0.0065	0.0022	0.0071
Ge	N.D.[a)]	0.0034	0.021	0.0086
Sn	N.D.[a)]	N.D.[a)]	N.D.[a)]	0.0062

[a)] N.D.: Not detected

PL spectral measurements of the Si-, Ge-, and Sn-DNDs were performed at room temperature. The PL intensities at 1.68, 2.06, and 2.00 eV, which are the ZPLs of the SiV$^-$, GeV$^-$, and SnV$^-$ centers, are mapped in Figures 5.7a–c, respectively. Each map comprises 10201 data points, each corresponding to a 1 × 1 μm region. The DNDs were densely packed in this measurement area. Figures 5.7a'–c' show representative PL spectra for the Si-, Ge-, and Sn-DNDs (spots 1, 2, and 3 indicated in Figures 5.7a–c, respectively) as black dots. In addition, the PL spectra of the undoped-DND are shown as red dots in

Figures 5.7a'–c' to investigate the baseline of those PL spectra originating from the DND structure. The PL intensity of the undoped-DND was normalized with respect to the PL intensity of the Si-, Ge-, and Sn-DNDs at 1.75, 2.12, and 1.85 eV [52, 64], respectively. The subtracted spectra between each doped-DND and undoped-DND are shown as blue dots in Figures 5.7a'–c'. These subtracted spectra of the Si- and Ge-DNDs have distinct peaks at approximately 1.68 and 2.06 eV (Figures 5.7a' and b'). These peak positions agree with the well-known energies of the ZPLs for the SiV^- and GeV^- centers, which suggests that the SiV- and GeV-DNDs were successfully synthesized via the detonation process using the explosives containing TPS and TPG as Si and Ge sources, respectively. This experiment did not perform an annealing process to couple the group IV atoms (M) and vacancies (V) required in the general procedure for preparing the $G4V^-$ centers [83, 136, 147]. Although air-oxidation was performed at 470 °C as a post-treatment to remove trace amounts of sp^2 carbon, the temperature is not sufficient to combine M and V as reported by Shimazaki *et al.*; on their SiV-DND preparation using impurity Si in DND, the annealing temperature required to couple Si and V in the DND was 1100 °C, and 800 °C was insufficient [137]. Therefore, the SiV^- and GeV^- centers were generated during the DND formation process in the detonation reaction. In contrast, although the spectral shapes of the Sn-DNDs and undoped-DNDs are different, the ZPL of the SnV^- center is not found in the map in Figure 5.7c, as represented by Figure 5.7c'.

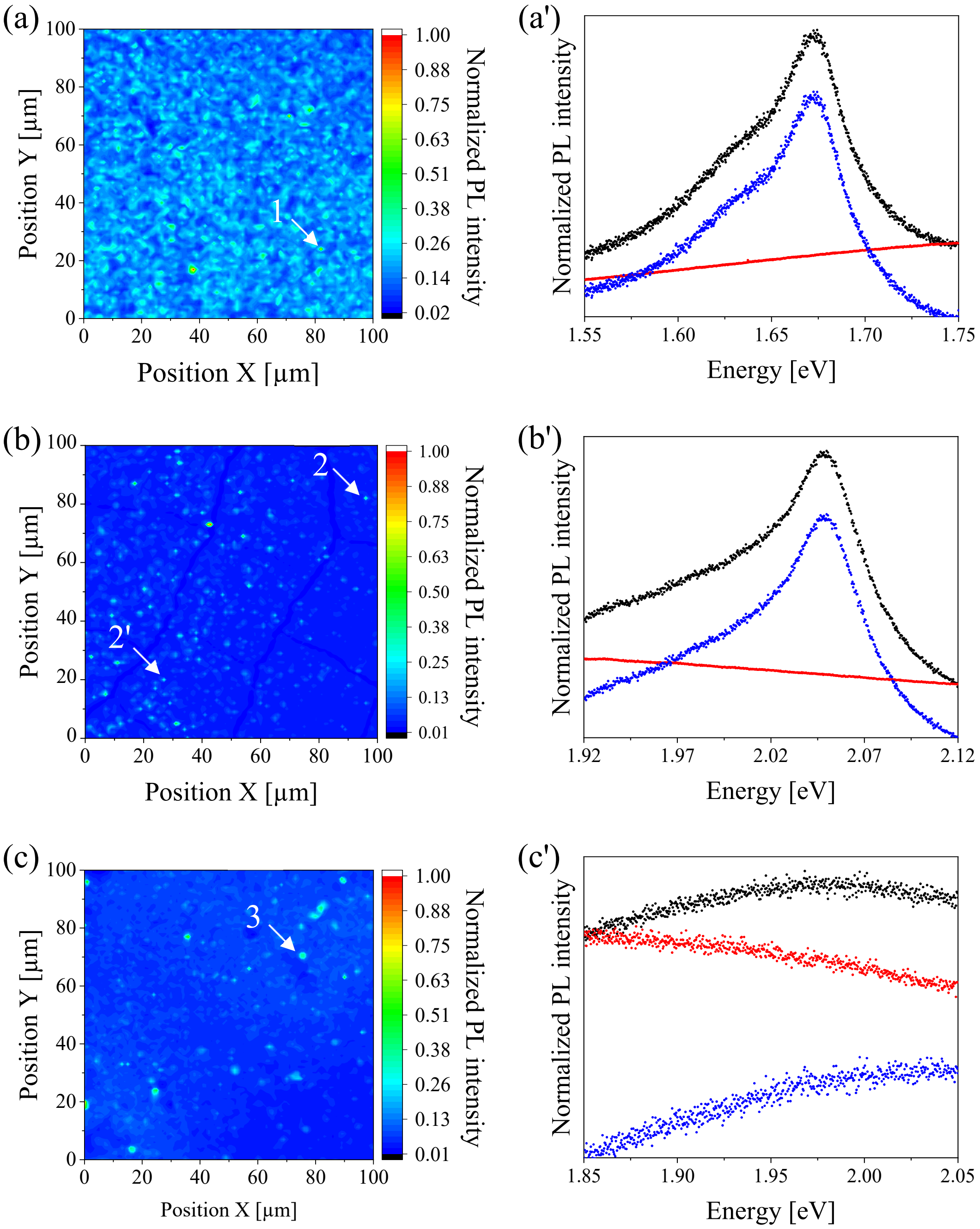

Figure 5.7 – Results of PL measurements for three types of doped-DNDs. PL intensity maps at (a) 1.68 eV for Si-DNDs, (b) 2.06 eV for Ge-DNDs, and (c) 2.00 eV for Sn-DNDs. PL spectra corresponding to spots 1, 2, and 3 indicated in (a–c) are shown by black dots in (a'–c'), respectively. Red dots show PL spectra of undoped-DNDs, of which intensities are normalized with respect to that of Si-, Ge-, and Sn-DNDs at 1.75, 2.12, and 1.85 eV, respectively. Subtracted spectra between each doped-DND (black dots) and undoped-DNDs (red dots) are shown by blue dots.

The numbers of data points in the maps in Figures 5.7a and b, where the spectra showing the ZPLs of the SiV^- and GeV^- centers such as spots 1 and 2 were observed, were counted to investigate the differences in the production amounts of the SiV- and GeV-DNDs. The counting of the data points including the SiV- or GeV-DNDs was performed regardless of the PL intensity to eliminate the effect of their unknown absorption cross-section. For the SiV- and GeV-DNDs (Figures 5.7a and b), 7050 and 1555 points were observed, respectively. Note that the map in Figure 5.7b shows not only the ideal spectrum of the GeV^- center, as in Figure 5.7b', but also a spectrum consisting of a peak at approximately 2.06 eV attributed to the ZPL of the GeV^- center and an unassigned peak at 1.97 eV, as shown in Figure 5.8. Although the peak at 1.97 eV can be a phonon sideband of the ZPL, there is also room for emission from other defects because of its excessively higher relative intensity to ZPL compared to previous reports [62, 83]. However, because the spectrum shown in Figure 5.8 contains the ZPL of the GeV^- center, the number of data points showing such spectra on the map was also counted as data points including the GeV-DNDs. The number of data points including the SiV-DNDs is larger than that of the GeV-DNDs; therefore, the production of SiV-DNDs was found to be more favorable. The unassigned peak at 1.97 eV is discussed in Chapter 6.

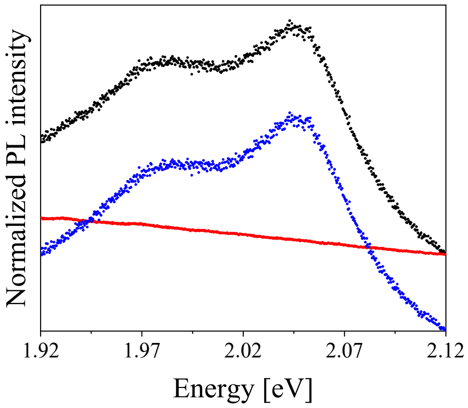

Figure 5.8 – Another type of PL spectrum of GeV-DNDs. PL spectra for GeV- and undoped-DNDs are plotted as black and red dots, respectively. PL intensity of undoped-DNDs is normalized with respect to PL intensity of GeV-DNDs at 2.12 eV. Subtracted spectrum of GeV- and undoped-DNDs are plotted as blue dots.

5.3.2 Quantum chemical calculation

The total electronic energies of the G4V-DNDs ($C_{104}[V\text{-}M\text{-}V]^{-}H_{86}$), group IV dopants ($C_{24}H_{20}M$), and group IV dioxides (MO_2) were evaluated at the optimized geometries, which are designated as $E_1(M)$, $E_2(M)$ and $E_3(M)$, respectively. Their calculated energies are listed in Table 5.2. In addition, vibrational analyses allowed for estimations of the corrections of thermal free energies for the model compounds of the G4V-DND, group IV dopants, and group IV dioxides at 3675 K, which are expressed as $G_1(M;T)$, $G_2(M;T)$ and $G_3(M;T)$, respectively. The resultant corrections are demonstrated in Table 5.3.

Table 5.2 – Total electronic energies of model compounds of G4V-DND ($C_{104}[V\text{-}M\text{-}V]^{-}H_{86}$), group IV dopants ($C_{24}H_{20}M$), and group IV dioxides (MO_2). Energy unit is in atomic units.

M	$E_1(M)$ ($C_{104}[V\text{-}M\text{-}V]^{-}H_{86}$)	$E_2(M)$ ($C_{24}H_{20}M$)	$E_3(M)$ (MO_2)
Si	−4301.53127150	−1215.38951832	−439.735831974
Ge	−6088.85498643	−3002.73791461	−2227.05597760
Sn	−4226.33190214	−1140.28420654	−364.591862294

Table 5.3 – Corrections of thermal free energies at 3675 K for G4V-DND ($C_{104}[V\text{-}M\text{-}V]^{-}H_{86}$), group IV dopants ($C_{24}H_{20}M$), and group IV dioxides (MO_2). Energy unit is in atomic units.

M	$G_1(M;T)$ ($C_{104}[V\text{-}M\text{-}V]^{-}H_{86}$)	$G_2(M;T)$ ($C_{24}H_{20}M$)	$G_3(M;T)$ (MO_2)
Si	−6.172200	−2.173138	−0.443483
Ge	−6.187622	−2.208038	−0.469007
Sn	−6.212044	−2.269380	−0.481704

5.4 Discussion

This section discusses the reasons for the differences in generated concentrations of each G4V-DND. HPHT synthesis of nano- and microdiamonds containing the $G4V^{-}$ centers using group IV dopants with the same chemical structure as the present study has been reported by Ekimov *et al.* [69]. Although the formation mechanism of the product is undoubtedly different between the HPHT method and the detonation process, the previously reported results are consistent with this present study in that the formation of the SiV^- and GeV^- centers was achieved, and only the SnV^- center was not produced. Ekimov *et al*. explained their results from reactivities with the group IV atoms and coexisting hydrogen atoms based on their employed HPHT system. On the other hand, the detonation reaction is dominated under thermodynamic control because the reaction proceeds under extreme conditions of approximately 25 GPa and 3675 K. The pressure and temperature correspond to the conditions at the CJ point (the details described in Chapter 1.4) of the 1.6 g cm^{-1} mixed explosive consisting of 60 wt% TNT and 40 wt% RDX used for the DNDs productions [116]. Therefore, the concentration ratios of the GeV- and SnV-DNDs to the SiV-DNDs were estimated from thermodynamic point of view and compared with the experimentally obtained data points of the $\mathrm{G4V}^-$ center luminescence in the PL-maps. To estimate the concentrations of the G4V-DNDs, it is first necessary to understand the mechanism of the DND formation. The dominant mechanism of the DND formation is that the self-decomposed explosive carbon species condense as droplet carbon (DC) and crystallize in the high-pressure and high-temperature environment of the detonation, on the basis of a nanoscale carbon phase diagram (the details described in Section 1.4) [90, 91]. In the case of the G4V-DND synthesis, group IV dopants ($\mathrm{MPh_4}$, M: Si, Ge, and Sn, Ph: phenyl group) are involved in the mechanism. Hereinafter, the G4V-DND are expressed as the MV-DND to distinguish $\mathrm{G4V}^-$ centers with different M. Focusing on the $\mathrm{MPh_4}$, two reactions proceed simultaneously. In the reaction of Equation 5.1, the $\mathrm{MPh_4}$ is incorporated into the DC to form the M-DC, the precursor of the MV-DND. In the reaction of Equation 5.2, the oxidation of the $\mathrm{MPh_4}$ proceeds. The oxygen atoms of the explosives involved in these reactions can be regarded as substantially $\mathrm{O_2}$.

$$\mathrm{MPh_4 + DC + 5O_2 \xrightleftharpoons{\Delta G_{1\mathrm{M}}} M\text{-}DC + 10H_2O}, \tag{5.1}$$

$$\mathrm{MPh_4 + 30O_2 \xrightleftharpoons{\Delta G_{2\mathrm{M}}} MO_2 + 10H_2O + 24CO_2}. \tag{5.2}$$

Although the reaction in Equation 5.1 includes the process of the DC agglomeration growth, I assumed an average DC size for a simple representation of the reaction. The length of the arrows indicates that the forward reaction is dominant in the equilibrium reaction since each oxide is thermodynamically stable in Equation 5.2. $\Delta G_{1\mathrm{M}}$ and $\Delta G_{2\mathrm{M}}$ are the free energy changes for Equations 5.1 and 5.2, respectively, which are dependent on M. The MV-DND generation by crystallization of the M-DC proceeds irreversibly in the latter stages of the detonation reaction. There is a sufficiently long time for this crystallization to begin; therefore, the two reactions can be considered to arrive at the chemical equilibrium state. The final concentration of the MV-DND is expected to be proportional to the concentration of the M-DC. Therefore, the concentration ratio of the M-DC (Ge- or Sn-DC) to Si-DC, $[\mathrm{M\text{-}DC}]/[\mathrm{Si\text{-}DC}]$, is calculated in this discussion. Here, the conversion of the $\mathrm{MPh_4}$ in Equations 5.1 and 5.2 under the extreme conditions of detonation is considered to be approximately 100%; therefore, the M-DC yield can be equated with the selectivity of their reactions, N_M. In addition, because the $\mathrm{MO_2}$ is the most stable compound containing M, it should be produced far more than the M-DC. Therefore, N_M can be approximated by Equation 5.3,

$$N_{\mathrm{M}} = \frac{[\text{M-DC}]}{[\text{M-DC}] + [\mathrm{MO_2}]} \approx \frac{[\text{M-DC}]}{[\mathrm{MO_2}]}. \tag{5.3}$$

The respective thermodynamic equilibrium constants $K_{1\mathrm{M}}$ and $K_{2\mathrm{M}}$ on Equations 5.1 and 5.2 are obtained by applying the law of mass action to these equations as follows:

$$K_{1\mathrm{M}} = K_{\gamma 1\mathrm{M}} \frac{[\text{M-DC}][\mathrm{H_2O}]^{10}}{[\mathrm{MP_4}][\mathrm{DC}][\mathrm{O_2}]^5} = \exp\left(\frac{-\Delta G_{1\mathrm{M}}}{RT}\right), \tag{5.4}$$

$$K_{2\mathrm{M}} = K_{\gamma 2\mathrm{M}} \frac{[\mathrm{MO_2}][\mathrm{H_2O}]^{10}[\mathrm{CO_2}]^{24}}{[\mathrm{MP_4}][\mathrm{O_2}]^{30}} = \exp\left(\frac{-\Delta G_{2\mathrm{M}}}{RT}\right), \tag{5.5}$$

where $K_{\gamma 1\mathrm{M}}$ and $K_{\gamma 2\mathrm{M}}$ are constants determined by the activity coefficient of each species, and R and T are gas constant (8.31×10^{-3} kJ mol^{-1} K^{-1}) and the absolute temperature of the detonation reaction, respectively. Hence, N_{M} is expressed as Equation 5.6:

$$N_{\mathrm{M}} = \frac{K_{1\mathrm{M}}}{K_{2\mathrm{M}}} \frac{K_{\gamma 2\mathrm{M}}}{K_{\gamma 1\mathrm{M}}} \frac{[\mathrm{DC}][\mathrm{CO_2}]^{24}}{[\mathrm{O_2}]^{25}}. \tag{5.6}$$

Because the amount of the $\mathrm{MPh_4}$ added to the explosive is so small as 1 wt%, the changes in the amounts of the DC, $\mathrm{CO_2}$, and $\mathrm{O_2}$ involved in the reactions of Equations 5.1 and 5.2 are negligible in the overall detonation reaction. Therefore, the factor $[\mathrm{DC}][\mathrm{CO_2}]^{24}/[\mathrm{O_2}]^{25}$ in Equation 5.6 can be regarded as a constant, and the concentration ratio of the MV-DND (Ge- or Sn-DND) to the SiV-DND can be derived as follows:

$$\frac{[\text{M-DC}]}{[\text{Si-DC}]} = \frac{N_{\mathrm{M}}}{N_{\mathrm{Si}}} \approx \frac{K_{1\mathrm{M}}}{K_{2\mathrm{M}}} \frac{K_{2\mathrm{Si}}}{K_{1\mathrm{Si}}} \frac{K_{\gamma 2\mathrm{M}}}{K_{\gamma 1\mathrm{M}}} \frac{K_{\gamma 1\mathrm{Si}}}{K_{\gamma 2\mathrm{Si}}} \approx \exp\left\{\frac{-\left(\Delta\Delta G_{1\mathrm{M/Si}} - \Delta\Delta G_{2\mathrm{M/Si}}\right)}{RT}\right\}. \tag{5.7}$$

The homologous elements exhibit similar chemical behavior; therefore, deviations from the ideal behavior of the M-DC and the MO_2 are also considered to be identical to the Si-DC and the SiO_2, respectively. Thus, $\left(K_{\gamma 1\mathrm{Si}}/K_{\gamma 1\mathrm{M}}\right)$ and $\left(K_{\gamma 2\mathrm{M}}/K_{\gamma 2\mathrm{Si}}\right)$ in the derivation of Equation 5.7 can be approximated as 1. $\Delta\Delta G_{1\mathrm{M/Si}}$ and $\Delta\Delta G_{2\mathrm{M/Si}}$ correspond to the relative free energies calculated by $\Delta G_{1\mathrm{M}} - \Delta G_{1\mathrm{Si}}$ and $\Delta G_{2\mathrm{M}} - \Delta G_{2\mathrm{Si}}$, respectively. Thus, these reactions with relative free energy changes can be summarized from Equations 5.1 and 5.2 as Equations 5.8 and 5.9, respectively.

$$\mathrm{MPh_4} + \text{Si-DC} \xrightleftharpoons{\Delta\Delta G_{1\mathrm{M/Si}}} \mathrm{SiPh_4} + \text{M-DC}\ , \tag{5.8}$$

$$\mathrm{MPh_4} + \mathrm{SiO_2} \xrightleftharpoons{\Delta\Delta G_{2\mathrm{M/Si}}} \mathrm{SiPh_4} + \mathrm{MO_2}\ . \tag{5.9}$$

The relative free energies $\Delta\Delta G_{1\mathrm{M/Si}}$ and $\Delta\Delta G_{2\mathrm{M/Si}}$ are subtractions of the total electronic energies with the corrections of the thermal free energies of the reactant species from those of the product species in Equations 5.8 and 5.9, respectively. However, it is difficult to calculate the total electronic energies of the Si- and M-DC (Ge- or Sn-DC). Here, the free energy change is zero along the coexistence line in the phase diagram; hence, the free energy changes from the Si- and M-DC to the SiV- and MV-DND (GeV- or SnV-DND) in the neighborhood of the coexistence line can both be regarded as approximately zero. Therefore, the values of $\Delta\Delta G_{1\mathrm{M/Si}}$ are not affected when the Si- and M-DC are substituted by the SiV- and MV-DND, respectively. Thus, $\Delta\Delta G_{1\mathrm{M/Si}}$ was calculated using the total electron energy of the Si- and MV-DND instead of the Si- and M-DC. According to thermodynamics, the relative free energies for the generation of the MV-DND and the MO_2

(Equations 5.8 and 5.9, respectively) at temperature T, $\Delta\Delta G_{1\mathrm{M/Si}}$ and $\Delta\Delta G_{2\mathrm{M/Si}}$, can be calculated by Equations 5.10 and 5.11, respectively, using the values of $\mathrm{E}_i(\mathrm{M})$ and $\mathrm{G}_i(\mathrm{M};T)$ in Tables 5.2 and 5.3:

$$\Delta\Delta G_{1\mathrm{M/Si}} = \textstyle\sum_{i=1}^{2} \nu_i\{-\mathrm{E_i}(\mathrm{M}) - \mathrm{G}_i(\mathrm{M};T) + \mathrm{E}_i(\mathrm{Si}) + \mathrm{G}_i(\mathrm{Si};T)\}\,, \tag{5.10}$$

$$\Delta\Delta G_{2\mathrm{M/Si}} = \textstyle\sum_{i=1}^{2} \nu_i\{\mathrm{E}_{i+1}(\mathrm{M}) + \mathrm{G}_{i+1}(\mathrm{M};T) - \mathrm{E}_{i+1}(\mathrm{Si}) - \mathrm{G}_{i+1}(\mathrm{Si};T)\}\,, \tag{5.11}$$

where ν_i denotes a stoichiometric coefficient. ν_1 and ν_2 are equal to -1 and $+1$, respectively. Table 5.4 summarizes the values of $\Delta\Delta G_{1\mathrm{M/Si}}$ and $\Delta\Delta G_{2\mathrm{M/Si}}$ calculated by the quantum chemical method and vibrational analysis, and the equilibrium concentration ratios of the GeV- and SnV-DNDs to the SiV-DNDs estimated by Equation 5.7. T used in the correction of the thermal free energies and calculation of Equation 5.7 was taken to be 3675 K for the detonation temperatures of the TR-explosive at 1.6 g cm^{-3} [116]. According to this thermodynamic estimation, the concentration of the SnV-DND compared with that of the SiV-DND is almost zero, which is consistent with the experimental results that the SnV-DNDs were undetected in the PL-map. The thermodynamically calculated ratio of the GeV-DND production concentration to the SiV-DNDs is approximately 0.6, similar to the order of the ratio of experimentally detected data points in the PL maps of 0.22. Hence, the thermodynamics of the detonation reactions could explain the experimental results. The SiV-DND was produced at higher concentrations than the GeV- and SnV-DND owing to the thermodynamic advantage of the reaction.

Table 5.4 – Calculation results for relative free energies of Equations 5.8, 5.9, and equilibrium concentration ratios of GeV- and SnV-DNDs to SiV-DNDs. Thermal free energies were corrected under 3675 K.

M	$\Delta\Delta G_{1\mathrm{M/Si}}$ [kJ mol^{-1}]	$\Delta\Delta G_{2\mathrm{M/Si}}$ [kJ mol^{-1}]	[MV-DND]/[SiV-DND]	
			Calculation	Experiment[a)]
Ge	116	99	0.57	0.22
Sn	395	254	0.01	0.00[b)]

[a)] Ratio of the number of data points where spectra containing the ZPL of each G4V⁻ center were detected in PL-maps; [b)] SnV-DNDs were not detected in PL measurements.

The generation ratio of the G4V-DNDs was well explained by thermodynamics of the detonation reaction. However, the concentration ratio of the GeV-DNDs to the SiV-DNDs evaluated experimentally is slightly smaller than the calculated value. This difference may be due to the slight effect of kinetics. The detonation processes were identical except for the dopants used as the group IV atom sources. Therefore, this discussion focuses on the differences in the chemical structures of the dopants with tetraphenyl structures. In the study in Chapter 4 regarding the SiV-DNDs synthesis, it was proposed that the interaction between the aromatic ring structure of the Si-dopant and that of TNT has an essential role in the doping of Si. According to this proposal, it is necessary for group IV atom doping that the M−C bond between M and the aromatic ring be maintained in the detonation reaction; the bond energies of the Si–C, Ge–C, and Sn–C were 272, 264, and 216 kJ mol^{-1}, respectively [156]. The kinetic rate of cleavage of these bonds k_{M} can be expressed using Arrhenius equation:

$$k_{\mathrm{M}} = A_{\mathrm{M}} \exp\left(\frac{-E_{\mathrm{a}}^{\mathrm{M}}}{RT}\right), \tag{5.12}$$

where A_{M} and $E_{\mathrm{a}}^{\mathrm{M}}$ are the frequency factor and the activation energy of the cleavage of each M−C bond (M: Si, Ge, and Sn), respectively. R and T are the gas constant (8.31×10^{-3} kJ mol^{-1} K^{-1}) and the detonation temperature 3675 K, respectively, which are the same as the discussion based on thermodynamics. If k_{Si} is adopted as a reference for the kinetic rate, then relative kinetic rates of k_{Ge} and k_{Sn} can be expressed as follows:

$$k_{\mathrm{Si}}^{\mathrm{M}} = \frac{k_{\mathrm{M}}}{k_{\mathrm{Si}}} = \frac{A_{\mathrm{M}}}{A_{\mathrm{Si}}} \exp\left\{\frac{-\left(E_{\mathrm{a}}^{\mathrm{M}} - E_{\mathrm{a}}^{\mathrm{Si}}\right)}{RT}\right\}, \tag{5.13}$$

where $k_{\mathrm{Si}}^{\mathrm{M}}$ is the relative kinetic rate, and M is eligible for only Ge and Sn. Here, A_{M} can be supposed to be a similar value to A_{Si} owing to the chemical analogues of M (Ge or Sn) to Si. In addition, if the difference in the activation energy between $E_{\mathrm{a}}^{\mathrm{M}}$ and $E_{\mathrm{a}}^{\mathrm{Si}}$ can be regarded as that in bond energy ΔE_{B}, Equation 5.13 can be approximated as follows:

$$k_{\mathrm{Si}}^{\mathrm{M}} \approx \exp\left(\frac{-\Delta E_{\mathrm{B}}}{RT}\right). \tag{5.14}$$

The results of the calculations are shown in Table 5.5. The dopants used as the Ge (Ge-dopant, TPG) and Sn (Sn-dopant, TPT) sources lose the aromatic ring structure, which plays an essential role in doping the group IV atoms into the carbon clusters during the detonation reactions, i.e., more rapidly than the Si source dopant (Si-dopant, TPS). Therefore, the generation of the SiV-DNDs is more advantageous than that of the GeV- and SnV-DNDs from a kinetic point of view. The experimentally determined concentration ratio of the GeV-DND to the SiV-DND was probably lower than one thermodynamically estimated owing to the kinetic effect of each dopant. However, the kinetic effect is limited compared to the thermodynamic effect because the detonation reaction proceeds in extreme conditions.

Table 5.5 – Relative kinetic rates of Ge- and Sn-dopants calculated with respect to Si-dopant at 3675 K.

M	$k_{\mathrm{Si}}^{\mathrm{M}}$
Ge	1.30
Sn	6.27

5.5 Summary

The synthesis of the G4V-DNDs was performed by the detonation process using the dopant molecules with group IV atoms centered on tetraphenyl compounds. The direct synthesis of the SiV- and GeV-DNDs was confirmed by the observation of the ZPLs in their PL spectra. However, the SnV-DNDs were not produced in detectable concentrations in PL measurements. According to the PL-maps, the SiV- and GeV-DNDs were observed in 7055 and 1555 data points, respectively, among a total of 10201 data points. Therefore, this synthesis process favorably produced the G4V-DNDs composed of elements with smaller atomic numbers. According to the amount of the produced G4V-DNDs, the contribution of thermodynamics to the reaction was more dominant over than that of kinetics, dependent on the molecular structure of the dopant in this reaction. The successes and limitations of the G4V-DND direct synthesis by the detonation process can be explained by the influence of each group IV atom on the chemical equilibrium in the process.

Chapter 6. Optical properties of silicon- or germanium-vacancy centers-containing nanodiamonds fabricated by detonation process

6.1 Introduction

In the previous Chapters 4 and 5, the mass productions of the SiV- and GeV-NDs were demonstrated via the detonation process using the aromatic compounds as the group IV dopants. An understanding of their optical properties is indispensable for their applications. The optical properties of the SiV^- and GeV^- centers have been widely studied using bulk-sized diamonds containing them, as described in Chapter 1.2. Representative optical properties of the SiV^- and the GeV^- centers are exhibited in their ZPLs located at 1.68 and 2.06 eV [65], respectively. The ZPLs of SiV^- and GeV^- centers appear in their PL spectra as narrow peaks with linewidths of ~11.4 and ~17.1 meV [52], respectively. Moreover, their luminescence is concentrated in the ZPLs, whose DWFs are over 0.6 [64]. These optical properties are derived from their split-vacancy structure with D_{3d} symmetry isolated from the carbon bonding network which strongly suppresses their electron–phonon couplings (the split-vacancy structure illustrated in Figure 1.4) [56, 60]. As additional features of their luminescence, the PL spectra of the SiV^- and GeV^- centers have also been reported to show peaks attributed to local vibrational modes (LVMs) of the diamond lattice at low energies of ~64 and ~45 meV from their ZPLs, respectively [157]. For the SiV^- center, its radiative decay time was calculated as 6.24 ns by experimental results [158]. These reported values have generally been accepted as the optical properties exhibited by ideal SiV^- and GeV^- centers. However, the optical properties of the SiV^- and GeV^- centers in NDs and an understanding of their particle size effect have not been studied well. In this chapter, the optical properties of the SiV^- and GeV^- centers inside extremely small NDs synthesized by the detonation process (the SiV^- and the GeV^- centers in DNDs, respectively) were systematically investigated by spectroscopy. Moreover, the particle size effect on the color centers was discussed by comparing the optical properties of the SiV^- and GeV^- centers in DNDs and ideal ones in bulk-sized diamonds.

6.2 Experimental detail in Chapter 6

6.2.1 Synthesis and structural characterization

1000 g of a mixed explosive consisting of 60 wt% TNT and 40 wt% RDX (TR-explosive) was used to fabricate the undoped-DNDs. This chapter used large amounts of explosives compared with Chapters 3–5 (60 g as the TR-explosive) to obtain a large volume of DND samples. Explosives for SiV- and GeV-DNDs productions were prepared by adding 10 g of TPSOH (Tokyo Chemical Industry Co., Ltd.) and TPG (Tokyo Chemical Industry Co., Ltd.) as dopants in TR-explosive, respectively (Si- and Ge-explosives, respectively). Their chemical structures and properties are described in Chapters 3.3.5 and 5.2.1. They could be well mixed with TNT and RDX powders. The resultant mixtures could be molded by pressing them into a cylindrical shape. The bulk densities of the TR-, Si-, and Ge-explosives were 1.59, 1.54, and 1.55 g cm^{-3}, respectively. Each of the three explosives was detonated under a CO_2 atmosphere. The detonation products were purified by the acid-, alkali treatments and air-oxidization at 470 or 570 °C for 2 h. These purified samples were confirmed to be DNDs by powder XRD analyses and TEM observations. These details are described in Chapter 2.1.

6.2.2 Investigation of optical properties

The air-oxidized DNDs for optical measurements were prepared by dropping 100 μL of 10 wt% aqueous suspensions of each DND onto glass substrates and drying them (drop-cast samples). PL measurements of the undoped-, SiV-, and GeV-DNDs were performed using the handmade system schematically shown in Figure 6.1. A Yb: KGW laser (Pharos, Light Conversion) operating at 1 kHz with a 200 fs pulse width and 0.2 mJ pulse energy at an output energy of 1.204 eV was used to pump an optical parametric amplifier (OPA; Orpheus-HP, Light Conversion) and to generate excitation pulses with energy in the range of 1.80–3.54 eV. The excitation laser beam was guided through a circular pinhole for all-optical experiments. Luminescence was spectrally dispersed by a spectrometer (SpectraPro HRS-300, Acton Research) equipped with a 150 grooves mm^{-1} grating and was detected using an air-cooled CCD camera (PIXIS 256, Princeton Instruments). In the case of low-temperature measurements, the drop-cast samples were cooled using a He cryostat and excited by the laser with an energy of 2.34 eV.

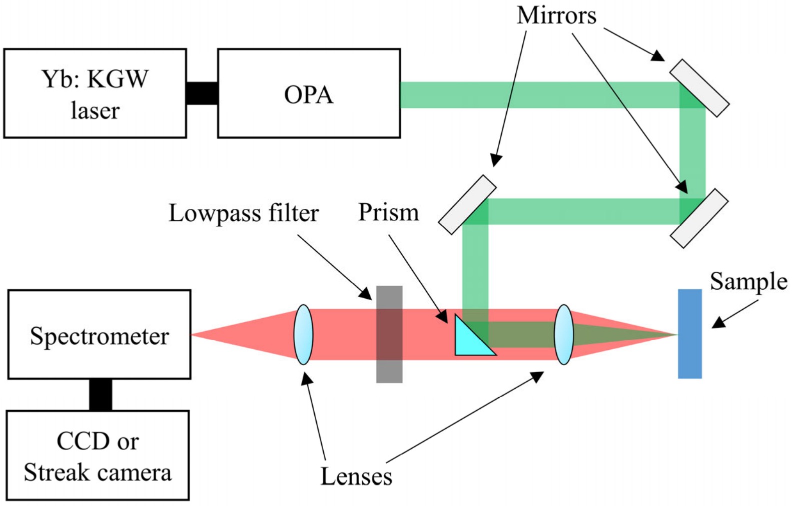

Figure 6.1 – Schematic of optical system for PL experiments.

For time-resolved PL measurements of the SiV- and GeV-DNDs, the same optical system shown in Figure 6.1 was employed. The SiV- and GeV-DNDs samples were excited by an excitation laser with an energy of 2.34 and 2.38 eV, respectively. Luminescence was detected by a streak camera (C14831, Hamamatsu Photonics) interfaced with a spectrometer (SpectraPro 300i, Acton Research) equipped with a 50 grooves mm^{-1} grating. This optical system recorded time-resolved spectra on timescales of 1000, 100, and 20 ns with time resolutions of 1.4, 0.14, and 0.027 ns, respectively.

The photostability of the SiV^{-} or GeV^{-} centers in DNDs was evaluated according to the method of Reineck *et al.*, as follows [159]. Colloidal solutions of the SiV- or GeV-DNDs were prepared by sonicating 750 mg of each DNDs in 15 mL of DI water using an ultrasound horn (UP-400S, Hielscher Ultrasonics) at 180 W for 3 h to ensure proper dispersion. The dispersions were centrifuged (CR22G, Hitachi Koki) at 13200 × *g* for 1 h. The supernatant was separated, and DI water was added to the separated supernatant to prepare the SiV- or GeV-DNDs at a concentration of 1 wt%. The concentrations were confirmed by measuring the weights of the SiV- or GeV-DNDs remaining after the prepared dispersions were dried. The 1 wt% water dispersions of the SiV- or GeV-DNDs were filled into a glass capillary with an inner diameter of 10 µm and an outer diameter of 1 mm. The PL intensities of the colloidal samples were measured over time using the system shown in Figure 6.1, which was equipped with a CW laser with an excitation energy of 2.33 eV (LCX-532S, Oxxius). The samples were irradiated with the CW laser at 7.1 kW cm^{-2}, and the PL measurements were performed every 15 s.

6.3 Results and discussion

6.3.1 Structural characterization

XRD patterns of the SiV- and GeV-DNDs are shown in Figure 6.2, which have three major diffraction peaks originating from the (111), (220), and (311) planes of the diamond. The average crystallite sizes, approximately the average particle sizes of the DNDs, were calculated using Scherrer's formula on the basis of (111) diffraction peaks showing the strongest diffraction intensities. The average sizes of the SiV-DNDs air-oxidized at 470 and 570 °C were 8.1 and 10.8 nm, respectively. The average sizes of the GeV-DNDs purified by the air-oxidation at 470 and 570 °C were 7.4 and 9.1 nm, respectively. Their particle size distributions were obtained by the TEM observations. Figures 6.3a–d show TEM images of the SiV- and GeV-DNDs air-oxidized at different temperatures. The SiV-DNDs air-oxidized at 570 °C do not have a well-defined sphere shape like the other DNDs. The sizes of particles in the TEM images were calculated by assuming a spherical shape because the particle sizes of such non-spherical particles were difficult to determine. In addition, the calculation did not include particles with unclear boundaries of adjacent particles in yellow squares indicated in the TEM images. Figure 6.3e shows the particle size distributions calculated from the TEM images. The most frequent particle sizes of all samples in Figure 6.3e are consistent with the average values calculated from the XRD patterns. However, the particle size distributions of the SiV- and GeV-DNDs air-oxidized at 470 °C are broader and contain larger particles than those fabricated in Chapters 4 and 5. These size changes were explained by a well-known positive correlation of the explosive weight with the particle size [105]. In this chapter, the explosive weights were increased from 60 g in the previous chapters to 1000 g in order to scale up the SiV- and GeV-DNDs production. The exothermic chemical reaction zone in which the explosive molecules decompose (the details described in Chapter 1.4) increased with the explosive size, allowing the carbon condensation and crystallization processes to continue on a longer time scale for larger explosives. Hence, larger particles of the SiV- and GeV-DNDs air-oxidized at 470 °C were produced in this chapter. The changes in the particle size depending on the air-oxidation temperatures are discussed in the next paragraph.

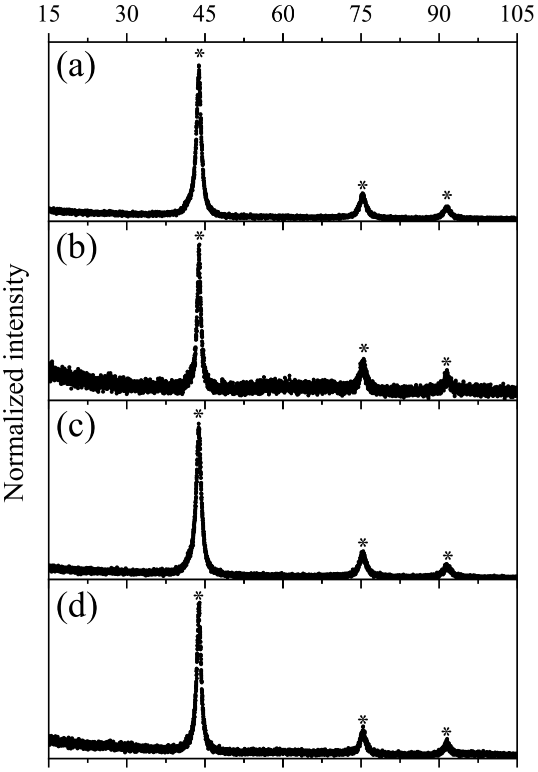

Figure 6.2 – XRD patterns of (a, b) SiV- and (c, d) GeV-DNDs. These air-oxidization temperatures were (a, c) 470 and (b, d) 570 °C. Asterisks denote a cubic diamond structure.

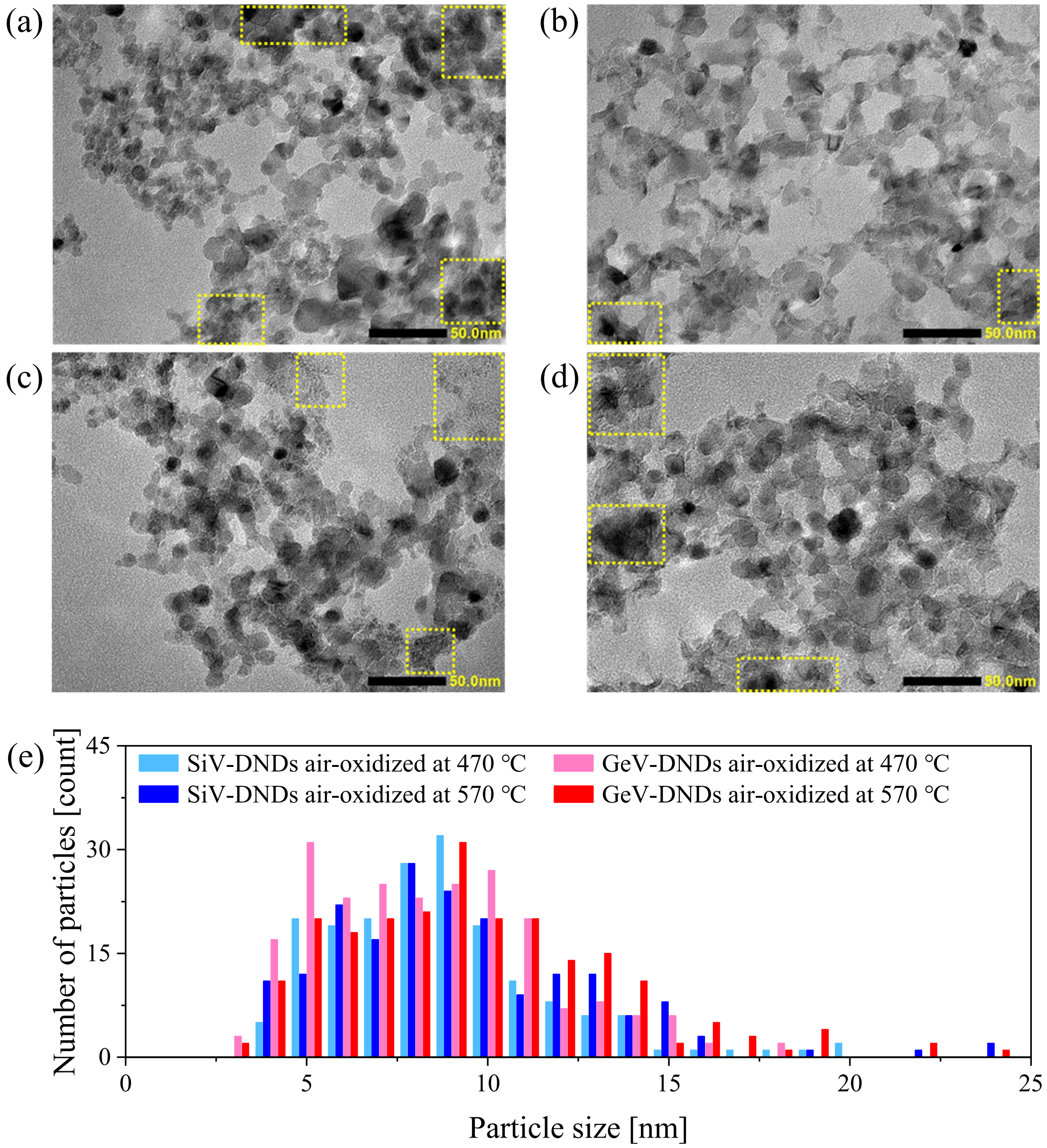

Figure 6.3 – TEM images of aggregated (a, b) SiV- and (c, d) GeV-DNDs. These air-oxidization temperatures were (a, c) 470 and (b, d) 570 ºC. Yellow squares in (a)–(d) are excluded areas in the particle size calculations owing to unclear boundaries between adjacent particles. (e) Particle size distributions obtained from TEM images.

The results of the XRD analyses and the TEM observations indicate that the particle sizes of the DNDs depend on the air-oxidation temperature. The air-oxidation conditions, yields, and particle sizes are shown in Table 6.1. The DNDs oxidized at 470 °C hardly lost their weight, whereas those oxidized at 570 °C lost approximately 95 wt%. The high-temperature condition caused an increase in particle size and a decrease in yield. Osswald *et al*. reported similar results and pointed out that larger particles observed after the oxidation treatment were present in the sample before the treatment [160]. My experimental results summarized in Table 6.1 can be similarly explained by the discussion of Osswald *et al*. Only relatively large particles survived the air-oxidation process at 570 °C, while particularly small DNDs, such as those with a single-digit-nanometer diameter, were decomposed and/or combusted.

Table 6.1 – Yield and primary particle size of SiV- and GeV-DNDs after air-oxidation.

Sample	Air-oxidization conditions		Yield [wt%]	Average particle size[a] [nm]
	Temperature [°C]	Time [h]		
SiV-DNDs	470	2	86.3	8.1
	570	2	4.6	10.8
GeV-DNDs	470	2	89.4	7.4
	570	2	5.8	9.1

[a] Calculated by Scherrer's formula using the (111) diffraction peaks.

The PL measurements were performed using the optical system shown in Figure 6.1 to investigate the influence of the air-oxidation temperatures on luminescence from the SiV- and GeV-DNDs. PL spectra of the SiV- and GeV-DNDs air-oxidized at 470 and 570 °C were recorded at room temperature using the laser with an excitation energy of 2.34 eV, as shown in Figure 6.4. The luminescence from the SiV- and GeV-DNDs are composed not only of the ZPLs at 1.68 or 2.06 eV with PSB originating from the SiV^- and GeV^- centers but also of luminescence bands with a broad peak around 1.80 eV as baselines. Similar broad backgrounds have been observed in the spectra of SiV^- or GeV^- centers-containing bulk-sized diamonds/NDs fabricated by other methods [65, 80, 161–163]. In the case of NDs with a size of 5–50 nm, such broadband luminescence presumably originates from surface defects [164]. Therefore, the broad backgrounds observed from the SiV- and GeV-DNDs originate in the diamond structures irrespective of those color centers. Moreover, the ZPL intensities of the SiV^- and GeV^- centers increased in the high-temperature-treated samples. The increase in the ZPL intensity of the GeV-DNDs is particularly remarkable; the luminescence from the surface defects mentioned above is almost invisible in the PL spectrum of the GeV-DNDs air-oxidized at 570 °C. This increase in the ZPL intensities might be attributable to the average particle size and yield after the air-oxidization (see Table 6.1). According to Shershulin *et al.* [165], the smallest oxygen-terminated diamond particle that can hold a stable SiV^- center is 8 nm. After the air-oxidation at 570 °C, DNDs smaller than 8 nm were decomposed/combusted, and only the initially large particles (4.6 wt% of the total mass) capable of emitting SiV^- luminescence survived. The same process can be considered to occur for the GeV^- center as well as the SiV^- center. As a result, concentrations of the SiV^- or GeV^- centers in DNDs are increased.

In addition, the high-temperature air-oxidation might have eliminated defects quenching the PL from color centers [67, 160]. Since the luminescence intensities of the samples oxidized at 570 °C are stronger than the ones oxidized at 470 °C, the SiV- and GeV-DNDs oxidized at 570 °C were employed for subsequent optical measurements in Sections 3.2 and 3.3, respectively.

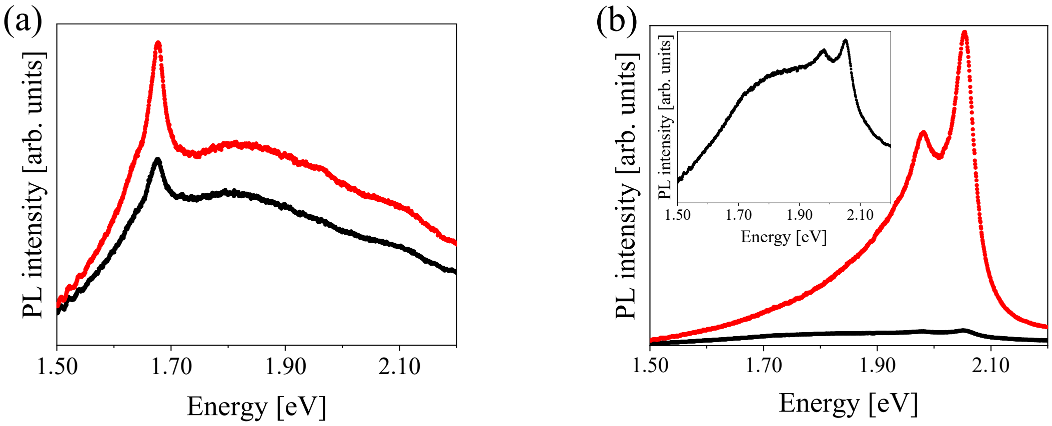

Figure 6.4 – PL spectra of (a) SiV- and (b) GeV-DNDs excited by 2.34 eV. Black and red dots indicate the spectra of air-oxidized samples at 470 and 570 ºC, respectively. Inset of (b) is a magnified view of PL spectrum of GeV-DNDs air-oxidized at 470 ºC.

6.3.2 Optical properties of silicon-vacancy centers in detonation nanodiamonds

6.3.2.1 Photoluminescence spectra

The PL spectrum of the SiV-DNDs excited at room temperature by the laser with an excitation energy of 2.34 eV is shown in Figure 6.5a as black dots. Red dots in Figure 6.5a additionally show the PL spectrum of the undoped-DNDs air-oxidized at 570 °C measured to examine the broadband background luminescence from the diamond structure in the PL spectrum of the SiV-DNDs air-oxidized at 570 °C, where PL intensity is normalized by the PL intensity of the SiV-DNDs at 1.80 eV. The subtracted spectrum between the SiV- and undoped-DNDs indicated as blue dots in Figure 6.5a show typical SiV^{-} luminescence spectra shapes. Figure 6.5b shows that the ZPL of SiV⁻ center in the subtracted spectrum can be well-fitted with a Gaussian curve. The ZPL linewidth (FWHM: full-width at half-maximum) of the SiV-DNDs is 32 meV. Its DWF is calculated to be 0.47 as the area ratio of the subtracted spectrum to the Gaussian curve. In the case of typical SiV⁻ centers in bulk-sized diamonds reported by Häußler *et al.* [65], ZPL linewidth and DWF were 12.1 meV and 0.67, respectively; therefore, the SiV⁻ centers in DNDs exhibit ZPLs with wider homogeneous and/or inhomogeneous broadening and have stronger electron–phonon couplings.

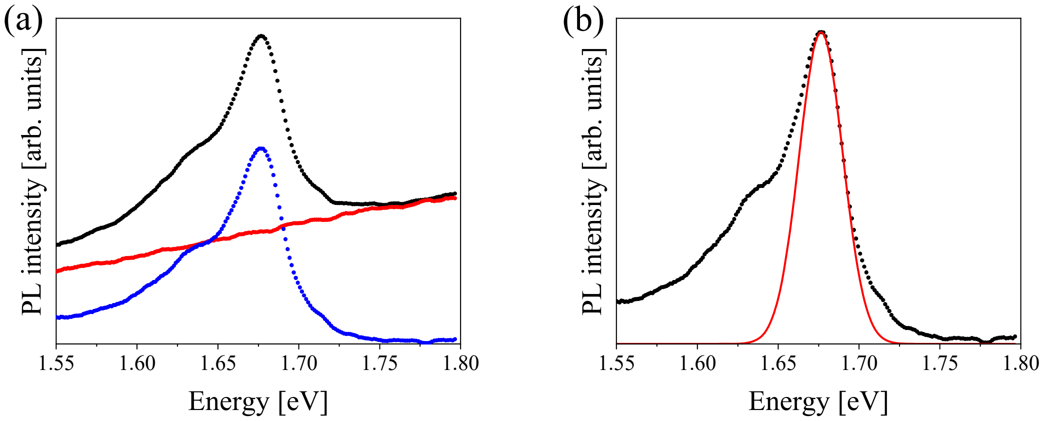

Figure 6.5 – (a) PL spectrum of SiV-DNDs plotted as black dots. Red dots in (a) indicate PL spectrum of undoped-DNDs whose intensity is normalized by PL intensity of SiV-DNDs at 1.80 eV. Blue dots in (a) are subtracted spectrum between SiV-DNDs and undoped-DNDs. (b) Gaussian fitting curves for the subtracted spectrum in (a). Black dots and a red line in (b) indicate original data and a fitted curve, respectively.

6.3.2.2 Temperature-dependent photoluminescence spectra

I studied the temperature dependence of the luminescence intensity of the SiV-DNDs. Figures 6.6a and b show the PL spectra of the SiV- and undoped-DNDs at 4 to 300 K, normalized by the excitation power, respectively. As is clear from Figure 6.6c, the normalized spectra of the undoped-DNDs (Figure 6.6b) show that their spectral shapes are almost independent of temperature. Hence, the PL spectrum at 4 K, which exhibits the highest signal-to-noise ratio among the undoped-DND spectra, was used as the baseline for the $\mathrm{SiV^-}$ luminescence. The subtracted spectra in Figure 6.6d were obtained via the subtraction method described in Section 3.2.1. Hereinafter, the subtracted spectra are referred to as PL spectra from the $\mathrm{SiV^-}$ centers in DNDs. The ZPL intensity of the $\mathrm{SiV^-}$ centers was estimated by fitting the shape of the ZPL in the PL spectra with a Gaussian function. As shown in Figure 6.6e, the PL intensity I of the ZPL of $\mathrm{SiV^-}$ centers shows a temperature dependence expressed by the Arrhenius equation [166, 167]:

$$I = \frac{I_0}{1 + A\exp\left(\frac{-E_{\mathrm{a}}}{k_{\mathrm{B}}T}\right)}, \tag{6.1}$$

where I_0, A, k_{B}, and T are the PL intensity at the lowest temperature, a pre-exponential factor, Boltzmann constant, and temperature, respectively. The activation energy E_{a} obtained by the fitting is 21.2 meV. All the fitting parameters are summarized in Table 6.2. Thus, the $\mathrm{SiV^-}$ centers in DNDs show a typical thermally activated behavior.

Table 6.2 –Fitting parameters of Equation 6.1 by Arrhenius plot for ZPL intensity of SiV centers in DNDs

I_0 [arb. units]	A [arb. units]	E_{a} [meV]
$(4.4\pm0.2)\times10^5$	8.8±3.9	21.2±0.5

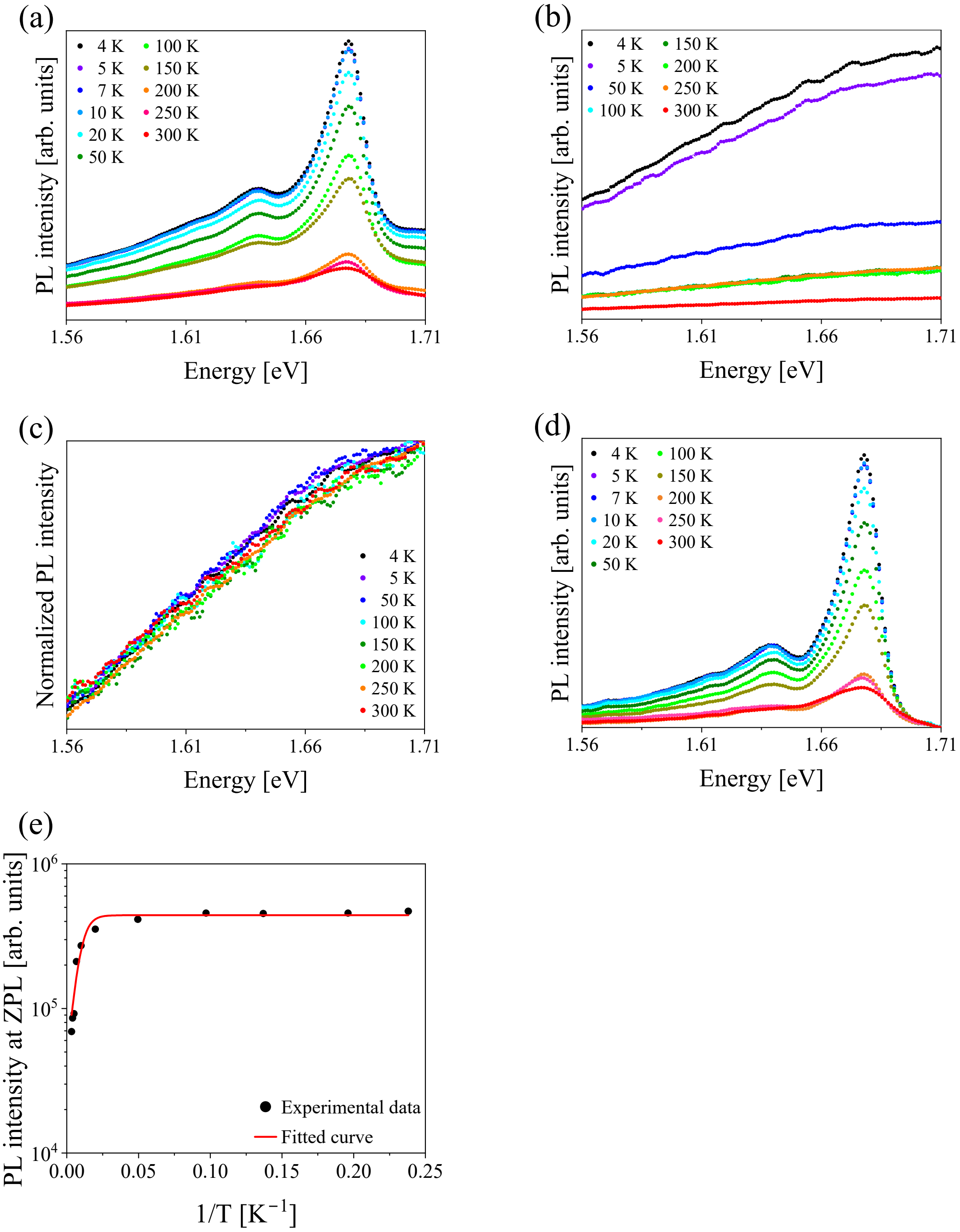

Figure 6.6 – PL spectra of (a) SiV-DNDs and (b) undoped-DNDs at each investigated temperature. (c) Normalized PL spectra of undoped-DNDs calculated from (b). (d) Subtracted spectra between PL spectra of SiV-DNDs at each temperature and undoped-DNDs at 4 K. (e) Temperature independence of PL intensity of SiV$^-$ centers in DNDs plotted as black dots. A red line is a fitted curve using the Arrhenius equation.

The luminescence linewidth and DWF of the SiV$^-$ centers at cryogenic temperatures are evaluated. The black dots in Figure 6.7 indicate the PL spectrum from the SiV$^-$ in DNDs at 4 K shown in Figure 6.6d by black dots. The ZPL in the spectrum can be well-fitted with a Gaussian curve, as indicated by a red line in Figure 6.7. The linewidth of the ZPL was 14 meV. The linewidth of the ZPL at 4 K is narrower than that at room temperature (Figure 6.5b). The value of the linewidth is discussed in Section 3.2.5.

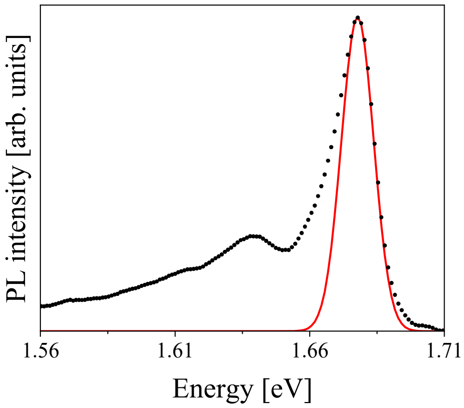

Figure 6.7 –PL spectra of SiV$^-$ centers in DNDs at 4 K indicated by black dots. A red line is a Gaussian fitting curve for subtracted spectra.

6.3.2.3 Excitation energy-dependent photoluminescence spectra

The excitation energy dependence of the luminescence intensity from the SiV$^-$ in DNDs was investigated via PL measurements at room temperature using excitation energy ranging from 1.80 to 3.54 eV. The PL spectra of the SiV$^-$ centers in DNDs shown in Figure 6.8a were obtained as subtracted spectra of the SiV- and undoped-DNDs normalized in intensities at 1.80 eV (excitation energy: 2.03–3.02 eV). In the case of the excitation energies of 1.80–1.97 and 3.54 eV, the PL intensity could not be normalized at 1.80 eV because a low-pass filter of 1.70 eV was used to prevent the output of the excitation laser or its seed laser from mixing into the spectra. Therefore, the PL intensities of undoped-DNDs excited by these energies were adjusted so that the shapes of their subtracted spectra were similar to those with excitation energies of 2.03–3.02 eV. In addition, it was difficult to normalize the intensity of the spectra of the SiV- and undoped-DNDs obtained using an excitation laser of 3.18 eV at 1.80 eV since their PL intensities and signal-to-noise ratios are low. Therefore, the PL intensity of the undoped-DNDs excited at 3.18 eV was normalized by the same method used for the spectra excited at 1.80–1.97 and 3.54 eV. As shown in Figure 6.8b, the photoluminescence excitation (PLE) spectrum was obtained by plotting the PL intensity at the ZPL of SiV⁻ center against the excitation energy. The PLE spectrum shows a broad band with a peak at 2.3 eV. This band is consistent with the PLE spectrum of SiV⁻ centers in bulk-sized diamonds reported by Häußler *et al.* [65]. In addition, a low-energy tail of the ZPL is observed, reflecting on the lower broadening of the energy level of the SiV⁻ centers in DNDs.

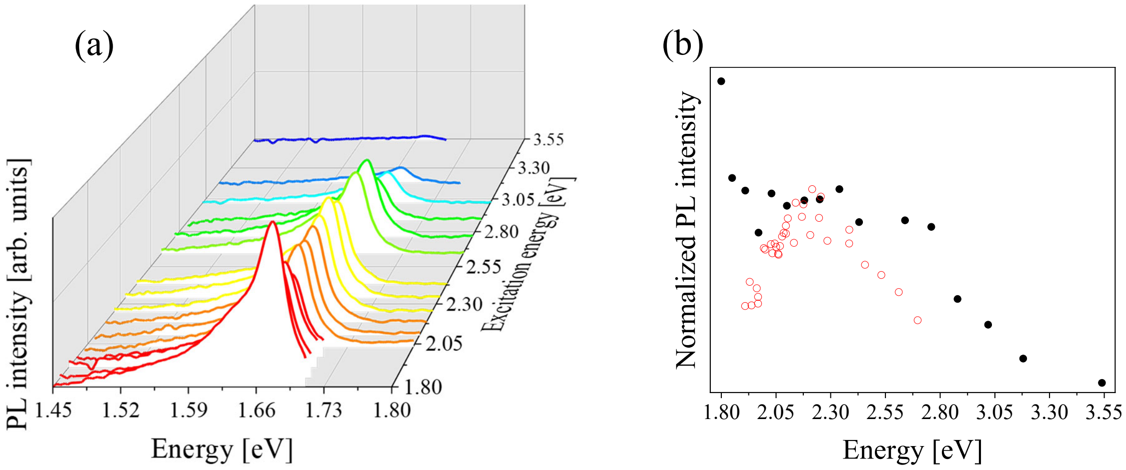

Figure 6.8 – (a) PL spectra as a function of excitation energy for SiV⁻ centers in DNDs. (b) PLE spectrum produced by plotting PL intensity at 1.68 eV against excitation energy in (a) as black dots. PLE spectrum of typical SiV⁻ center reported by Häußler *et al.* is plotted as red circles [65]. PL intensities of SiV⁻ centers in DNDs and typical SiV⁻ center are normalized by PL intensity excited at 2.3 eV.

6.3.2.4 Time-resolved photoluminescence spectra

Time-resolved spectroscopy was performed using the streak camera to measure a luminescence lifetime of the SiV⁻ centers in DNDs excited at 2.34 eV. Figures 6.9a and b show time-resolved PL spectra around the SiV⁻-ZPL at 1.68 eV during approximately 100 ns and its time-integrated spectrum, respectively. The luminescence peak of the SiV⁻ centers is observed in those spectra. Figures 6.9c and d show decay curves for the luminescence from the SiV-DNDs; these curves were extracted by integrating over the spectral ranges of 1.65–1.72 and 1.76–1.84 eV in Figure 6.9a, respectively. The luminescence from the SiV⁻ centers is observed only in the range of 1.65–1.72 eV. Both decay curves reach baselines after ~90 ns. Since the well-known luminescence lifetime of SiV⁻ centers in bulk-sized diamonds is 1.0–2.4 ns [52], the decay curves have long-lived components unrelated to the SiV⁻ centers in DNDs and related to the presence of other defects in the DNDs. The time constants of long-lived components are calculated by fitting both decay curves in the time domain after 25 ns using the following formula,

$$F(t) = F_0 + F_{\mathrm{Long}}\exp\left(-t/\tau_{\mathrm{Long}}\right), \tag{6.2}$$

where F_0 is the baseline, and F_{Long} and τ_{Long} denote the pre-exponential factor and the lifetime of the long-lived component, respectively. Both decay curves were successfully fitted with a common τ_{Long} = ~10 ns, as shown in Figures 6.9e and f. All fitting parameters were reported in Table 6.3. An example of a diamond defect exhibiting a luminescence lifetime of ~10 ns is NV center [168, 169], which is widely observed in DNDs [170].

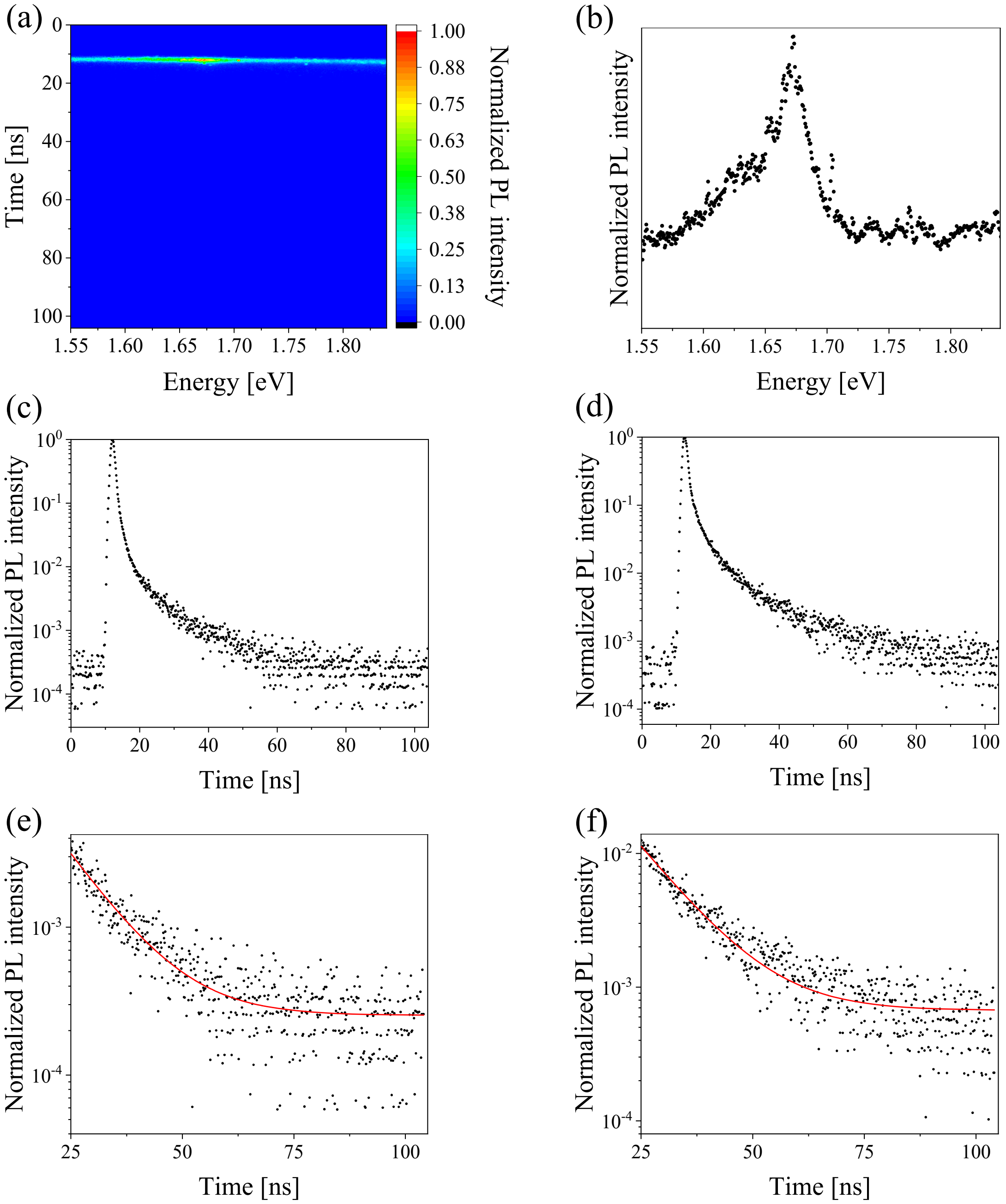

Figure 6.9 – (a) Time-resolved PL spectrum around ZPL of SiV^- centers in DNDs excited at 2.34 eV. (b) Time-integrated spectrum at all measurement times in (a). Decay curves of luminescence in ranges of (c) 1.65–1.72 and (d) 1.76–1.84 eV. Magnified views of (c, d) in time regions from 25 to 104 ns are shown in (e, f), respectively. Black dots and red lines indicate the experimental data and fitted curves based on Equation 6.2, respectively.

Table 6.3 – Parameters for the decay curves represented in Figures 6.9e and f fitted by Equation 6.2.

Energy range [eV]	F_0 [arb. units]	F_{Long} [arb. units]	τ_{Long} [ns]
1.65–1.72	2.5×10^{-4}	0.04±0.03	10.1±0.3
1.76–1.84	6.7×10^{-4}	0.12±0.01	10.5±0.2

To investigate the short luminescence components of the SiV-DNDs luminescence, time-resolved spectra were recorded over a time range of approximately 20 ns. Figures 6.10a and b show PL decay around the ZPL of the SiV^- centers and its time-integrated spectrum, respectively. Figures 6.10c and d show the luminescence decay curves extracted by integration over the ranges of 1.65–1.72 and 1.76–1.84 eV in Figure 6.10a, respectively. These luminescence decay curves can be expressed by setting τ_{Long} = 10 ns, as follows:

$$F'(t) = F'_0 + \sum_{i=1}^{N} F_i \exp(-t/\tau_i) + F_{\mathrm{Long}} \exp\left(-t/\tau_{\mathrm{Long}}\right), \tag{6.3}$$

where F'_0 is the baseline, F_i and F_{Long} are pre-exponential factors, and τ_i denotes lifetimes. As shown in Figure 6.10c, the decay curve of the luminescence in the range of 1.65–1.72 eV is well-fitted with the *tetra*-exponential model ($N = 3$ in Equation 6.3). On the other hand, the luminescence decay curve in the range of 1.76–1.84 eV indicated in Figure 6.10d is successfully fitted with *tri*-exponential components ($N = 2$ in Equation 6.3). These fitting parameters are shown in Table 6.4. Because τ_1, τ_2, and τ_{Long} are commonly observed in both decay curves, these are presumed to be the same components originating from the ND structure. The time constant of τ_3 = 0.56±0.04 ns was observed only from the decay curve in the range of 1.65–1.72 eV which contains the SiV⁻-ZPL.

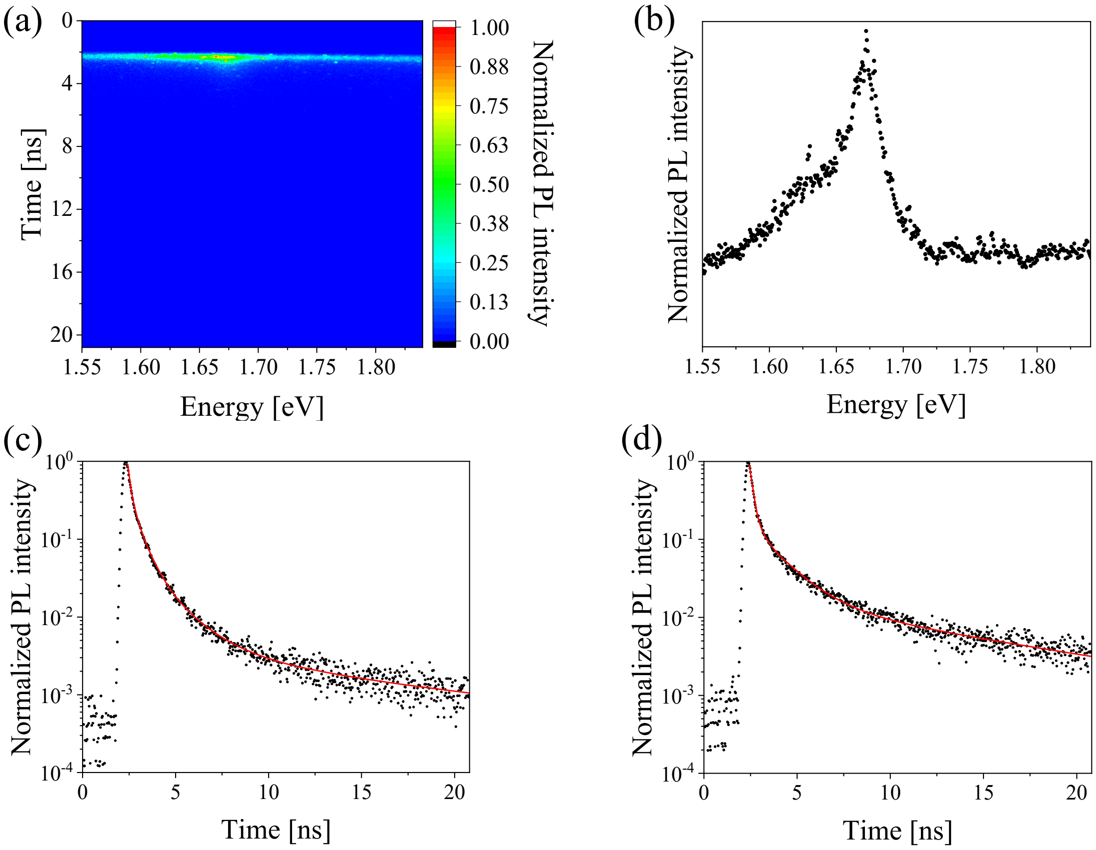

Figure 6.10 – (a) Time-resolved PL spectrum around ZPL of SiV⁻ centers in DNDs excited at 2.34 eV. (b) Time-integrated spectrum at all measurement times in (a). Decay curves of the luminescence in ranges of (c) 1.65–1.72 and (d) 1.76–1.84 eV. Black dots and red lines indicate experimental data and fitted curves based on Equation 6.3, respectively.

Table 6.4 – Fitting parameters of Equation 6.3 for decay curves of luminescence from SiV-DNDs.

Energy range [eV]	F_0 [arb. units]	F_1 [arb. units]	τ_1 [ns]	F_2 [arb. units]	τ_2 [ns]	F_3 [arb. units]	τ_3 [ns]	F_{Long} [arb. units]
1.65–1.72	3.5×10^{-4}	0.56±0.02	0.16±0.01	0.06±0.02	1.6±0.2	0.31±0.01	0.56±0.04	$(4.4\pm0.5)\times10^{-3}$
1.76–1.84	4.4×10^{-4}	0.74±0.01	0.20±0.01	0.14±0.01	1.5±0.1	N.A.[a)]	N.A.[a)]	$(1.7\pm0.1)\times10^{-2}$

[a)] N.A.: Not Applicable.

Two additional experiments were conducted to verify the correctness of the fittings in Figures 6.10c and d. Firstly, the decay curve fitted with the *tri*-exponential model shown in Figure 6.10d was attempted to express using a *tetra*-exponential model having an additional component with a time constant of 0.56 ns. However, the component of 0.56 ns did not substantially contribute to the fitting results, as shown in Figure 6.11 and Table 6.5. Secondly, Figures 6.12a and b are decay curves in the range of 1.65–1.72 eV with SiV⁻ centers obtained from other spots (i) and (ii) in the drop-cast sample, respectively. These were also fitted by *tetra*-exponential models with the same fitting parameters reported in Table 6.4 including τ_3 in the range of 0.56±0.04 ns, as shown in the red lines in Figure 6.12 and the value of Table 6.6. These results suggest that the component with the time constant 0.56 ns in the range of 1.65–1.72 eV is attributable to luminescence from the SiV⁻ centers.

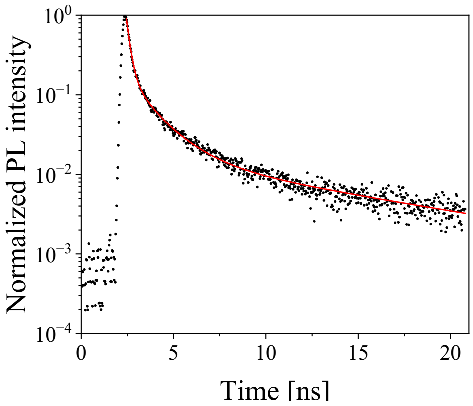

Figure 6.11 – Decay curve of luminescence in the range of 1.76–1.84 eV (same as the black dots in Figure 6.10d). Black dots and a red line indicate experimental data and a fitted curve based on *tetra*-exponential components, respectively.

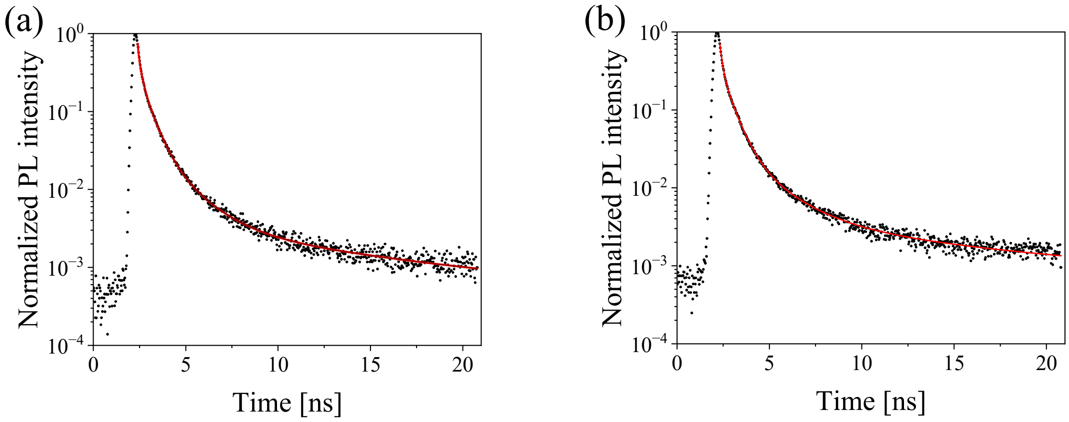

Figure 6.12 – (a, b) Decay curves of luminescence in the range of 1.65–1.72 eV from other spots (i, ii) in the drop-cast sample, respectively. Black dots and red lines indicate experimental data and fitted curves based on *tetra*-exponential components, respectively.

Table 6.5 – Fitting parameters of *tri*-exponential for a decay curve of luminescence of 1.76–1.84 eV from SiV-DNDs.

F_0 [arb. units]	F_1 [arb. units]	τ_1 [ns]	F_2 [arb. units]	τ_2 [ns]	F_3 [arb. units]	τ_3 [ns]	F_{Long} [arb. units]
4.4×10^{-4}	0.69±0.01	0.18±0.01	0.12±0.01	1.5±0.1	0.081±0.024	0.56 (constant)	$(1.8\pm0.1)\times10^{-2}$

Table 6.6 – Fitting parameters of *tetra*-exponential for decay curves of luminescence of 1.65–1.72 eV from SiV-DNDs.

spot	F_0 [arb. units]	F_1 [arb. units]	τ_1 [ns]	F_2 [arb. units]	τ_2 [ns]	F_3 [arb. units]	τ_3 [ns]	F_{Long} [arb. units]
i	4.0×10^{-4}	0.51±0.01	0.13±0.01	0.05±0.01	1.6±0.2	0.29±0.01	0.55±0.02	$(3.6\pm0.3)\times10^{-3}$
ii	7.0×10^{-4}	0.43±0.01	0.13±0.01	0.04±0.01	1.9±0.1	0.31±0.01	0.58±0.01	$(4.0\pm0.2)\times10^{-3}$

The contribution of the component of time constant 0.56 ns for the luminescence from the SiV^- centers was evaluated by the two different sets of experimental data shown in Table 6.7: the decay curve (Figure 6.10c) and the PL spectrum in the range of 1.65–1.72 eV. The contribution calculation based on the time-integrated PL spectrum is performed using the PL spectra shown in Figure 6.5a, which were recorded under the same conditions as the time-resolved spectroscopic measurements. A_{Subt} and $A_{\mathrm{SiV-DNDs}}$ are the areas of the subtracted and the raw PL spectra of the SiV-DNDs represented by blue and black dots in Figure 6.5a in the energy range of 1.65–1.72 eV, respectively. Since the value calculated by the decay curve is consistent with that by the PL spectrum, the lifetime of the SiV^- centers in the DNDs is determined to be 0.56±0.04 ns.

Table 6.7 – Contribution of luminescence from SiV^- centers in DNDs.

Calculation method of contribution	Decay curve	Spectrum
	$F_3\tau_3/\sum F_i\tau_i + F_{\mathrm{Long}}\tau_{\mathrm{Long}}$	$A_{\mathrm{Subt}}/A_{\mathrm{SiV-DNDs}}$
Calculated value	0.43	0.50

Although the luminescence lifetime of 0.56±0.04 ns obtained in the present study for the SiV-DNDs is shorter than the well-known luminescence lifetime of SiV^- centers (1.0–2.4 ns) [52], the shortest luminescence lifetime is 0.2 ns [171] among the previous reports. In addition, SiV^- centers constructed with 5 nm-sized DNDs using a high-temperature annealing technique have been reported to exhibit a luminescence lifetime of 0.4 ns [137]. The luminescence lifetime of the SiV^- centers in DNDs presented by this study is within the range of values reported previously. Note that the determined luminescence lifetime of SiV^- centers in DNDs (0.56±0.04 ns) is considered an average value for the large number of the SiV-DNDs in the excitation spot of the drop-cast samples. According to the previous studies of NV centers, the luminescence lifetimes of color centers in NDs differ among individual particles and exhibit distribution slightly.

6.3.2.5 *Effect of particle size on the optical properties of silicon-vacancy centers in detonation nanodiamonds*

Table 6.8 shows the key optical properties of the SiV^- centers in DNDs measured in a series of spectroscopic experiments in this study, along with those of typical SiV^- centers in bulk-sized diamonds. According to the linewidths, the ZPL of SiV^- centers in DNDs exhibits greater homogeneous and inhomogeneous broadening than the ZPL of typical ones. The broadening of the ZPL absorption band is also observed in the PLE spectrum, as shown in Figure 6.8b. Focusing on the time-resolved PL, the luminescence lifetime of the SiV^- centers in DNDs is shorter than that of typical SiV^- centers by approximately one-half. Therefore, the homogeneous broadening of the ZPL of SiV^- centers in DNDs at room temperature can be estimated to be ~20 meV if I assume the time–energy uncertainty relation. Because the linewidth is determined by the sum of homogeneous and inhomogeneous broadening, the inhomogeneous broadening of the SiV^- centers in DNDs is estimated to be ~12 meV at room temperature. The estimated inhomogeneous broadening is roughly consistent with the linewidth at the cryogenic condition, where the homogeneous broadening is maximally suppressed. The broad homogeneous linewidth and short lifetime of the SiV^- centers in DNDs indicate an increase in the nonradiative transition probability derived from an enhancement of electron–phonon coupling. The increase and enhancement are evident in the decrease in the DWF compared with that of typical SiV^- centers. Furthermore, quantum efficiency of the SiV^- centers in DNDs is also relatively small as shown in Table 6.8, which was calculated as 8.7% on the basis of the luminescence lifetime of 0.56 ns and its natural radiative lifetime of 6.24 ns [158]. The possible causes of the change in the electronic state of the SiV^- centers in DNDs are the distortion of their split-vacancy structure and the influence of the surface potential owing to the specific small particle size of the SiV-DNDs. The extremely small size, ~10 nm, the more sensitive the internal SiV^- centers are to such surface effects compared with typical ones. Moreover, the small particle size also affects the inhomogeneous broadening. The energy levels of each SiV^- center fluctuate with the lattice distortions. The dependence of the ZPL peak position of the SiV^- center on the stress in the diamond lattice has been reported in detail [172, 173]. The detonation process does not completely control the distance of each SiV^- center from the surface in DNDs. The location of each color center in the DNDs varies from the center to the surface. The lattice distortion is inhomogeneously distributed around the SiV-structures according to the distance from the surface. Because the SiV-DND sample used in the present study is an aggregate of particles, the PL spectra are observed as an ensemble of individually peak-shifted ZPLs, reflecting inhomogeneous broadening. As summarized above, the SiV^- centers in DNDs exhibit unique optical properties reflecting the particle size effect of the DNDs—the enhancement of electron–phonon coupling and the increase in nonradiative transition probability—and their inhomogeneous distribution.

Table 6.8 – Optical properties of the SiV$^-$ centers in DNDs and typical SiV$^-$ centers.

Spectroscopic method	Optical properties	SiV$^-$ centers in DNDs	Typical SiV$^-$ centers in bulk-sized diamond
PL	Linewidth (FWHM[a])	32 meV at rt[b)] 14 meV at 4 K	~12.1 meV at rt[b)] [65] ~11.4 meV at rt[b)] [82] 10.2 meV at rt[b)] [77] 0.7 meV at 5 K [77]
Ditto	DWF at rt[b)]	0.47	0.67 [65]
Time-resolved PL	Luminescence lifetime	0.56±0.04 ns	1.2 ns [82]
Ditto	Quantum efficiency	8.7%[c)]	19%[c)]

[a)] Full-width at half-maximum; [b)] room temperature; [c)] ratio of natural radiative lifetime to experimentally determined luminescence lifetime indicated in this table.

The literature contains some reports on the fabrication of the SiV$^-$ centers in NDs and the characterization of their optical properties. In 2021, Shimazaki *et al.* demonstrated the SiV$^-$ centers formation by high-temperature annealing at 1100 °C of DNDs containing silicon as a trace impurity [137]. I compare the optical properties of two types of SiV$^-$ centers in DNDs, where the SiV$^-$ centers were formed using different fabrication methods. The DNDs with SiV$^-$ centers created by the post-treatment exhibited a ZPL with a minimum linewidth of 17.8 meV and a luminescence lifetime of 0.4 ns at room temperature. This linewidth might correspond to the homogeneous linewidth because high-temperature annealing is known to dramatically decrease the inhomogeneous linewidth of the SiV$^-$ centers [136]. The estimated homogeneous linewidth and luminescence lifetime are consistent for the SiV$^-$ centers in DNDs created by the *in situ* synthesis during the detonation reaction and the post-treatment. These results mean that the two types of SiV$^-$

centers in DNDs are commonly affected by the effect of their very small particle size of DNDs, regardless of the creation methods.

6.3.2.6 Photostability

The photostability of the SiV⁻ centers in DNDs is investigated, which is a key property for applications such as fluorescent markers. In 2016, Reineck *et al.* characterized the photostability of various fluorescent markers in detail by measuring their luminescence intensity over time [159]. According to their experiments, the fluorescent dye Alexa Fluor 647, Au nanoclusters, and carbon dots decreased luminescence intensity within a few minutes. In contrast, carbon nanotubes (CNTs) and NDs containing NV centers exhibited perfect photostability without fading. The measurement results of the SiV⁻ centers in DNDs are shown in Figure 6.13. The SiV⁻ centers in DNDs emit stable luminescence with no decrease in intensity, similar to CNTs and NV centers in NDs.

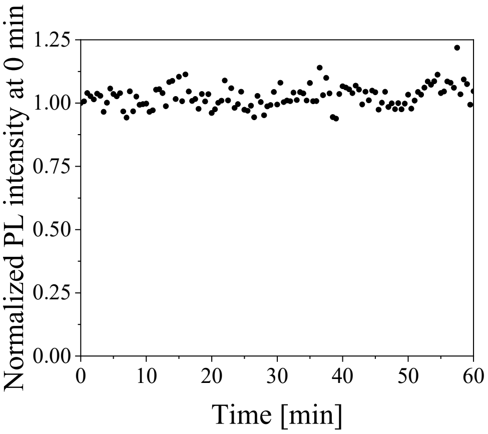

Figure 6.13 – Luminescence intensity for ZPL of SiV⁻ centers in DNDs, recorded at 15 s intervals. The ZPL intensity was counted after its baseline removals and was normalized by initial intensity at 0 min.

6.3.3 Optical properties of germanium-vacancy centers in detonation nanodiamonds

6.3.3.1 Photoluminescence spectra

Figure 6.14a shows the PL spectra of the GeV-DNDs excited by 2.34 eV at room temperature, as black dots. Their broadband backgrounds luminescence from the diamond structures were subtracted by the same method employed in Section 3.2.1. Red and blue dots in Figure 6.14a are the PL spectra of the undoped-DNDs and subtracted spectra, respectively. The PL intensities of undoped-DNDs are normalized by one of the GeV-DNDs at 2.20 eV. Although an unassigned peak at 1.98 eV remains in the subtracted spectrum, the subtracted one shows the ZPL of GeV⁻ center at 2.06 eV. The unassigned peak is discussed in detail later. Figure 6.14b shows that the ZPLs of GeV⁻ centers in the subtracted spectra can be well-fitted with a Gaussian curve. The ZPL linewidth and DWF are 59 meV and 0.19, respectively.

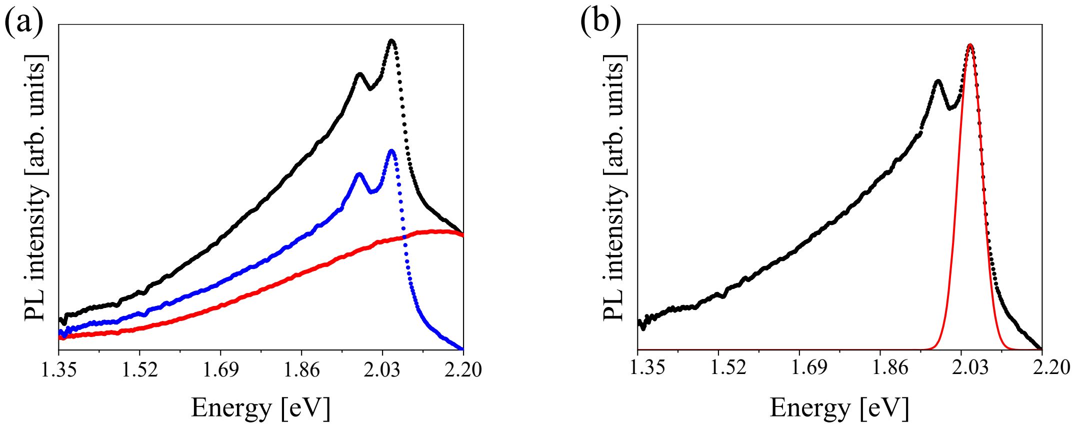

Figure 6.14 – (a) PL spectra of GeV- and undoped-DNDs plotted as black and red dots, respectively. PL intensity of undoped-DNDs is normalized by one of GeV-DNDs at 2.20 eV. Blue dots in (a) indicate subtracted spectrum between GeV- and undoped-DNDs. (b) Gaussian fitting curves for the subtracted spectrum in (a). Black dots and a red line show original data and a fitted curve, respectively.

6.3.3.2 Temperature-dependent photoluminescence spectra

Temperature dependence of luminescence from the GeV$^-$ centers in DNDs was investigated. The PL spectra of the GeV- and undoped-DNDs at 4 to 300 K normalized by the excitation power, as shown in Figures 6.15a and b, respectively. The spectra shapes of the undoped-DNDs show temperature variation, unlike the SiV-DNDs case: therefore, the undoped-DNDs spectra at corresponding temperatures were adopted as baselines for the GeV-DNDs spectra. Subtracted spectra obtained by the above method are shown in Figure 6.15c (the subtraction detail described in Section 3.2.1). Hereafter, the subtracted spectra created by the method are represented as PL spectra of the GeV$^-$ centers in DNDs. They have a sharp peak at 2.06 eV, corresponding to the ZPL of the GeV$^-$ center, and the unassigned peak at 1.98 eV. Both peak intensities were estimated by a Gaussian fitting and then fitted by the Arrhenius Equation 6.1, as shown in Figure 6.15d, using the parameters reported in Table 6.9. According to Arrhenius plots, the GeV$^-$ centers in DNDs also show a typical thermally activated behavior, as the SiV$^-$ centers in DNDs. In addition, the unassigned peak indicates the same thermal behavior with approximately identical E_a to the ZPL.

Table 6.9 – Fitting parameters of Equation 6.1 by Arrhenius plot for PL intensities of GeV$^-$-ZPL and unassigned peak.

Peak	I_0 [arb. units]	A [arb. units]	E_a [meV]
ZPL at 2.06 eV	$(3.9\pm0.1)\times10^5$	10.1±4.7	36.7±7.6
Unassigned peak at 1.98 eV	$(2.9\pm0.1)\times10^5$	12.0±7.9	43.4±11.5

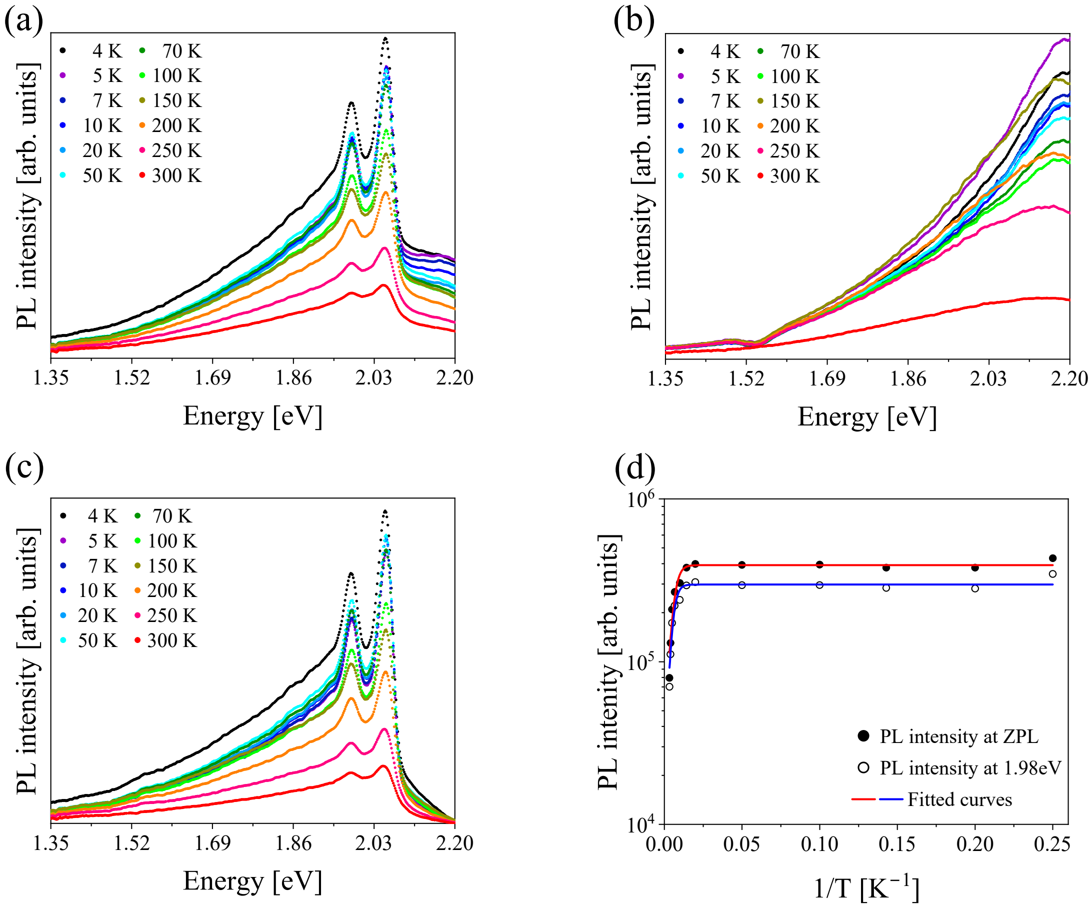

Figure 6.15 – PL spectra of (a) GeV- and (b) undoped-DNDs at each investigated temperature. (c) Subtracted spectra between PL spectra of GeV-DNDs and undoped-DNDs at each temperature. (d) Temperature independence of PL intensities of ZPL of GeV$^-$ centers in DNDs (black dots) and the unassigned peak at 1.98 eV (circles). Red and blue lines are curve-fitted using Arrhenius equation.

Figure 6.16 shows the spectrum of the GeV⁻ centers at 4 K as black dots. I calculated the ZPL linewidth of GeV⁻ centers in DNDs under cryogenic temperature. The spectrum is well-fitted with Gaussian curves as indicated by a red curve in Figure 6.16. The linewidth of the GeV⁻ centers in DNDs is 41 meV, which is narrower than those at room temperature (Figures 6.14b).

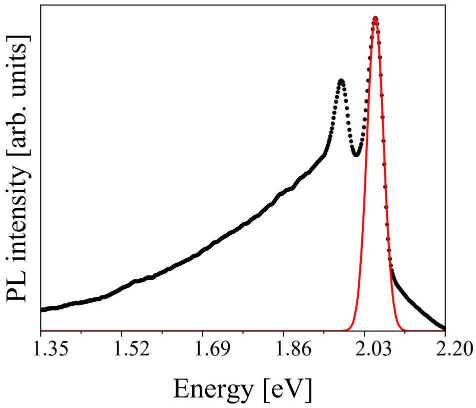

Figure 6.16 – PL spectra of GeV⁻ centers in DNDs at 4 K. Black dots and a red curve show original data and Gaussian fitting curve.

6.3.3.3 Excitation energy-dependent photoluminescence spectra

I also investigated the excitation energy dependence of the luminescence intensity from the GeV-DNDs. Figure 6.17a is the subtracted PL spectra between the GeV- and undoped-DNDs excited by 2.38–3.54 eV. Figure 6.17b shows PLE spectra of the ZPL of GeV⁻ center at 2.06 eV and the unassigned peak at 1.98 eV, prepared from Figure 6.17a. The excitation energy dependence of the PL intensity of the unassigned peak shows the same behavior as the one of the GeV⁻ centers. The PLE spectra of the two peaks have a peak at 2.8 eV and a second peak on its lower energy side that is presumed to correspond to the ZPL. The shape of the second peaks is consistent with the PLE spectra of typical GeV⁻ centers in bulk-sized diamonds reported by Häußler *et al.* [65].

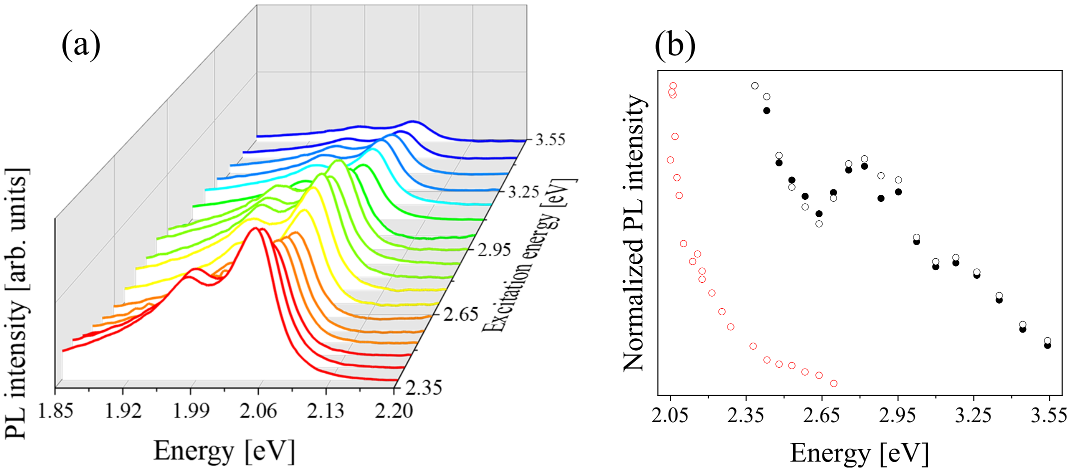

Figure 6.17 – (a) PL spectra versus excitation energy for GeV⁻ centers in DNDs prepared by subtracted PL spectra of the GeV- and undoped-DNDs. (b) PLE spectra were constructed by plotting PL intensity of GeV⁻-ZPL at 2.06 eV and unassigned peak at 1.98 eV against the excitation energy in (a) as black dots and circles, respectively. The PLE spectrum of typical GeV⁻ centers based on Häußler *et al.* is plotted as red circles [65]. This PLE spectrum is normalized to compare the one of GeV⁻ centers in DNDs.

6.3.3.4 Time-resolved photoluminescence spectra

The luminescence lifetime of the GeV⁻ centers in DNDs was investigated. Figures 6.18a and b show a time-resolved PL spectrum around the ZPL of GeV⁻ centers during approximately 1000 ns and its time-integrated spectrum, respectively. These spectra consist of the ZPL of the G4V centers at 2.06 eV and the unassigned peak at 1.98 eV, as in the previous PL studies. Figure 6.18c shows luminescence decay curves integrated over the spectral range of 2.01–2.07 eV including the ZPL from Figure 6.18a. Figure 6.18d shows a luminescence decay curve in the higher energy range, 2.10–2.17 eV, compared with the ZPL of Figure 6.18a. These decay curves reach baseline after ~400 ns and contain longer components with several hundred nanoseconds which are too long compared with the well-known lifetimes of GeV^{-} centers of 1.4–5.5 ns [83]. The time constants for these long-lived components could not be determined using Equation 6.2 owing to the low signal-to-noise in their corresponding time region in Figures 6.18c and d. Therefore, the investigation of the luminescence lifetime of the GeV^{-} centers in DNDs could not employ the procedure for that of the SiV^{-} centers in DNDs.

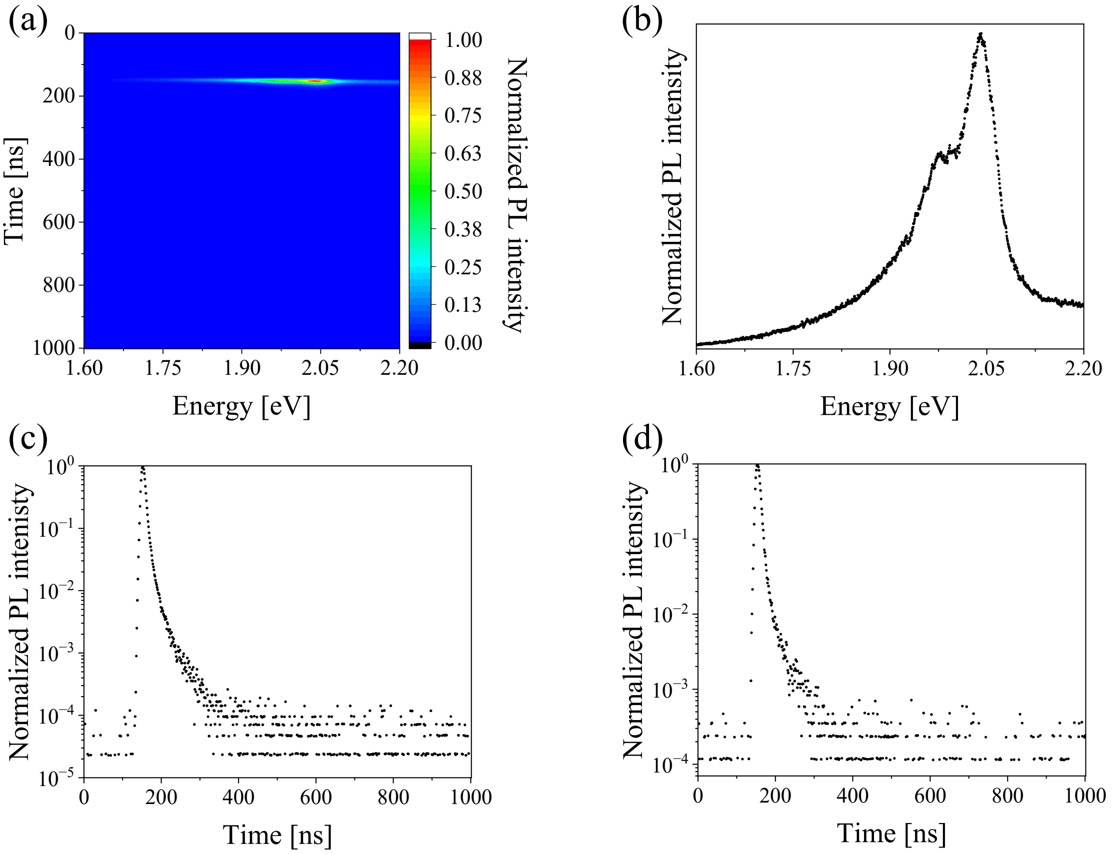

Figure 6.18 – (a) Time-resolved PL spectrum around ZPL of GeV^{-} centers in DNDs excited at 2.38 eV. (b) Time-integrated spectrum at all measurement times in (a). Decay curves of luminescence in ranges of (c) 2.01–2.07 and (d) 2.10–2.17 eV.

Figure 6.19a shows a time-resolved PL spectrum from the GeV-DNDs whose time scale is approximately 100 ns to investigate the luminescence lifetime of the GeV⁻ centers in DNDs. Figure 6.19b is a time-integrated spectrum of Figure 6.19a. Figures 6.19c and d indicate luminescence decay curves extracted by integration over the ranges of 2.01–2.07 and 2.10–2.07 eV in Figure 6.19a, respectively. These luminescence decay curves can be expressed in Equation 6.4 which excludes the contribution of long-lived components from Equation 6.3, as follows:

$$F'^{(t)} = F'_0 + \sum_{i=1}^{N} F_i \exp(-t/\tau_i)\,. \tag{6.4}$$

As shown in Figure 6.19c, the luminescence decay curve including the ZPL of GeV⁻ centers is well-fitted with the *tri*-exponential model ($N = 3$ in Equation 6.4) using values of Table 6.10. The precision of $\tau_3 = 25$ ns is not precise because it involves long components that could not be determined by the 1000 ns time scale measurement in Figure 6.18. On the other hand, the luminescence decay curve without the ZPL shown in Figure 6.19d does not fit Equation 6.4, even for the *tetra*-exponential model ($N = 4$ in Equation 6.4). This result indicates that the luminescence in the range of 2.10–2.17 eV has numerous components. Since common components could not be found for the decay curves with and without the ZPL of GeV⁻ centers in DNDs, the luminescence lifetime of the GeV⁻ centers in DNDs is determined solely by the fitting parameters for the decay curve in Figure 6.19c. The time constant of $\tau_3 = 25$ ns is too long compared to the luminescence lifetime of the typical GeV⁻ center (1.4–5.5 ns) and is therefore excluded as a candidate for one of the GeV⁻ centers in DNDs [83]. In the case of SiV⁻ centers in DNDs, their luminescence lifetime is shorter than that of typical SiV⁻ centers. Following the case of SiV⁻ centers, the luminescence lifetime of the GeV⁻ centers in DNDs is probably shorter than that of typical GeV⁻ centers of 1.4–5.5 ns. However, this study cannot rule out $\tau_2 = 7.1$ ns, similar to the luminescence lifetime of typical GeV⁻ centers. Namely, the luminescence lifetime of the GeV⁻ centers in DNDs ranges from 1.3 to 7.1 ns.

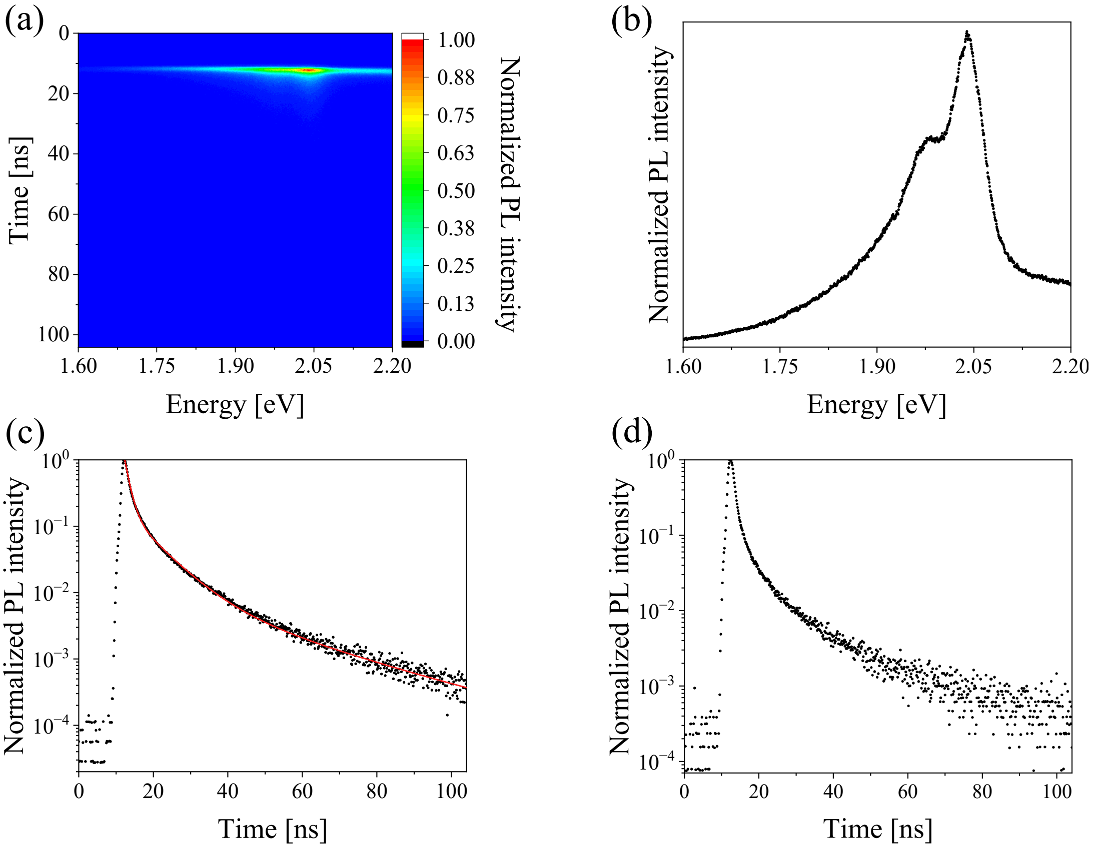

Figure 6.19 – (a) Time-resolved PL spectrum around ZPL of GeV⁻ centers in DNDs excited at 2.38 eV. (b) Time-integrated spectrum at all measurement times in (a). Decay curves of the luminescence in ranges of (c) 2.01–2.07 and (d) 2.10–2.17 eV. Black dots and a red line indicate experimental data and a fitted curve based on Equation 6.4, respectively.

Table 6.10 – Fitting parameters of *tri*-exponential for a decay curve of luminescence of 2.01–2.07 eV from GeV-DNDs.

F_0 [arb. units]	F_1 [arb. units]	τ_1 [ns]	F_2 [arb. units]	τ_2 [ns]	F_3 [arb. units]	τ_3 [ns]
5.5×10^{-5}	0.93±0.01	1.3±0.02	0.16±0.01	7.1±0.4	0.012±0.003	25[a)]

[a)] Accuracy of this value is not guaranteed because the effect of long-lived components is not taken into consideration.

In order to attribute the unassigned peak at 1.98 eV in the luminescence spectrum of the GeV-DNDs, its time constant is investigated. Black dots in Figures 6.20 a and b show the decay curves extracted by integration over the ranges of 1.94–1.99 eV in Figures 6.18a and 6.19a, respectively. These decay curves are consistent with those of 2.01–2.07 eV indicated by red dots in Figures 6.20a and b (including the ZPL, same as the black dots in Figures 6.18c and 6.19c, respectively). While the time constant of the peak at 1.98 eV cannot be determined, the luminescence with the peak is composed of the same components as the luminescence containing the GeV⁻ center's ZPL in the range of 2.01–2.07 eV.

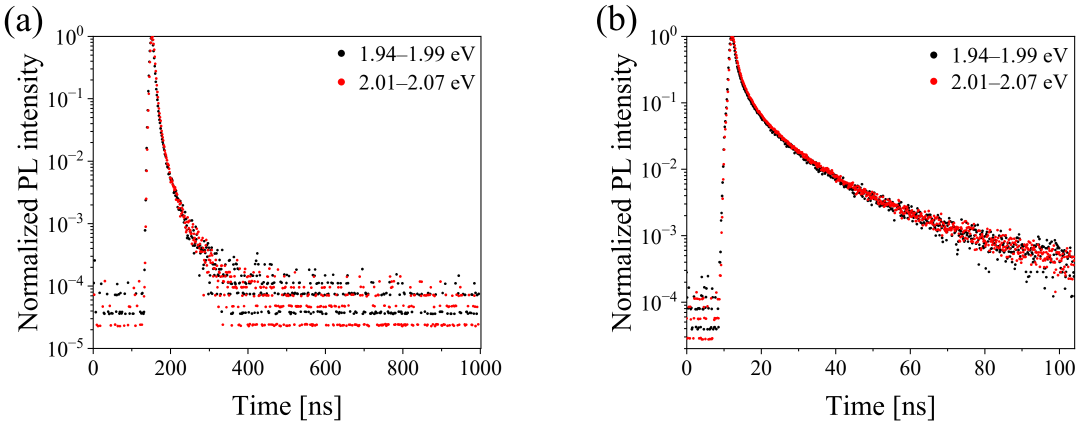

Figure 6.20 – Decay curves of the luminescence in ranges of 1.94–1.99 and 2.01–2.07 eV. (a) and (b) are produced from time-resolved PL spectra of Figures 6.18a and 6.19a, respectively.

6.3.3.5 Effect of particle size on the optical properties of germanium-vacancy centers in detonation nanodiamonds

Table 6.11 summarizes the optical properties of the GeV^- centers in DNDs measured in this study and typical GeV^- centers in bulk-sized diamonds. There are fewer detailed reports on the optical properties of typical GeV^- centers compared with those of typical SiV^- centers; in particular, their luminescence lifetime has not been precisely determined. In this study, the GeV^- centers in DNDs exhibited >3.5 times greater linewidth at room temperature and ~30% DWF than the typical GeV^- centers. These results indicate that the GeV^- centers in DNDs also have enhanced electron–phonon coupling compared with the typical GeV^- centers because of the particle size effects of DNDs, as with the SiV^- centers in DNDs. In addition, because the linewidths exhibited from the GeV^- centers in DNDs at cryogenic temperature are sufficiently broad, they have inhomogeneous broadening derived from the detonation process, as same as the SiV^- centers in DNDs.

Table 6.11 – Optical properties of the GeV^- centers in DNDs and typical GeV^- centers.

Spectroscopic method	Optical properties	GeV^- centers in DNDs	Typical GeV^- centers in bulk-sized diamond
PL	Linewidth (FWHM[a)])	59 meV at rt[b)] 41 meV at 4 K	~17.1 meV at rt[b)] [52, 83] ~22.2 meV at rt[b)] [174] 7.5 meV at 80 K [174]
Ditto	DWF at rt[b)]	0.19	~0.6 [64, 83]
Time-resolved PL	Luminescence lifetime	1.3–7.1 ns	1.4–5.5 ns [83]

[a)] Full-width at half-maximum; [b)] room temperature.

6.3.3.6 Attribution of the peak at 1.98 eV from germanium-vacancy centers-containing detonation nanodiamonds

The luminescence from GeV-DNDs contained the unassigned peak at 1.98 eV in addition to the ZPL. The ZPL of GeV^- centers and unassigned peaks exhibited identical temperature and excitation energy dependence. Furthermore, the shapes of luminescence decay curves from those peaks were perfectly consistent. The agreements of these optical responses indicate that the peak at 1.98 eV is the ZPL-related luminescence. According to Krivobok *et al.* [175], the PL spectra from the ideal GeV^- centers have three peaks in addition to the ZPL at 2.058 eV as follows: (i) the LVM of the GeV^- center at 2.013 eV (the details described in Section 1); (ii) longitudinal acoustic (LA) or transverse acoustic (TA) phonon mode of the diamond lattice coupling with the GeV^- center at 1.933 eV; (iii) longitudinal optical (LO) or transverse optical (TO) phonon mode of the diamond lattice coupling with the GeV^- center at 1.903 eV [176]. In the case of the GeV^- centers in DNDs, these phonon mode peaks could be separated and observed in the spectra as an ensemble peak at 1.98 eV because of the particle size effect and its inhomogeneity derived from the detonation process.

6.3.3.7 Photostability

The photostability of the GeV^- centers in DNDs was evaluated according to the method of Reineck *et al.* [159], as same as one of the SiV^- centers in DNDs described in Section 3.2.6. The evaluation results are shown in Figure 6.21. The GeV^- centers in DNDs exhibit stable luminescence with no bleaching as well as CNTs, NV centers in NDs, and the SiV^- centers in DNDs.

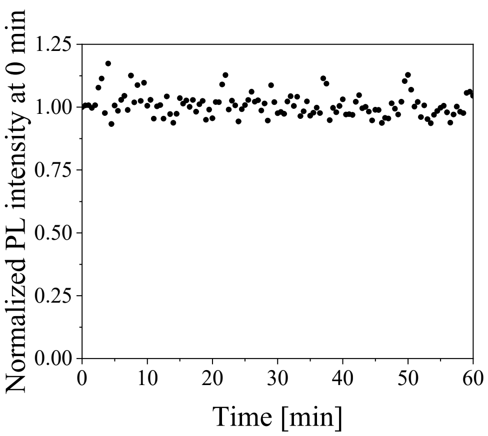

Figure 6.21 – Luminescence intensity for ZPL of GeV⁻ centers in DNDs, recorded at 15 s intervals. The ZPL intensity was counted after its baseline removals and was normalized by initial intensity at 0 min.

6.4. Summary

The optical properties of the SiV⁻ and GeV⁻ centers in DNDs of ~10 nm on average were evaluated systematically. They exhibited greater linewidths, smaller DWFs, and shorter luminescence lifetimes than those of typical SiV⁻ and GeV⁻ centers in bulk-sized diamonds. Note that the luminescence lifetime of the GeV⁻ centers in DNDs could not be determined. This issue must be solved by single-particle measurements in the future. These characteristic optical properties reflected changes in the electronic states of the SiV⁻ and GeV⁻ centers caused by the particle size effect of the DNDs. The extremely small particle size of DNDs with ~10 nm distorted the split-vacancy structures of each color center and made them more sensitive to surface potentials. As a result, they caused the increase in nonradiative transition probability and the enhancement of electron–phonon coupling on each color center. In addition, the detonation process does not completely control the distance of each color center from the surface in DNDs, which gives variation to the size effect on the color centers. The variation induced the inhomogeneous broadening of their ZPLs.

Chapter 7. Conclusion and future prospects

7.1 Conclusion

In this dissertation, the author demonstrated the industrial-scale synthesis of the G4V-NDs via the detonation process (G4V-DNDs) and revealed the optical properties of the G4V$^-$ centers encapsulated in extremely small DNDs.

The synthesis strategy of the G4V-DNDs was designed as follows: (i) to propose the DND formation mechanism at the molecular level; (ii) to select the dopants as group IV element sources based on the proposed mechanism; (iii) to synthesize the G4V-DNDs by the detonation process using the selected dopants. In Chapter 3, the DND formation mechanism was discussed on the basis of the intermediate species in the detonation reaction. The emission from the mixed-explosive consisting of TNT and RDX (TR-explosive) for the undoped-DND production was observed by time-resolved emission spectroscopy explained in Chapter 2. The measured time-resolved emission spectra showed the peak of the atomic carbon (C_1) emission and no peaks in Swan-band of C_2 which is characteristic of carbon diatomic radicals. The absence of the peaks in Swan-band suggested that the previously proposed the C_2-mechanism, in which radical-like carbons C_2 generated by the decomposition of the explosive molecules serve as the building blocks for the DND formation, was not promising. On the other hand, the observation of the atomic carbons proposed the C_1-mechanism in which C_1 species function as building blocks of DNDs. Second, the MD simulation with ReaxFF of 288 TNT molecules, which play the role of the carbon sources of the DNDs, was carried out under the detonation reaction conditions of 25 GPa and 3675 K. According to this simulation, while the functional groups on TNTs were released as the stable gas, the toluene skeletons of TNTs, including the C_6 aromatic rings, were maintained during the detonation reaction and then polymerized to form the carbon clusters. Hence, the C_6-mechanism was proposed, in which C_6 species function as the building blocks of DNDs. Under the proposed mechanisms, the silicon sources (Si-dopants) were selected for the SiV-DNDs synthesis. TTS was selected for the C_1-mechanism because its structure has abundant Si atoms and can readily release atomic Si during the detonation reactions. The released Si atoms were expected to be in high-frequency contact with the C_1 species derived from TNT molecules and then incorporated into the C_1 condensation process. For the C_6-mechanism, TPSOH was selected owing to its structure with three aromatic rings attached to the Si atom. The aromatic ring interaction between the TPSOH and the C_6 building blocks during the detonation reaction was expected to incorporate the Si atoms into the DND structure. The SiV-DND synthesis using the explosives containing each Si-dopant was performed in Chapter 4. DNDs with an average particle size of 7 nm were produced by both explosives with TTS or TPSOH (TTS- or TPSOH-DNDs, respectively), which were measured by PL spectroscopy to confirm the SiV^- center creation. The SiV^- luminescence was not detected in the PL spectra of the TTS-DNDs. In contrast, the PL spectrum of the TPSOH-DNDs showed a prominent peak at 1.68 eV corresponding to the ZPL of the SiV^- center. Hence, The SiV-DND synthesis was achieved by the explosive with TPSOH as the Si-dopant. Subsequently, the time-resolved emission measurements of the detonation reaction from each explosive were performed to investigate the reason for the successful synthesis. Because the time-resolved emission spectrum of the TTS-containing explosive exhibited atomic emission of Si, TTS was decomposed to atomic Si during the detonation reaction following the Si-dopant selection strategy corresponding to the C_1-mechanism. Nevertheless, the SiV-DNDs were not produced by the explosive containing TTS. These results suggested the non-intervention of atomic Si in the C_1 condensing process and the invalidity of the C_1-mechanism. On the other hand, TPSOH maintained its chemical structure in whole or in part during the detonation reaction because of the absence of Si atomic emission in the time-resolved spectrum of the detonation emission from the explosive with TPSOH. Therefore, the achievement of the SiV-DNDs synthesis was explained by the aromatic–aromatic interactions between TPSOH and C_6 diamond building blocks derived from TNTs as the DND carbon source. In other words, this study proposed the C_6-mechanism as the DND formation mechanism at the molecular level during the detonation reaction. This detonation process using aromatic organic compounds as heteroatom dopants was extended to the other types G4V-DNDs syntheses in Chapter 5. The resynthesis of SiV-DNDs and syntheses of the GeV- and SnV-DNDs were performed using the explosives containing dopant molecules with each group IV atom centered on tetraphenyl compounds. The direct syntheses of the SiV- and GeV-DNDs were confirmed by the observation of their ZPLs in their PL spectra. However, the SnV-DNDs were not produced in detectable concentrations in PL measurements. To compare the amounts of the SiV- and GeV-DNDs produced, the numbers of data points in the PL-maps, where the spectra show the ZPLs, were counted. The SiV- and GeV-DNDs were observed in 7055 and 1555 data points from the corresponding PL-maps, among a total of 10201 data points, respectively. Therefore, this synthesis process favorably produced the G4V-DNDs composed of elements with smaller atomic numbers. Here, the successes and limitations of G4V-DND direct synthesis by the detonation process were discussed in thermodynamics and kinetics of the detonation reaction involving each dopant. Each detonation reaction is a competing reaction between the doping of group IV atoms into DNDs and generations of group IV dioxides. The thermodynamic equilibrium constant ratios for these two competing reactions were calculated using quantum chemical simulations. The ratios for each detonation reaction with the group IV dopants were consistent with the generated concentrations of the G4V-DNDs. Therefore, the detonation reaction for G4V-DND synthesis was explained from the thermodynamic point of view. Kinetics of the detonation reaction depended on the dopant structures and affected the concentration of G4V-DND formation. However, the kinetic effect was smaller than the thermodynamic effect. As concluded above, these studies in Chapters 3–5 not only demonstrated the practical scale synthesis of the SiV- and GeV-DNDs by the detonation process but also explained the physical chemistry behind the achievements.

The optical properties of the G4V$^-$ centers in DNDs were evaluated in Chapter 6 using the time-resolved spectroscopic measurement and other optical measurements. The samples used in this study were the SiV- and GeV-DND synthesized by the detonation process described in Chapters 4 and 5, with an average particle size of ~10 nm. Firstly, the optical properties of the SiV$^-$ centers in DNDs were compared with those of typical SiV$^-$ centers in bulk-sized diamonds. The SiV$^-$ centers in DNDs exhibited greater homogeneous and inhomogeneous broadening of the ZPL than those for typical SiV$^-$ centers. The broadening of the ZPL absorption band was also observed in the PLE spectrum. Moreover, the DWF and luminescence lifetimes of the SiV$^-$ centers in DNDs were smaller and shorter than those of typical SiV$^-$ centers by ~70% and 50%, respectively. These optical properties indicate the differences in electronic states of the SiV$^-$ centers in DNDs from typical SiV$^-$

centers, namely the enhancement of electron–phonon coupling and the increase in nonradiative transition probability. The possible cause of the differences was the particle size effect of the extremely small DNDs with ~10 nm, which distorted the split-vacancy structures of the SiV⁻ center and made it more sensitive to surface potentials. Moreover, the detonation process did not completely control the distance of each SiV⁻ center from the surface of DNDs. The uncontrolled distance gave variation to the particle size effect, which induced the inhomogeneous broadening of the ZPL. Secondly, the optical properties of the GeV⁻ centers in DNDs were also compared with those of typical GeV⁻ centers in bulk-sized diamonds. As with the SiV⁻ center, the changes in the optical properties were observed compared with those of typical GeV⁻ centers because of the following factors: (i) the particle size effects of DNDs on the GeV⁻ centers leading to enhance the electron–phonon coupling and increase in the nonradiative transition probability; (ii) the induction of inhomogeneity in the particle size effects by the detonation process. However, the photostability of the SiV⁻ and GeV⁻ centers did not change even when the particle size was extremely small. These fundamental optical properties and the understanding of their origin are expected to accelerate the application of the SiV- and GeV-DNDs.

In this dissertation, the detonation reaction was represented as a chemical reaction based on the formation mechanism, thermodynamics, and kinetics. It provides an understanding of the detonation process from a perspective outside of explosives engineering. I believe that this chemical perspective helps in the synthesis of other F-NDs as well as other types of advanced materials using the detonation process. In addition, the optical properties of the G4V⁻ centers in DNDs, the smallest of the NDs, were characterized and discussed in detail regarding the effect of particle size on their electronic structures. The discussion provides a foundational understanding that is lacking not only in the G4V-NDs but also in the other F-NDs. It is expected to contribute to the development of the F-ND community.

7.2 Future prospects

For the social implementation of the G4V-DNDs, three issues remain. Firstly, the optical properties of the SiV^- and GeV^- centers presented in Chapter 6 were average values measured on aggregated SiV- and GeV-DNDs, respectively. The properties of each particle have not yet been determined. Secondly, the G4V-DNDs are mixtures with the undoped-DNDs in an unknown ratio. To answer these two issues, it is necessary to investigate them in more detail using single-particle spectroscopy. Lastly, the ratio must not be high sufficiently in specific applications such as single-photon sources which always require 100% G4V-DND. The most realistic way to enhance the ratio is probably employing an optical manipulation focusing on the light absorption and emission processes that are the critical difference between the G4V-DNDs and undoped-DNDs [177–180].

Despite the abovementioned issues, the day is steadily approaching when the G4V-DNDs will be put to practical use as fluorescent markers and single-photon sources. Their non-bleaching, bright, and sharp ZPLs promise advances in medicine and QIP. Moreover, this dissertation enables the further exploration of science. Combination of the detonation process and the optical characterization with the optical manipulation can provide all types of homogeneous F-NDs of single-digit nanometer size. The F-NDs can be used for fundamental physics research such as atomic physics because they are considered to be atomic-level optical materials that function stably in the ambient environment. Adopting the F-NDs removes the requirements of atomic physics, such as a confinement system with ultrahigh vacuum, and leads researchers to study novel quantum phenomena simply. I conclude this dissertation with the sincere hope that the F-NDs and their detonation synthetic technologies will solve the social problems of our time and future.

References

[1] T.M. Osman, D.E. Rardon, L.B. Friedman, and L.F. Vega, “The commercialization of nanomaterials: today and tomorrow,” JOM **58**, 21–24 (2006).

[2] N. Baig, I. Kammakakam, and W. Falath, “Nanomaterials: a review of synthesis methods, properties, recent progress, and challenges,” Mater. Adv. **2**, 1821–1871 (2021).

[3] W.J. Stark, P.R. Stoessel, W. Wohlleben, and A. Hafner, “Industrial applications of nanoparticles,” Chem. Soc. Rev. **44**, 5793–5805 (2015).

[4] J. Ni, C. Huang, L.-M. Zhou, M. Gu, Q. Song, Y. Kivshar, and C.-W. Qiu, “Multidimensional phase singularities in nanophotonics,” Science **374**, 418 (2021).

[5] S. Surana, A.R. Shenoy, and Y. Krishnan, “Designing DNA nanodevices for compatibility with the immune system of higher organisms,” Nat. Nanotechnol. **10**, 741–747 (2015).

[6] Z.L. Wang and W. Wu, “Nanotechnology-enabled energy harvesting for self-powered micro-/nanosystems,” Angew. Chem. Int. Ed. **51**, 11700–11721 (2012).

[7] J. Zhu, M. Zhu, Q. Shi, F. Wen, L. Liu, B. Dong, A. Haroun, Y. Yang, P. Vachon, X. Guo, T. He, and C. Lee, “Progress in TENG technology—a journey from energy harvesting to nanoenergy and nanosystem” EcoMat **2**, e12058 (2020).

[8] D.F. Emerich and C.G. Thanos, “Nanotechnology and medicine,” Expert Opin. Biol. Ther. **3**, 655–663 (2003).

[9] J. He, C. Li, L. Ding, Y. Huang, X. Yin, J. Zhang, J. Zhang, C. Yao, M. Liang, R.P. Pirraco, J. Chen, Q. Lu, R. Baldridge, and Y. Zhang, “Tumor targeting strategies of smart fluorescent nanoparticles and their applications in cancer diagnosis and treatment,” Adv. Mater. **31**, 1902409 (2019).

[10] M.H. Alkahtani, F. Alghannam, L. Jiang, A. Almethen, A.A. Rampersaud, R. Brick, C.L. Gomes, M.O. Scully, and P.R. Hemmer, “Fluorescent nanodiamonds: past, present, and future,” Nanophotonics **7**, 1423–1453 (2018).

[11] I.L. Medintz, H. Mattoussi, and A.R. Clapp, “Potential clinical applications of quantum dots,” Int. J. Nanomedicine **3**, 151–167 (2008).

[12] W.J. Parak, T. Pellegrino, and C. Plank, “Labelling of cells with quantum dots,” Nanotechnology **16**, R9–R25 (2005).

[13] U. Resch-Genger, M. Grabolle, S. Cvavaliere-Jaricot, R. Nitschke, and T. Nann, "Quantum dots versus organic dyes as fluorescent labels," Nat. Methods **5**, 763–775 (2008).

[14] J.Y. Kim, O. Voznyy, D. Zhitomirsky, and E.H. Sarge, "25th anniversary article: colloidal quantum dot materials and devices: a quarter-century of advances," Adv. Mater. **25**, 4986–5010 (2013).

[15] K. Cottingham "Quantum dots leave the light on," Anal. Chem. **77**, 354 A–357 A (2005).

[16] T. Jamieson, R. Bakhshi, D. Petrova, R. Pocock, M. Imani, and A.M. Seifalian, "Biological applications of quantum dots," Biomaterials **28**, 4717–4732 (2007).

[17] P. Zrazhevskiy and X. Gao, "Multifunctional quantum dots for personalized medicine," Nano Today **4**, 414–428 (2009).

[18] R. Bilan, F. Fleury, I. Nabiev, and A. Sukhanova, "Quantum dot surface chemistry and functionalization for cell targeting and imaging," Bioconjugate Chem. **26**, 609−624 (2015).

[19] AI.L. Efros and M. Rosen, "Random telegraph signal in the photoluminescence intensity of a single quantum dot," Phys. Rev. Lett. **78**, 1110 (1997).

[20] M. Bottrill and M. Green, "Some aspects of quantum dot toxicity," Chem. Commun. **47**, 7039–7050 (2011).

[21] C. Zhu, Z. Chen. S. Gao, B.L. Goh, I.B. Samsudin, K.W. Lwe, Y. Wu, C. Wu, and X. Su, "Recent advances in non-toxic quantum dots and their biomedical applications," Prog. Nat. Sci.: Mater. Int. **29**, 628–640 (2019).

[22] M. Montalti, A. Cantelli, and G. Battistelli, "Nanodiamonds and silicon quantum dots: ultrastable and biocompatible luminescent nanoprobes for long-term bioimaging," Chem. Soc. Rev. **44**, 4853–4921 (2015).

[23] M.D. Torelli, N.A. Nunn, and O.A. Shenderova, "A perspective on fluorescent nanodiamond bioimaging," Small **15**, 1902151 (2019).

[24] A.M. Zaitsev, "Vibronic spectra of impurity-related optical centers in diamond," Phys. Rev. B **61**, 12909 (2000).

[25] I. Aharonovich and E. Neu "Diamond nanophotonics," Adv. Opt. Mater. **2**, 911–928 (2014).

[26] A. Boruah and B.K. Saikia, "Synthesis, characterization, properties, and novel applications of fluorescent nanodiamonds," J. Fluoresc. **32**, 863–885 (2022).

[27] G. Kucsko, P.C. Maurer, N.Y. Yao, M. Kubo, H.J. Noh, P.K. Lo, H. Park, and M.D. Lukin, "Nanometre-scale thermometry in a living cell," Nature **500**, 54–58 (2013).

[28] A. Alfieri, S.B. Anantharaman, H. Zhang, and D. Jariwala, "Nanomaterials for quantum Information science and engineering," Adv. Mater. **35**, 2109621 (2022).

[29] S.A. Iyengar, A.B. Puthirath, and V. Swaminathan, "Realizing quantum technologies in nanomaterials and nanoscience," Adv. Mater. **35**, 2107839 (2023).

[30] L. You, "Superconducting nanowire single-photon detectors for quantum information," Nanophotonics **9**, 2673–2692 (2020).

[31] M.G. Raymer and C. Monroe, "The US national quantum initiative," Quantum Sci. Technol. **4**, 020504 (2019).

[32] E. Gibney, "Quantum gold rush: the private funding pouring into quantum start-ups," Nature **574**, 22–24 (2019).

[33] M. Barbiero, S. Castelletto, X. Gan, and M. Gu, "Spin-manipulated nanoscopy for single nitrogen-vacancy center localizations in nanodiamonds," Light Sci. Appl. **6**, e17085 (2017).

[34] R. Löfgren, S. Öberg, and J.A. Larssona, "The diamond NV-center transition energies in the vicinity of an intrinsic stacking fault," AIP Adv. **12**, 035009 (2022).

[35] A. Alkauskas, B.B. Buckley, D.D. Awschalom, and C.G. van de Walle, "First-principles theory of the luminescence lineshape for the triplet transition in diamond NV centres," New J. Phys. **16**, 073026 (2014).

[36] Á. Gali, "*Ab initio* theory of the nitrogen-vacancy center in diamond," Nanophotonics **8**, 1907–1943 (2019).

[37] M. Fox, "Optical properties of solids (1st ed.)," Oxford University Press, New York (2001) pp. 173–176, 186–191.

[38] S.E. Schwartz, "The Franck-Condon principle and the duration of electronic transitions," J. Chem. Educ. **50**, 608–610 (1973).

[39] J. Walker, "Optical absorption and luminescence in diamond," Rep. Prog. Phys. **42**, 1605 (1979).

[40] M.N. Sapozhnikov, "Zero-phonon transitions in the optical spectra of impurity molecular crystals," Phys. Status Solidi B **75**, 11–51 (1976).

[41] K. Sakoda, J. Kawamata, K. Onoue, and M. Maeda, "Photochemical hole burning and Debye-Waller factor in polyvinylalcohol doped with mesoporphyrin," Chem. Phys. Lett. **231**, 171–176 (1994).

[42] G. Balasubramanian, A. Lazariev, S.R. Arumugam, and D.-W. Duan, “Nitrogen-vacancy color center in diamond—emerging nanoscale applications in bioimaging and biosensing,” Curr. Opin. Chem. Biol. **20**, 69–77 (2014).

[43] M.W. Doherty, N.B. Mansonb, P. Delaney, F. Jelezko, J. Wrachtrupe, and L.C.L. Hollenberg, “The nitrogen-vacancy colour centre in diamond,” Phys. Rep. **528**, 1–45 (2013).

[44] R. Schirhagl, K. Chang, M. Loretz, and C.L. Degen, “Nitrogen-vacancy centers in diamond: nanoscale sensors for physics and biology,” Annu. Rev. Phys. Chem. **65**, 83–105 (2014).

[45] A. Lenef and S.C. Rand, “Electronic structure of the N-V center in diamond: theory,” Phys. Rev. B **53**, 13441–13455 (1996).

[46] A. Batalov, V. Jacques, F. Kaiser, P. Siyushev, P. Neumann, L.J. Rogers, R.L. McMurtrie, N.B. Manson, F. Jelezko, and J. Wrachtrup, “Low temperature studies of the excited-state structure of negatively charged nitrogen-vacancy color centers in diamond,” Phys. Rev. Lett. **102**, 195506 (2009).

[47] I. Aharonovich, A. D. Greentree, and S. Prawer, “Diamond photonics,” Nat. Photonics **5**, 397–405 (2011).

[48] P.L. Stanwix, L.M. Pham, J.R. Maze, D.L. Sage, T.K. Yeung, P. Cappellaro, P.R. Hemmer, A. Yacoby, M.D. Lukin, and R.L. Walsworth, “Coherence of nitrogen-vacancy electronic spin ensembles in diamond,” Phys. Rev. B **82**, 201201(R) (2010).

[49] L. Childress and R. Hanson, “Diamond NV centers for quantum computing and quantum networks,” MRS Bulletin **38**, 134–138 (2013).

[50] B. Rodiek, M. Lopez, H. Hofer, G. Porrovecchio, M. Smid, X.-L. Chu, S. Gotzinger, V. Sandoghdar, S. Lindner, C. Becher, and S. Kuck, “Experimental realization of an absolute single-photon source based on a single nitrogen vacancy center in a nanodiamond,” Optica **4**, 71–76 (2017).

[51] L.J. Rogers, K.D. Jahnke, M.W. Dohetry, A. Dietrich, L.P. McGuinness, C. Müller, T. Teraji, H. Sumiya, J. Isoya, N.B. Manson, and F. Jelezko, “Electronic structure of the negatively charged silicon-vacancy center in diamond,” Phys. Rev. B **89**, 235101 (2014).

[52] C. Bradac, W. Gao, J. Forneris, M. E. Trusheim, and I. Aharonovich, “Quantum nanophotonics with group IV defects in diamond,” Nat. Commun. **10**, 5625 (2019).

[53] M. Zaghrioui, V.N. Agafonov, and V.A. Davydov, “Nitrogen and group-IV (Si, Ge) vacancy color centres in nanodiamonds: photoluminescence study at high temperature (25 °C–600 °C),” Mater. Res. Express **7**, 015043 (2020).

[54] C. Qiu, H.-X. Deng, S.G., and S.-H. Wei, "Origin of structure and zero-phonon-line anomalies of *X*V centers in diamond (*X*=Si, Ge, Sn, Pb)," Phys. Rev. B **107**, 214110 (2023).

[55] J.P. Goss, R. Jones, S.J. Breuer, P.R. Briddon, and S. Öberg, "The twelve-line 1.682 eV luminescence center in diamond and the vacancy-silicon complex," Phys. Rev. Lett. **77**, 3041–3044 (199146).

[56] J.P. Goss, P.R. Briddon, M.J. Rayson, S.J. Sque, and R. Jones, "Vacancy-impurity complexes and limitations for implantation doping of diamond," Phys. Rev. B **72**, 035214 (2005).

[57] U. Wahl, J.G. Correia, R. Villarreal, E. Bourgeois, M. Gulka, M. Nesládek, A. Vantomme, and L.M.C. Pereira, "Direct structural identification and quantification of the split-vacancy configuration for implanted Sn in diamond," Phys. Rev. Lett. **125**, 045301 (2020).

[58] A. Sipahigil, K.D. Jahnke, L.J. Rogers, T. Teraji, J. Isoya, A.S. Zibrov, F. Jelezko, and M.D. Lukin, "Indistinguishable photons from separated silicon-vacancy centers in diamond," Phys. Rev. Lett. **113**, 113602 (2014).

[59] K.D. Jahnke, A. Sipahigil, J.M. Binder, M.W. Doherty, M. Metsch, L.J. Rogers, N.B. Manson, M.D. Lukin, and F. Jelezko, "Electron–phonon processes of the silicon-vacancy centre in diamond," New J. Phys. **17**, 043011 (2015).

[60] A. Liu and S.T. Cundiff, "Spectroscopic signatures of electron–phonon coupling in silicon-vacancy centers in diamond," Phys. Rev. Mater. **4**, 055202 (2020).

[61] C.T. Nguyen, R.E. Evans, A. Sipahigil, M.K. Bhaskar, D.D. Sukachev, V.N. Agafonov, V.A. Davydov, L.F. Kulikova, F. Jelezko, and M.D. Lukin, "All-optical nanoscale thermometry with silicon-vacancy centers in diamond," Appl. Phys. Lett. **112**, 203102 (2018).

[62] J.-W. Fan, I. Cojocaru, J. Becker, I.V. Fedotov, M.H.A. Alkahtani, A. Alajlan, S. Blakley, M. Rezaee, A. Lyamkina, Y.N. Palyanov, Y.M. Borzdov, Y.-P. Yang, A. Zheltikov, P. Hemmer, and A.V. Akimov, "Germanium-vacancy color center in diamond as a temperature sensor," ACS Photonics **5**, 765–770 (2018).

[63] M. Alkahtani, I. Cojocaru, X. Liu, T. Herzig, J. Meijer, J. Küpper, T. Lühmann, A. V. Akimov, and P. R. Hemmer, "Tin-vacancy in diamonds for luminescent thermometry," Appl. Phys. Lett. **112**, 241902 (2018).

[64] M. Ruf, N.H. Wan, H. Choi, D. Englund, and R. Hanson, "Quantum networks based on color centers in diamond," J. Appl. Phys. **130**, 070901 (2021).

[65] S. Häuβler, G. Thiering, A. Dietrich, N. Waasem, T. Teraji, J. Isoya, T. Iwasaki, M. Hatano, F. Jelezko, A. Gali, and A. Kubanek, "Photoluminescence excitation

spectroscopy of SiV⁻ and GeV⁻ color center in diamond," New J. Phys. **19**, 063036 (2017).

[66] U.F.S. D'Haenens-Johansson, J.E. Butler, and A.N. Katrusha, "Synthesis of diamonds and their identification," Rev. Mineral. Geochem. **88**, 689–754 (2022).

[67] O.A. Shenderova, A.I. Shames, N.A. Nunn, M.D. Torelli, I. Vlasov, and A. Zaitsev, "Review article: synthesis, properties, and applications of fluorescent diamond particles," J. Vac. Sci. Technol. B **37**, 030802 (2019).

[68] G. Sittas, H. Kanda, I. Kiflawi, and P. M. Spear, "Growth and characterization of Si-doped diamond single crystals grown by the HTHP method," Diam. Relat. Mater. **5**, 866–869 (1996).

[69] E.A. Ekimov, M.V. Kondrin, V.S. Krivobok, A.A. Khomich, I.I. Vlasov, R.A. Khmelntiskiy, T. Iwasaki, and M. Hatano, "Effect of Si, Ge and Sn dopant elements on structure and photoluminescence of nano- and microdiamonds synthesized from organic compounds," Diam. Relat. Mater. **93**, 75–83 (2019).

[70] S.V. Bolshedvorskii, A.I. Zeleneev, V.V. Vorobyov, V.V. Soshenko, O.R. Rubinas, L.A. Zhulikov, P.A. Pivovarov, V.N. Sorokin, A.N. Smolyaninov, L.F. Kulikova, A.S. Garanina, S. G. Lyapin, V.N. Agafonov, R.E. Uzbekov, V.A. Davydov, and Alexey V. Akimov, "Single silicon vacancy centers in 10 nm diamonds for quantum information applications," ACS Appl. Nano Mater. **2**, 4765–4772 (2019).

[71] P.L. Diggle, U.F.S. D'Haenens-Johansson, B.L. Green, C.M. Welbourn, T.N.T. Thi, A. Katrusha, W. Wang, and M.E. Newton, "Decoration of growth sector boundaries with nitrogen vacancy centers in as-grown single crystal high-pressure high-temperature synthetic diamond," Phys. Rev. Mater. **4**, 093402 (2020).

[72] F.G. Celii and J.E. Butler, "Diamond chemical vapor deposition," Annu. Rev. Phys. Chem. **42**, 643–684 (1991).

[73] M. Schwander and K. Partes, "A review of diamond synthesis by CVD processes," Diam. Relat. Mater. **20**, 1287–1301 (2011).

[74] J.-C. Arnault, S. Saada, and V. Ralchenko, "Chemical vapor deposition single-crystal diamond: a review," Phys. Status Solidi Rapid Res. Lett. **16**, 2100354 (2022).

[75] T. Zhang, M. Gupta, J. Jing, Z. Wang, X. Guo, Y. Zhu, Y. C. Yiu, T.K.C. Hui, Q. Wang, K.H. Li, and Z. Chu, "High-quality diamond microparticles containing SiV centers grown by chemical vapor deposition with preselected seeds," J. Mater. Chem. C **10**, 13734–13740 (2022).

[76] E. Neu, C. Arend, E. Gross, F. Guldner, C. Hepp, D. Steinmetz, E. Zscherpel, S. Ghodbane, H. Sternschulte, D. Steinmüller-Nethl, Y. Liang, A. Krueger, and C. Becher, "Narrowband fluorescent nanodiamonds produced from chemical vapor deposition films," **98**, 243107 (2011).

[77] A. Bolshakov, V. Ralchenko, V. Sedov, A. Khomich, I. Vlasov, A. Khomich, N. Trofimov, V. Krivobok, S. Nikolaev, R. Khmelnitskii, and V. Saraykin, "Photoluminescence of SiV centers in single crystal CVD diamond *in situ* doped with Si from silane," Phys. Status Solidi A **212**, 2525–2532 (2015).

[78] V. Sedov, A. Martyanov, S. Savin, A. Bolshakov, E. Bushuev, A. Khomich, O. Kudryavtsev, V. Krivobok, S. Nikolaev, and V. Ralchenko, "Growth of polycrystalline and single-crystal CVD diamonds with bright photoluminescence of Ge-V color centers using germane GeH_4 as the dopant source," Diam. Relat. Mater. **90**, 47–53 (2018).

[79] A.M. Romshin, V. Zeeb, A.K. Martyanov, O.S. Kudryavtsev, D.G. Pasternak, V.S. Sedov, V.G. Ralchenko, A.G. Sinogeykin, and I.I. Vlasov, "A new approach to precise mapping of local temperature fields in submicrometer aqueous volumes," Sci. Rep. **11**, 14228 (2021).

[80] M.T. Westerhausen, A.T. Trycz, C. Stewart, M. Nonahal, B. Regan, M. Kianinia, and I. Aharonovich, "Controlled doping of GeV and SnV color centers in diamond using chemical vapor deposition," ACS Appl. Mater. Interfaces **12**, 29700–29705 (2020).

[81] T. Schröder, M. Walsh, J. Zheng, S. Mouradian, L. Li, G. Malladi, H. Bakhru, M. Lu, A. Stein, M. Heuck, and D. Englund, "Scalable fabrication of coupled NV center - photonic crystal cavity systems by self-aligned N ion implantation," Opt. Mater. Express **7**, 1514–1524 (2017).

[82] C. Wang, C. Kurtsiefer, H. Weinfurter, and B. Burchard, "Single photon emission from SiV centres in diamond produced by ion implantation," J. Phys. B: At. Mol. Opt. Phys. **39**, 37–41 (2006).

[83] T. Iwasaki, F. Ishibashi, Y. Miyamoto, Y. Doi, S. Kobayashi, T. Miyazaki, K. Tahara, K.D. Jahnke, L.J. Rogers, B. Naydenov, F. Jelezko, S. Yamasaki, S. Nagamachi, T. Inubushi, N. Mizuochi, and M. Hatano, "Germanium-vacancy single color centers in diamond," Sci. Rep. **5**, 12882 (2015).

[84] S.D. Tchernij, T. Herzig, J. Forneris, J. Küpper, S. Pezzagna, P. Traina, E. Moreva, I.P. Degiovanni, G. Brida, N. Skukan, M. Genovese, M. Jakšić, J. Meijer, and P. Olivero, "Single-photon-emitting optical centers in diamond fabricated upon Sn implantation," ACS Photonics **4**, 2580–2586 (2017).

[85] T.D. Merson, S. Castelletto, I. Aharonovich, A. Turbic, T.J. Kilpatrick, and A.M. Turnley, "Nanodiamonds with silicon vacancy defects for nontoxic photostable fluorescent labeling of neural precursor cells," Opt. Lett. **38**, 4170–4173 (2013).

[86] X. Xu, Z.O. Martin, M. Titze, Y. Wang, D. Sychev, J. Henshaw, A.S. Lagutchev, H. Htoon, E.S. Bielejec, S.I. Bogdanov, V.M. Shalaev, and A. Boltasseva "Fabrication of single color centers in sub-50 nm nanodiamonds using ion implantation," Nanophotonics **12**, 485–494 (2023).

[87] P. Wang, T. Taniguchi, Y. Miyamoto, M. Hatano, and T. Iwasaki, "Low-temperature spectroscopic investigation of lead-vacancy centers in diamond fabricated by high-pressure and high-temperature treatment," ACS Photonics **8**, 2947–2954 (2021).

[88] V. Pichot, O. Stephan, M. Comet, E. Fousson, J. Mory, K. March, and D. Spitzer, "High nitrogen doping of detonation nanodiamonds," J. Phys. Chem. C **114**, 10082–10087 (2010).

[89] D. Terada, T.F. Segawa, A.I. Shames, S. Onoda, T. Ohshima, E. Ōsawa, R. Igarashi, and M. Shirakawa, "Monodisperse five-nanometer-sized detonation nanodiamonds enriched in nitrogen-vacancy centers," ACS Nano **13**, 6461–6468 (2019).

[90] J.-C. Arnault, "Nanodiamonds: advanced material analysis, properties and applications (1st ed.)," Elsevier, Amsterdam (2017) pp. 166–172.

[91] V.N. Mochalin, O. Shenderova, D. Ho, and Y. Gogotsi, "The properties and applications of nanodiamonds," Nat. Nanotechnol. **7**, 11–23 (2012).

[92] V.V. Danilenko, "Nanodiamond: problems and prospects," J. Superhard Mater. **32**, 301–310 (2010).

[93] N. Nunn, M. Torelli, G. McGuire, and O. Shenderova, "Nanodiamond: a high impact nanomaterial," Curr. Opin. Solid. State. Mater. Sci. **21**, 1–9 (2017).

[94] S. Zhang, S. Yao, M. Luan, L. Zhang, and J. Wang, "Effects of injection conditions on the stability of rotating detonation waves," Shock Waves **28**, 1079–1087 (2018).

[95] S.H. Lin and H. Eyring, "Detonation," Annu. Rev. Phys. Chem. **21**, 225–264 (1970).

[96] Z. Wang, Y. Qi, H. Liu, P. Zhang, X. He, and J. Wang, "Shock wave reflection induced detonation (SWRID) under high pressure and temperature condition in closed cylinder," Shock Waves **26**, 687–691 (2016).

[97] A.N. Dremin, "Discoveries in detonation of molecular condensed explosives in the 20th century," Combust. Explos. Shock Waves **36**, 704–715 (2000).

[98] D. Guo, S.V. Zybin, Q. An, W.A. G.oddard III, and F. Huang, "Prediction of the Chapman–Jouguet chemical equilibrium state in a detonation wave from first

principles based reactive molecular dynamics," Phys. Chem. Chem. Phys. **18**, 2015–2022 (2016).

[99] V.V. Danilenko, "On the history of the discovery of nanodiamond synthesis," Phys. Solid Stat. **46**, 595–599 (2004).

[100] J.A. Viecelli, S. Bastea, J.N. Glosli, and F.H. Ree, "Phase transformations of nanometer size carbon particles in shocked hydrocarbons and explosives," J. Chem. Phys. **115**, 2730–2736 (2001).

[101] J. Görlitz, D. Herrmann, G. Thiering, P. Fuchs, M. Gandil, T. Iwasaki, T. Taniguchi, M. Kieschnick, J. Meijer, M. Hatano, A. Gali, and C. Becher, "Spectroscopic investigations of negatively charged tin-vacancy centres in diamond," New J. Phys. **22**, 013048 (2020).

[102] Hamamatsu Photonics (2008). "Guide to streak cameras," [Online]. Available: https://www.hamamatsu.com/content/dam/hamamatsu-photonics/sites/documents/99_SALES_LIBRARY/sys/SHSS0006E_STREAK.pdf

[103] W. Zhang, D. Zhu, Y. Sui, H. Ma, J. Yue, and J. Gao, "Streak camera calibration for bunch length measurement at BEPC II," Radiat. Detect. Technol. Methods. **5**, 466–473 (2021).

[104] J. Saarela, M. Törmänen, and R. Myllylä, "Measuring pulp consistency and fines content with a streak camera," Meas. Sci. Technol. **14**, 1801–1806 (2003).

[105] V.Y. Dolmatov, "On the mechanism of detonation nanodiamond synthesis," J. Superhard Mater. **30**, 233–240 (2008).

[106] V.Y. Dolmatov, V. Myllymäki, and A. Vehanen, "A possible mechanism of nanodiamond formation during detonation synthesis," J. Superhard Mater. **35**, 143–150 (2013).

[107] S. Tanaka, I. Bataev, M. Nishi, I. Balagansky, and K. Hokamoto, "Micropunching large-area metal sheets using underwater shock wave: experimental study and numerical simulation," Int. J. Mach. Tools Manuf. **147**, 103457 (2019).

[108] T.P Senftle, S. Hong, M.M. Islam, S.B. Kylasa, Y. Zheng, Y.K. Shin, C. Junkermeier, R. Engel-Herbert, M.J. Janik, H.M. Aktulga, T. Verstraelen, A. Grama, and A.C.T. van Duin, "The ReaxFF reactive force-field: development, applications and future directions," npj Comput. Mater. **2**,15011 (2016).

[109] A.C.T. van Duin, S. Dasgupta, F. Lorant, and W.A. Goddard III, "ReaxFF: a reactive force field for hydrocarbons," J. Phys. Chem. A **105**, 9396–9409 (2001).

[110] K. Chenoweth, A.C.T. van Duin, and W.A. Goddard III, "ReaxFF reactive force field for molecular dynamics simulations of hydrocarbon oxidation," J. Phys. Chem. A **112**, 1040–1053 (2008).

[111] S. Bhoi, T. Banerjee, and K. Mohanty, "Molecular dynamic simulation of spontaneous combustion and pyrolysis of brown coal using ReaxFF," Fuel **136**, 326–333 (2014).

[112] L. Liu, Y. Liu, S.V. Zybin, H. Sun, and W.A. Goddard III, "ReaxFF-lg: correction of the ReaxFF reactive force field for London dispersion, with applications to the equations of state for energetic materials," J. Phys. Chem. A **115**, 11016–11022 (2011).

[113] L. Zhang, S.V. Zybin, A.C.T. van Duin, S. Dasgupta, and W.A. Goddard III, "Carbon cluster formation during thermal decomposition of octahydro-1,3,5,7-tetranitro-1,3,5,7-tetrazocine and 1,3,5-triamino-2,4,6-trinitrobenzene high explosives from ReaxFF reactive molecular dynamics simulations," J. Phys. Chem. A **113**, 10619–10640 (2009).

[114] D. Furman, R. Kosloff, F. Dubnikova, S.V. Zybin, W.A. Goddard III, N. Rom, B. Hirshberg, and Y. Zeir, "Decomposition of condensed phase energetic materials: interplay between uni- and bimolecular mechanisms," J. Am. Chem. Soc. **136**, 4192–4200 (2014).

[115] N. Rom, B. Hirshberg, Y. Zeiri, D. Furman, S. V. Zybin, W. A. Goddard III, and R. Kosloff, "First-principles-based reaction kinetics for decomposition of hot, dense liquid TNT from ReaxFF multiscale reactive dynamics simulations," J. Phys. Chem. C **117**, 21043–21054 (2013).

[116] N.P. Satonkina and D.A. Medvedev, "On the mechanism of carbon nanostructures formation at reaction of organic compounds at high pressure and temperature," AIP Adv. **7**, 085101 (2017).

[117] A.G. Gaydon, "The spectroscopy of flame (2nd ed.)," Chapman and Hall, London, (1974) pp. 146–147, 343.

[118] J.E.M. Goldsmith, D.T.B. Kearsley, "C_2 creation, emission, and laser-induced fluorescence in flames and cold gases," App. Phys. B, **50**, 371–379 (1990).

[119] D. Amans, A.-C. Chenu, G. Ledoux, C. Dujardin, C. Reynaud, O. Sublemontier, K. Masenelli-Varlot, O. Guillois, "Nanodiamond synthesis by pulsed laser ablation in liquids," Diam. Relat. Mater. **18**, 177–180 (2009).

[120] A. Kramida, Y. Ralchenko, and J. Reader, NIST ASD Team (2019). NIST atomic spectra database (version 5.7.1), [Online]. Available: https://physics.nist.gov/asd [Tue Mar 31 2020]. National Institute of Standards and Technology, Gaithersburg, MD. DOI: 10.18434/T4W30F.

[121] A. Corney, "Atomic and laser spectroscopy," Oxford University Press., London, (1979) pp. 229–250.

[122] A.Y. Chang, M.D. Dirosa, and R.K. Hanson, "Temperature dependence of collision broadening and shift in the NO A ← X (0,0) band in the pressure of argon and nitrogen," J. Quant. Spectrosc. Radiat. Transfer. **47**, 375–390 (1992).

[123] M. Miclea, K. Kunze, U. Heitmann, S. Florek, J. Franzke, and K. Niemax, "Diagnostics and application of the microhollow cathode discharge as an analytical plasma," J. Phys. D: Appl. Phys. **38**, 1709–1715 (2005).

[124] K. Kurosawa and S. Sugita, "A pressure measurement method for high-temperature rock vapor," J. Geophys. Res. **115**, E10003 (2010).

[125] N. Ohno, M. A. Razzak, H. Ukai, S. Takamura, and Y. Uesugi, "Validity of electron temperature measurement by using Boltzmann plot method in radio frequency inductive discharge in the atmospheric pressure range," Plasma Fusion Res. **1**, 028 (2006).

[126] M. Ishikawa, J. Iyoda, H. Ikeda, K. Kotake, T. Hashimoto, and M. Kumada, "Aluminum chloride catalyzed skeletal rearrangement of permethylated acyclic polysilanes," J. Am. Chem. Soc. **103**, 4845–4850 (1981).

[127] A.G. Brook and S. Wolfe, "The reaction of triphenylsilylpotassium with organic halides, a case of halogen-metal interconversion," J. Am. Chem. Soc. **79**, 1431–1437 (1957).

[128] R. Weissleder, "A clearer vision for *in vivo* imaging," Nat. Biotechnol. **19**, 316–317 (2001).

[129] R. Weissleder and V. Ntziachristos, "Shedding light onto live molecular targets," Nat. Med. **9**, 123–128 (2003).

[130] W. Liu, M.N.A. Alam, Y. Liu, V.N. Agafonov, H. Qi, K. Koynov, V.A. Davydov, R. Uzbekov, U. Kaiser, T. Lasser, F. Jelezko, A. Ermakova, and T. Weil, "Silicon-vacancy nanodiamonds as high performance near-infrared emitters for live-cell dual-color imaging and thermometry," Nano Lett. **22**, 2881–2888 (2022).

[131] L. Schmidlin, V. Pichot, M. Comet, S. Josset, P. Rabu, and D. Spitzer, "Identification, quantification and modification of detonation nanodiamond functional groups," Diam. Relat. Mater. **22**, 113–117 (2012).

[132] T. Yoshikawa, M. Liu, S.L.Y. Chang, I.C. Kuschnerus, Y. Makino, A. Tsurui, T. Mahiko, and M. Nishikawa, "Steric interaction of polyglycerol-functionalized detonation nanodiamonds," Langmuir **38**, 661–669 (2022).

[133] M. Nishikawa, H.G. Kang, Y. Zou, H. Takeuchi, N. Matsuno, M. Suzuki, and N. Komatsu, "Conjugation of phenylboronic acid moiety through multistep

organic transformations on nanodiamond surface for an anticancer nanodrug for boron neutron capture therapy," Bull. Chem. Soc. Jpn. **94**, 2302–2312 (2021).

[134] Y.L. Hsin, H.-Y. Chu, Y.-R Jeng, Y.-H. Huang, M.H. Wang, and C.K. Chang, "*In situ* de-agglomeration and surface functionalization of detonation nanodiamond, with the polymer used as an additive in lubricant oil," J. Mater. Chem. **21**, 13213–13222 (2011).

[135] S. Stehlik, M.Varga, M. Ledinsky, D. Miliaieva, H. Kozak, V. Skakalova, C. Mangler, T.J. Pennycook, J.C. Meyer, A. Kromka, and B. Rezek, "High-yield fabrication and properties of 1.4 nm nanodiamonds with narrow size distribution," Sci. Rep. **6**, 38419 (2016).

[136] R.E. Evans, A. Sipahigil, D.D. Sukachev, A.S. Zibrov, and M.D. Lukin, "Narrow-linewidth homogeneous optical emitters in diamond nanostructures via silicon ion implantation," Phys. Rev. Applied. **5**, 044010 (2016).

[137] K. Shimazaki, H. Kawaguchi, H. Takashima, T.F. Segawa, F.T.-K. So, D. Terada, S. Onoda, T. Ohshima, M. Shirakawa, and S. Takeuchi "Fabrication of detonation nanodiamonds containing silicon-vacancy color centers by high temperature annealing," Phys. Status Solidi A **218**, 2100144 (2021).

[138] R.M. Pashley and M. E. Karaman, "Applied colloid and surface chemistry," John Wiley & Sons, New York (2004), pp. 1–6.

[139] H. Gilman and E.A. Zuech, "Selective reactions of the silicon-hydrogen group with Grignard reagents. The preparation of some unsymmetrical silane derivatives," J. Am. Chem. Soc. **81**, 5925–5928 (1959).

[140] G. Cerveau, C. Chuit, R.J.P. Corriu, and C. Reyé, "Reactivity of dianionic hexacoordinate germanium complexes toward organometallic reagents. A new route to organogermanes," Organometallics **10,** 1510–1515 (1991).

[141] J.J. Eisch and J.E. Galle, "Organosilicon compounds with functional groups proximate to silicon: XVII. synthetic and mechanistic aspects of the lithiation of α,β-epoxyalkylsilanes and related α-heterosubstituted epoxides," J. Organomet. Chem. **341**, 293–313 (1998).

[142] H. Goto and E. Ōsawa, "An efficient algorithm for searching low-energy conformers of cyclic and acyclic molecules," J. Chem. Soc. Perkin Trans. **2,** 187–198 (1993).

[143] SCIGRESS 2.3, Fujitsu Ltd., Tokyo, Japan, 2009.

[144] M. J. Frisch, G. W. Trucks, H.B. Schlegel, G.E. Scuseria, M.A. Robb, J.R. Cheeseman, G. Scalmani, V. Barone, G.A. Petersson, H. Nakatsuji, X. Li, M. Caricato, A.V. Marenich, J. Bloino, B.G. Janesko, R. Gomperts, B. Mennucci, H.P. Hratchian, J.V. Ortiz, A.F. Izmaylov, J.L. Sonnenberg, D. Williams-Young,

F. Ding, F. Lipparini, F. Egidi, J. Goings, B. Peng, A. Petrone, T. Henderson, D. Ranasinghe, V.G. Zakrzewski, J. Gao, N. Rega, G. Zheng, W. Liang, M. Hada, M. Ehara, K. Toyota, R. Fukuda, J. Hasegawa, M. Ishida, T. Nakajima, Y. Honda, O. Kitao, H. Nakai, T. Vreven, K. Throssell, J.A. Montgomery Jr., J.E. Peralta, F. Ogliaro, M.J. Bearpark, J.J. Heyd, E.N. Brothers, K.N. Kudin, V.N. Staroverov, T.A. Keith, R. Kobayashi, J. Normand, K. Raghavachari, A.P. Rendell, J.C. Burant, S.S. Iyengar, J. Tomasi, M. Cossi, J.M. Millam, M. Klene, C. Adamo, R. Cammi, J. W. Ochterski, R.L. Martin, K. Morokuma, O. Farkas, J.B.Foresman, and D.J. Fox, Gaussian 16, Revision A.03. Gaussian, Inc., Wallingford CT (2016).

[145] V.Y. Dolmatov, "Detonation-synthesis nanodiamonds: synthesis, structure, properties and applications," Russ. Chem. Rev. **76**, 339 (2007).

[146] C. Hepp, T. Müller, V. Waselowski, J.N. Becker, B. Pingault, H. Sternschulte, D. Steinmüller-Nethl, A. Gali, J.R. Maze, M. Atatüre, and C. Becher, "Electronic structure of the silicon vacancy color center in diamond," Phys. Rev. Lett. **112**, 036405 (2014).

[147] T. Iwasaki, Y. Miyamoto, T. Taniguchi, P. Siyushev, M.H. Metsch, F. Jelezko, and M. Hatano, "Tin-vacancy quantum emitters in diamond," Phys. Rev. Lett. **119**, 253601 (2017).

[148] G. Thiering and A. Gali, "The (eg ⊗ eu) ⊗ Eg product Jahn-Teller effect in the neutral group-IV vacancy quantum bits in diamond," NPJ Comput. Mater. **5**, 18 (2019).

[149] A. Gali and J.R. Maze, "*Ab initio* study of the split silicon-vacancy defect in diamond: Electronic structure and related properties," Phys. Rev. B **88**, 235205 (2013).

[150] D.A. McQuarrie and J.D. Simon, "Molecular thermodynamics," University Science Books, Sausalito, CA (1999) pp. 281–283.

[151] Z. Slanina, S.-L. Lee, F. Uhlík, L. Adamowicz, and S. Nagase, "Computing relative stabilities of metallofullerenes by Gibbs energy treatments," Theor. Chem. Acc. **117**, 315–322 (2007).

[152] R. Bleil, F.-M. Tao, and S. Kais, "Structure and stability of C_{13} carbon clusters," Chem. Phys. Lett. **229**, 491–494 (1994).

[153] S. Dhara, N.L. Misra, S.K. Aggarwal, D. Ingerle, P. Wobrauschek, and C. Streli, "Determinations of low atomic number elements in real uranium oxide samples using vacuum chamber total reflection x-ray fluorescence," X-ray Spectrom. **43**, 108–111 (2014).

[154] O.A. Shenderova, I.I. Vlasov, S. Turner, G.V. Tendeloo, S.B. Orlinskii, A.A. Shiryaev, A.A. Khomich, S.N. Sulyanov, F. Jelezko, and J. Wrachtrup,

"Nitrogen control in nanodiamond produced by detonation shock-wave-assisted synthesis," J. Phys. Chem. C **115**, 14014–14024 (2011).

[155] D.P. Mitev, A.T. Townsend, B. Paull, and P.N. Nesterenko, "Microwave-assisted purification of detonation nanodiamond," Diam. Relat. Mater. **48**, 37–46 (2014).

[156] D. Quane, "Bond energy terms for methylsilanes and methylchlorosilanes," J. Phys. Chem. **75**, 2480–2483 (1971).

[157] E.A. Ekimov, P.S. Sherin, V.S. Krivobok, S.G. Lyapin, V.A. Gavva, and M.V. Kondrin, "Photoluminescence excitation study of split-vacancy centers in diamond," Phys. Rev. B **97**, 045206 (2018).

[158] J.N. Becker and C. Becher, "Coherence properties and quantum control of silicon vacancy color centers in diamond," Phys. Status Solidi A **214**, 1700586 (2017).

[159] P. Reineck, A. Francis, A. Orth, D.W.M. Lau, R.D.V. Nixon-Luke, I.D. Rastogi, W. A. W. Razali, N.M. Cordina, L.M. Parker, V.K.A. Sreenivasan, L.J. Brown, and B. C. Gibson, "Brightness and photostability of emerging red and near-IR fluorescent nanomaterials for bioimaging," Adv. Opt. Mater. **4**, 1549–1557 (2016).

[160] S. Osswald, M. Havel, V. Mochalin, G. Yushin, and Y. Gogotsi, "Increase of nanodiamond crystal size by selective oxidation," Diam. Relat. Mater. **17** 1122–1126 (2008).

[161] V.G. Ralchenko, V.S. Sedov, A.A. Khomich, V.S. Krivobok, S.N. Nikolaev, S.S. Savin, I.I. Vlasov, and V.I. Konov, "Observation of the Ge-vacancy color center in microcrystalline diamond films," Bull. Lebedev Phys. Inst. **42**, 165–168 (2015).

[162] K.V. Bogdanov, V.Y. Osipov, M.V. Zhukovskaya, C. Jentgens, F. Treussart, T. Hayashi, K. Takai, A.V. Fedorov, and A.V. Baranov, "Size-dependent Raman and SiV-center luminescence in polycrystalline nanodiamonds produced by shock wave synthesis," RSC Adv. **6**, 51783–51790 (2016).

[163] M.J. Crane, A. Petrone, R.A. Beck, M.B. Lim, X. Zhou, X. Li, R. M. Stroud, and P.J. Pauzauskie, "High-pressure, high-temperature molecular doping of nanodiamond," Sci. Adv. **5**, eaau6073 (2019).

[164] P.-H. Chung, E. Perevedentseva, and C.-L. Cheng, "The particle size-dependent photoluminescence of nanodiamonds," Sur. Sci. **601**, 3866–3870 (2007).

[165] V.A. Shershulin, V.S. Sedov, A. Ermakova, U. Jantzen, L. Rogers, A.A. Huhlina, E.G. Teverovskaya, V.G. Ralchenko, F. Jelezko, and I.I. Vlasov, "Size-dependent luminescence of color centers in composite nanodiamonds," Phys. Status Solidi A **212**, 2600–2605 (2015).

[166] A. Yasan, R. McClintock, K. Mayes, D.H. Kim, P. Kung, and M. Razeghia, “Photoluminescence study of AlGaN-based 280 nm ultraviolet light-emitting diodes,” Appl. Phys. Lett. **83**, 4083–4085 (2003).

[167] J. Krustok, H. Collan, and K. Hjelt, “Does the low-temperature Arrhenius plot of the photoluminescence intensity in CdTe point towards an erroneous activation energy?,” J. App. Phys. **81**, 1442–1445 (1997).

[168] S. Kumar, V.A. Davydov, V.N. Agafonov, and S.I. Bozhevolnyl, “Excitation of nanowire surface plasmons by silicon vacancy centers in nanodiamonds,” Opt. Mater. Express **7**, 2586–2596 (2017).

[169] B.R. Smith, D.W. Inglis, B. Sandnes, J.R. Rabeau, A.V. Zvyagin, D. Gruber, C.J. Noble, R. Vogel, E. Ōsawa, and T. Plakhotnik, “Five-nanometer diamond with luminescent nitrogen-vacancy defect centers,” Small **5**, 1649–1653 (2009).

[170] P. Reineck, M. Capelli, D.W. M. Lau, J. Jeske, M.R. Field, T. Ohshim, A.D. Greentree, and B.C. Gibson, “Bright and photostable nitrogen-vacancy fluorescence from unprocessed detonation nanodiamond,” Nanoscale **9**, 497–502 (2017).

[171] E. Neu, D. Steinmetz, J. Riedrich-Möller, S. Gsell, M. Fischer, M. Schreck, and C. Becher, “Single photon emission from silicon-vacancy colour centres in chemical vapour deposition nano-diamonds on iridium,” New J. Phys. **13**, 025012 (2011).

[172] S. Lindner, A. Bommer, A. Muzha, A. Krueger, L. Gines, S. Mandal, O. Williams, E. Londero, A. Gali, and C. Becher, “Strongly inhomogeneous distribution of spectral properties of silicon-vacancy color centers in nanodiamonds,” New J. Phys. **20**, 115002 (2018).

[173] L. Himics, S. Tóth, M. Veres, and M. Koós, “Spectral properties of the zero-phonon line from ensemble of silicon-vacancy center in nanodiamond,” Opt. Quant. Electron. **48**, 394 (2016).

[174] S.A. Grudinkin, N.A. Feoktistov, K.V. Bogdanov, A.V. Baranov, and V.G. Golubev, “Photoluminescence of germanium-vacancy color centers in diamond particles obtained by chemical vapor deposition,” Phys. Solid. Stat. **62**, 919–925 (2020).

[175] V.S. Krivobok, E.A. Ekimov, S.G. Lyapin, S.N. Nikolaev, Y.A. Skakov, A.A. Razgulov, and M.V. Kondrin, “Observation of a 1.979-eV spectral line of a germanium-related color center in microdiamonds and nanodiamonds,” Phys. Rev. B **101**, 144103 (2020).

[176] Y. Toyozawa, “Optical processes in solids,” Cambridge University Press, New York (2003) pp. 64–68.

[177] T. Iida and H. Ishihara, “Theoretical study of the optical manipulation of semiconductor nanoparticles under an excitonic resonance condition,” Phys. Rev. Lett. **90**, 057403 (2003).

[178] H. Ishihara, “Optical manipulation of nanoscale materials by linear and nonlinear resonant optical responses,” Adv. Phys.: X **6**, 1885991 (2021).

[179] H. Fujiwara, K. Yamauchi, T. Wada, H. Ishihara, and K. Sasaki, “Optical selection and sorting of nanoparticles according to quantum mechanical properties,” Sci. Adv. **7**, eabd9551 (2021).

[180] C. Pin, R. Otsuka, and K. Sasaki, “Optical Transport and Sorting of Fluorescent Nanodiamonds inside a Tapered Glass Capillary: Optical Sorting of Nanomaterials at the Femtonewton Scale,” ACS Appl. Nano Mater. **3**, 4127–4134 (2020).

List of publications

1 **Y. Makino**, T. Mahiko, M. Liu, A. Tsurui, T. Yoshikawa, S. Nagamachi, S. Tanaka, K. Hokamoto, M. Ashida, M. Fujiwara, N. Mizuochi, and M. Nishikawa, "Straightforward synthesis of silicon vacancy (SiV) center-containing single-digit nanometer nanodiamonds via detonation process," Diamond and Related Materials **112**, 108248 (2021).

2 **Y. Makino**, Y. Saito, H. Takehara, A. Tsurui, N. Okuyama, and M. Ashida, "Effect of particle size on the optical properties of silicon-vacancy centers in nanodiamonds fabricated by a detonation process," Physica Status Solidi A **219**, 2200342 (2022).

3 **Y. Makino**, T. Yoshikawa, A. Tsurui, M. Liu, G. Yamagishi, M. Nishikawa, T. Mahiko, M. Ohno, M. Ashida, and N. Okuyama, "Direct synthesis of group IV-vacancy center-containing nanodiamonds via detonation process using aromatic compound as group IV element source," Diamond and Related Materials **130**, 109493 (2022).

4 **Y. Makino**, Y. Saito, N. Okuyama, A. Tsurui, Y. Kishino, T. Kouuchi, Y. Takeuchi, and M. Ashida, "Optical properties of negatively charged germanium-vacancy centers in detonation nanodiamonds with an average particle size of 10 nm" in preparation.

List of presentations

1 **Y. Makino**, T. Mahiko, M. Liu, A. Tsurui, T. Yoshikawa, S. Nagamachi, S. Tanaka, K. Hokamoto, M. Ashida, M. Fujiwara, N. Mizuochi, and M. Nishikawa, "Creation of silicon vacancy (SiV) center-containing nanodiamonds by detonation process," 34th Diamond Symposium, Online, 2021.

2 **Y. Makino**, S. Tanaka, T. Mahiko, T. Kouuchi, K. Kusakabe, K. Hokamoto, and M. Ashida, "On the mechanism of nanodiamond formation during detonation synthesis using time-resolved optical emission spectroscopy," 14th International Conference on New Diamond and Nano Carbons 2020/2021 (NDNC 2020/2021), Online, 2021.

3 **Y. Makino**, Y. Saito, and M. Ashida, "Optical properties of color centers in nanodiamonds fabricated by detonation process," The 10th Optical Manipulation and Structured Materials Conference (OMC), Yokohama, Japan, 2023.

4 **Y. Makino**, "Mass production of fluorescent nanodiamonds by a detonation process and their application developments," The 51st Thin Film and Surface Seminar (Invited Speaker), Kanazawa, Japan, 2023.

5 **Y. Makino**, T. Yoshikawa, A. Tsurui, M. Liu, M. Nishikawa, T. Mahiko, M. Ohno, M. Ashida, and N. Okuyama, "Direct synthesis of nanodiamonds containing silicon- or germanium-vacancy centers via detonation techniques," 33rd International Conference on Diamond and Carbon Materials (ICDCM), Mallorca, Spain, 2023.

6 **Y. Makino**, Y. Saito, T. Horai, Y. Minowa, H. Ishihara, and M. Ashida, “Optical manipulation of fluorescent nanodiamonds produced by a detonation process,” 84th The Japan Society of Applied Physics (JSPS) Autumn Meeting, Kumamoto, Japan, 2023.

List of awards

1 **Y. Makino**, 34th Diamond Symposium 2021, Oral Session Best Award.

2 **Y. Makino**, T. Mahiko, M. Liu, A. Tsurui, and T. Yoshikawa, 75th Kinka Chemical Society (KCS) Award in Chemical and Environmental Technology 2022.

Acknowledgments

First of all, I would like to express my warmest gratitude to my supervisor, Professor Masaaki Ashida, for accepting me as his student and for his constant, kind, and patient guidance throughout this study. I would not have been able to complete my doctoral dissertation while working at my company without his great efforts. I also would like to acknowledge the helpful suggestions by Associate Professor Masaya Nagai and Assistant Professor Yusuke Minowa. I cannot thank them enough for teaching me physics as a researcher at a chemical company.

I would like to grateful my appreciation to Professor Hajime Ishihara and Professor Katsuya Shimizu for their willingness and valuable time to be a member of my doctoral defense reviewer committee. I also would like to thank them for the beneficial advice and careful reviews, which significantly improved this dissertation.

This research has been accomplished through the great contributions of many collaborators. I sincerely thank Professor Kazuyuki Hokamoto, Associate Professor Shigeru Tanaka, and Mr. Takeshi Kusano of Kumamoto University for their technical cooperation in explosive engineering. Their expertise helped me make the time-resolved spectroscopic measurements and the high-speed camera observation during the detonation reaction successful. I also thank Dr. Takehiro Matsunaga of the National Institute of Advanced Industrial Science and Technology for safety assessments in explosive handling.

My special thanks go to Daicel-Engineering Science Collaborative Laboratory members for their support. Notably, I owe a great deal to Mr. Satoshi Sakamoto for his profound comments and helps me not only in this work but also in my life of doctoral course. Moreover, I would like to express my sincere gratitude to Professor Naoto Okuyama who guided all computational studies in this dissertation. He also encouraged me to pursue my research interest through valuable discussion.

I thank all members and secretaries of the Center for Industry-University Collaboration. Particularly, I am deeply grateful to Professor Shigeo Wada for believing in me and giving me the opportunity to enroll doctoral course while working for my company. My heartful thanks are due to Mr. Shinzo Uda for his personal support.

I gratefully acknowledge this study of past and present members of the Ashida laboratory, especially Mr. Yoshiki Saito who tried hard with me to characterize the optical properties of the SiV^- and GeV^- centers in DNDs.

This work would not be produced without the support and encouragement of my company, Daicel Corporation. I am indebted to my coworkers for their contributions. The following people supported this research: Mr. Akihisa Takabe, Dr. Mitsuteru Mutsuda, Mr. Motohiro Kawasaki, Mr. Ichiro Takase, Mr. Kouichi Umemoto, Dr. Takahiro Tei, and Mr. Tomohiro Goto. Especially, I want to extend my thanks to members of the nanodiamond team: Dr. Tomoaki Mahiko has monitored my progress and encouraged me throughout; Mr. Masahiro Nishikawa and Dr. Liu Ming provided me with many discussions and suggestions for improving my English writing; Dr. Taro Yoshikawa has been supportive and has provided me with invaluable teaching opportunities, as a specialist in diamond science; Mr. Akihiko Tsurui, Mr. Yoshiki Kishino, Mr. Takashi Kouuchi, and Mr. Yusaku Takeuchi assisted with the detonation experiments, nanodiamonds purifications, and characterizations, all experiments could not have been carried out safely without their efforts. My gratitude is also extended to Analysis Service Center staff: Mr. Gaku Yamagishi for the TEM observations; Dr. Naoki Takao and Dr. Mariko Ogura for the powder XRD analyses and XRF measurements. Significantly, my heartfelt thanks go to Dr. Mitsuru Ohno who not only guided the discussion of thermodynamics and kinetics in the detonation reaction in this dissertation but also expanded my perspective through the discussion, as a specialist in synthetic organic chemistry. Most of all, I would like to give special thanks to my boss, Mr. Hisayoshi Ito, who made me recognize the importance of physics and gave me the opportunity to study it.

My acknowledgments would not be complete without thanking my family. I am deeply indebted to My wife, Ms. Mai, for her continuous support and encouragement.

Yuto Makino
Division of Frontier Materials Science
Graduate School of Engineering Science
Osaka University, Toyonaka, Osaka 560-8531, Japan